

Coulomb induced interplay of localized and reservoir carriers in semiconductor quantum dots

Vorgelegt von Diplom-Physiker
Alexander Wilms
aus Berlin

von der Fakultät II – Mathematik und Naturwissenschaften
der Technischen Universität Berlin

zur Erlangung des akademischen Grades
Doktor der Naturwissenschaften

— **Dr. rer. nat.** —

genehmigte Dissertation

Promotionsausschuss

Vorsitzende : Prof. Dr. rer. nat. Ulrike Woggon, TU Berlin
1. Gutachter : Prof. Dr. rer. nat. Andreas Knorr, TU Berlin
2. Gutachter : Priv.-Doz. Dr. rer. nat. Uwe Bandelow, WIAS

Tag der wissenschaftlichen Aussprache: 12.12.2012

Berlin 2013

D 83

Abstract

This thesis is about the calculation of Coulomb–scattering processes between bound states in semiconductor quantum dots and delocalized states of the surrounding reservoir. The thesis is divided into two parts. The central topic is the fundamental question, how reservoir dimensionality influences Coulomb scattering. It was discussed, that 2D scattering is more efficient than 3D scattering, due to the lower dimensionality. The results on that topic, presented in the first part, might improve the understanding of fundamental experiments like pump-probe measurements. In the second part, the influence of Coulomb scattering processes on material gain and refractive index in quantum dot devices will be investigated. This is of fundamental importance for quantum dot device simulation.

The Coulomb scattering processes are treated in this thesis within the framework of a microscopic model in the limit of Born-Markov approximation. Screening effects were included in the limit of the Lindhard formula and perturbation of the reservoir wavefunctions caused by the quantum dot states are incorporated via orthogonalized plane waves. In addition, it was shown how to extend the theory for the description of weakly, spatially inhomogeneous carrier densities.

In the central part of this thesis - the investigation of the impact of the reservoir dimensionality - Coulomb scattering rates for two systems are compared. Equal quantum dots coupled to different reservoirs are assumed. The quantum dots in model system (i) are coupled to a two dimensional reservoir, for example a quantum well, whereas in model system (ii), the quantum dots are coupled to the three dimensional reservoir formed by the bulk material. The higher dimensional integrals (up to 8D), appearing in the calculation of the scattering rates, particularly in model system (ii), are evaluated efficiently via Quasi-Monte Carlo method. In the calculations presented here, the significant rates showed similar behavior concerning the carrier density dependency, although the rates differ in details. As an example, the two model systems show an opposite behavior concerning the quantum dot height. Contrary to the assumption of more efficient 2D scattering, the 2D rates have not shown to be more efficient in general. This is in agreement with experimental observations.

In the second part of the presented results, the polarization dynamics are investigated to calculate gain spectra. The quantum dots under consideration, contain two energy levels and couple to a two dimensional carrier reservoir. The impact of Coulomb scattering on microscopic polarization is investigated in terms of a microscopically determined dephasing time T_2 . From this one can calculate the homogeneous linewidth of the quantum dot transition, which in turn can be used to calculate the gain spectra and the refractive index of the quantum dot material. The results are compared with results of the benchmark model of M. Lorke et. al. and with experimental results. It is found that the basic features like gain reduction of quantum dots and the qualitative behavior of the homogeneous broadening are nicely reproduced by the model presented here. Therefore, it improves the understanding of device limiting processes and offers a good compromise between accuracy and effort for usage in device simulation.

Zusammenfassung

Diese Arbeit befasst sich mit der Berechnung von Coulomb-Streuprozessen zwischen gebundenen Zuständen in Halbleiter Quantenpunkten und den delokalisierten Zuständen des sie umgebenden Reservoirs. Dabei gliedern sich die Ergebnisse in zwei Teile. Das Hauptaugenmerk liegt auf der grundlegenden Frage, wie die Reservoirdimensionalität diese Streuprozesse beeinflusst. Es wurde diskutiert, ob aufgrund der reduzierten Dimensionalität die Streuung aus 2D effizienter ist als aus 3D. Die im ersten Teil darüber gewonnenen Ergebnisse können dazu beitragen grundlegende Experimente wie Pump-Probe Messungen besser zu verstehen. Im zweiten Teil wird der Einfluss der Coulomb-Streuung auf die Lichtverstärkung in Quantenpunkt Bauelementen untersucht. Dieser ist von elementarer Bedeutung für die Simulation solcher Bauelemente.

Die Beschreibung der Coulomb-Streuprozesse erfolgt in dieser Arbeit durch mikroskopische Modelle im Rahmen der Born-Markov Näherung. Es werden sowohl Abschirmungseffekte im Rahmen der Lindhard Formel berücksichtigt, als auch Störungen der Reservoirwellenfunktion durch die Quantenpunkte mittels orthogonalisierter ebener Wellen. Ferner wird gezeigt, wie man zu einer ortsabhängigen Systembeschreibung übergehen kann, um schwache räumliche Dichteinhomogenitäten zu behandeln.

Im Hauptteil - der Untersuchung des Einflusses der Reservoirdimensionalität - werden Coulomb-Streuratzen zweier Modellsysteme miteinander verglichen. Es wird angenommen, dass die Quantenpunkte beider Modellsysteme gleich sind, jedoch unterscheiden sich die Ladungsträgerreservoirs. In Modellsystem (i) sind die Quantenpunkte an ein zweidimensionales Reservoir gekoppelt, beispielsweise eine Quanten-Barriere, wohingegen die Quantenpunkte in Modellsystem (ii) direkt an das dreidimensionale Reservoir koppeln, welches das Volumenmaterial bildet. Die bei der Berechnung der Streuratzen, insbesondere im System (ii), auftretenden höherdimensionalen Integrale (bis zu 8D), werden mit Hilfe des Quasi-Monte Carlo Verfahrens effizient berechnet. In den hier präsentierten Rechnungen zeigen die signifikanten Streuratzen beider Modellsysteme ein ähnliches qualitatives und quantitatives Verhalten bezüglich der Ladungsträgerdichte, jedoch weisen die Raten im Detail Unterschiede auf. So ist beispielsweise die Abhängigkeit der Streuratzen von der Quantenpunkthöhe gegensätzlich. Entgegen der Annahme zeigt sich jedoch, dass die 2D Raten nicht grundsätzlich effizienter sind. Dies ist im Einklang mit experimentellen Beobachtungen.

Im zweiten Ergebnisteil wird zur Berechnung des Gewinnspektrums von Quantenpunkten deren Polarisationsdynamik untersucht. Es werden Quantenpunkte mit zwei Energieniveaus betrachtet, die an ein umliegendes 2D Reservoir koppeln. Durch Berechnung der Dephasierungszeit T_2 wird für dieses System der Einfluss der Coulomb-Streuung auf die mikroskopische Polarisation untersucht. Die daraus gewonnene homogene Linienbreite des Quantenpunktübergangs wird genutzt, um Spektren und den Brechungsindex des Quantenpunktmaterials selbstkonsistent zu berechnen. Die Ergebnisse werden mit Resultaten aus Benchmark-Rechnungen von M. Lorke et al., sowie experimentellen Ergebnissen verglichen. Dabei zeigt sich, dass grundlegende Effekte, wie beispielsweise Gewinnreduktion oder das qualitative Verhalten der homogenen Linienbreite, durch das erstellte Modell gut beschrieben werden. Somit hilft das Modell die limitierenden Prozesse in Quantenpunktbauteilen besser zu verstehen und bietet einen guten Kompromiss zwischen Aufwand und Exaktheit für eine Nutzung in der Bauteilsimulation.

Contents

List of Figures	ix
1. Introduction	1
2. Setting of the model systems and the theoretical framework	3
2.1. Quantum Dots	3
2.1.1. System used for the gain model	4
2.1.2. Model comparing 2D and 3D scattering rates	5
2.1.3. Setting in a device	5
2.2. Theoretical frame work	7
2.3. Hamiltonian	8
2.4. Wave functions	9
2.4.1. Quantum dot wavefunctions	9
2.4.2. Reservoir wavefunctions- Orthogonalized Plane Waves	10
2.5. Coulomb matrix	13
2.5.1. Screening	14
3. Equations of motion	17
3.1. Quantities of interest	17
3.2. Hierarchy problem and Cluster Expansion	18
3.2.1. A short description of the cluster expansion	18
3.3. Equations of motion describing carrier-carrier scattering	21
3.3.1. Equations in a spatially homogeneous system	21
3.3.2. Equations in a system with an inhomogeneous carrier density	24
3.4. Numerical Integration	28
3.4.1. Grid based methods	29
3.4.2. Monte Carlo estimates	31
3.4.3. Summary	33
4. Comparison of 2D and 3D scattering	35
4.1. Relevant scattering processes	35
4.2. How to compare 2D and 3D carrier densities?	38
4.3. Numerical results	40
4.3.1. Scattering rates without transitions between QD and reservoir	40
4.3.2. Processes with one transition between QD and reservoir	41
4.3.3. Scattering rates with two transitions between QD and reservoir	43
4.3.4. Comparison of the relaxation processes	43
4.3.5. Do large deviations between 2D and 3D scattering rates appear?	46
4.3.6. Summary of intermediary results	47

4.3.7. Comparison with experiments	47
4.3.8. Parameter studies	52
4.3.9. Direction dependency of the scattering	57
4.3.10. The role of OPW approaches	58
4.4. Conclusions	60
4.5. Outlook	61
5. A microscopic gain model	63
5.1. Dephasing time and homogeneous broadening	63
5.1.1. Comparison of the theoretical model with experiment	64
5.1.2. Comparison with a theoretical benchmark model	65
5.2. Refractive Index	67
5.3. Quantum dot material gain	67
5.4. Discussion	69
A. Details of the orthogonalized plane waves	71
A.1. Orthogonalized plane waves for the bulk states standardly used	71
A.2. Additional possible orthogonalized plane waves.	74
B. Coulomb integrals	77
C. Derivation Screening	79
C.1. Screening in 3D	82
C.2. Screening in 2D	83
D. Derivation of the T_2 time	85
E. Light matter interaction	97
E.1. Calculation of macroscopic polarization	98
E.2. Material gain	100
E.3. Refractive index	101
F. List of parameters	103
G. Bibliography	107

List of Figures

2.1.	STM pictures of InAs QDs [1]	3
2.2.	Illustration of the density of states for different structures taken from Ref. [2]	4
2.3.	Illustration of the considered systems for the gain model.	4
2.4.	Illustration of the systems used for comparison of 2D and 3D rates	5
2.5.	Illustration of the material composition of a VCSEL (from T. Koprucki)	6
2.6.	Calculated electron density in the laser structure (from T. Koprucki)	6
2.7.	Screening wavenumber κ	16
3.1.	Illustration of a numerical integration via a Riemann sum	30
3.2.	Comaprison of random points with Sobol points	32
4.1.	Illustration of the main scattering processes	36
4.2.	Illustration of the height L of the mesoscopic structures.	38
4.3.	Fermi distributions for electrons and holes	39
4.4.	Carrier relaxation rate $S_{GS,rel,1}^{in}$	41
4.5.	Capture rates: $S_{D,cap}^{in}$	42
4.6.	Carrier relaxation rate $S_{GS,3QD}^{in}$	42
4.7.	Carrier relaxation rate $S_{D,rel,2}^{in}$	43
4.8.	Carrier relaxation rates, pure CB electron contribution	44
4.9.	Exchange terms $S_{GS,exch.}^{in}$ of the relaxation processes.	45
4.10.	Mixed electron-hole processes of $S_{GS,Rel2}^{in}$	46
4.11.	Scheme of the processes involved in the PL-rise time, according to Ref. [3]	48
4.12.	Calculated rise time τ_{fill}	49
4.13.	Photoluminescence rise time (experiment) from Ref. [4]	50
4.14.	Capture rate for different heights of the mesoscopic structures	53
4.15.	Capture rate for a different set of material parameters	54
4.16.	Capture rate for holes	55
4.17.	Capture in dependence of the chemical potential	56
4.18.	Excited state capture rates for shifted and unshifted Fermi-distributions.	57
4.19.	Illustration of the direction dependency of a capture rate	58
4.20.	Excited states capture rate for different OPW approaches.	59
4.21.	Illustration of differences between the different OPW-types	60
5.1.	Dephasing time T_2 and twice the carrier lifetime T_1	64
5.2.	Comparison of the homogeneous broadening: with experiment	65
5.3.	Comparison of the homogeneous broadening: with benchmark model	66

LIST OF FIGURES

5.4. Refractive index n_r 67
5.5. Maximal gain and gain spectra 68
5.6. Illustration of the impact of T_2 on the maximal gain 69

1. Introduction

In the last decades, electronic data exchange has become crucially important: By the end of 2011, more than two billion people had Internet access [5]. Internet applications have become an integral part of the every-day life of hundreds of million people. According to Cisco systems [6], the “compound annual growth rate” of the worldwide IP traffic will be 34 % between 2009 and 2014, exceeding about 767 exabytes ($= 767 \times 2^{60}$ bytes $\approx 767 \times 10^{18}$ bytes) in 2014. As a result of that, there is a need to develop advanced devices for high-speed data transmission.

Semiconductor nanomaterials play an important role in new device types. Especially quantum dot (QD) materials [7] are promising candidates for future devices, as they have shown impressive results for various device types.

Due to the elaborate production process of these nanostructures, it is necessary to have reliable simulators to predict device properties. One integral component of a device simulator is a description of how the material behaves realistic conditions. For example scattering rates, which describe the filling and discharging of system states, have a strong influence on the laser dynamics and the possible data transmission rate of amplifiers. The material gain, which describes the absorption or amplification of light by the active media, is also a key parameter for optical devices. In turn, a microscopic material description is a key to understanding device limiting processes. For that reason, this thesis will focus on a microscopic description of Coulomb scattering. In the high-density regime under consideration, Coulomb scattering is one of the dominant interaction mechanisms in QD devices [8].

During the last few decades, there has been an enormous progress in the theoretical modeling of semiconductor devices: Haken, Haug, and others established the basis for a microscopic description of solid-state lasers between the 1960s and the 1990s [9, 10]. In the 1980s and 1990s, there was a lot of successful work in the description of quantum well (QW) lasers (e.g. by Bastard, Chow, Hader, Haug, Koch and co-workers [11, 12, 13, 14, 15, 16]). The variety of effects in QD materials has also been intensively studied.

There has been extensive publication on the theoretical description of Coulomb scattering in QD devices (see e.g. [17, 18, 19, 20, 21, 22]). The focus has been mainly on a system consisting of QDs and a *two-dimensional carrier reservoir* (2DCR), e.g. a QD-wetting layer (WL)¹ or a dot in a well (DWELL) system, due to its importance for optical devices and the established production processes for the related devices [7]. Special note should be taken of the work of Nielsen et al. [20], presenting a detailed study of various scattering processes in typical QD systems. Most of these works examine processes within the Markovian limit. Schneider et al., as well as Lorke et al. improved these models by including non-Markovian effects [24, 25]. This was shown to

¹ For thin WL structures it is not guaranteed that a WL contains bound states. This is a result of growth variations [23]. However, in this thesis it is assumed that a WL is a 2D reservoir.

1. Introduction

be important to dissolve artifacts, such as the phonon bottleneck, to include pure inner dot scattering processes, and to describe the fast polarization dynamics in QD devices.

Only few articles examine systems consisting of QDs directly coupled to the bulk material, acting as a *three-dimensional carrier reservoir* (3DCR), e.g. [26, 27, 28, 29]. This might be due to the current lesser technical importance of these devices compared to typical Stranski-Krastanow QD-2D reservoir systems. However, the much higher numerical complexity that is necessary for the treatment of a 3D system might also be a reason it is rarely investigated. Nevertheless, there are applications where advantages can be expected from a QD-3D system in comparison to QD-2D systems. For example, the absence of the 2D carrier reservoir promises a faster response in amplifiers. There are encouraging candidates for efficient production of these structures using modern growth techniques like modified droplet epitaxy or sub-monolayer (SML) deposition, as well as QD etching or colloidal QDs, so that these structures may become of higher technical importance in future.

The question arises whether these kinds of structures contain some inherent disadvantages compared to the 2D system: Sanguinetti et al. [30] reference a long debate on the necessity of a 2D reservoir for efficient feeding of the QD with reservoir carriers. Sanguinetti et al. investigated this question experimentally, cf. also [4]. The central question of this thesis strives to answer from the theoretical point of view is:

What is the influence of the reservoir dimensionality on the Coulomb scattering processes between QD and reservoir?

This question will be answered within the framework of a microscopically derived Boltzmann equation by comparing the Coulomb scattering rates of a QD-2D system with a QD-3D system. To overcome difficulties in the numerical evaluation of the QD-3D system, namely high dimensional integrals, a quasi-Monte Carlo (QMC) method is used, cf. [31, 32]. Furthermore, some calculations of spatial resolution of the scattering rates will be done to accommodate the settings to a laser device. A further aspect treated in this thesis is the description of the QD material gain via a compact model.

This work is structured as follows:

Chapter 2 introduces the model system and the model assumptions for the following calculations. The analytical results are presented in Chap. 3. That chapter also introduces the most significant analytical and numerical techniques used in this thesis. In Chap. 4, the influence of the reservoir dimensionality on the scattering rates is investigated. The gain model will be discussed in Chap. 5.

2. Setting of the model systems and the theoretical framework

In this chapter, the first section (Sec. 2.1) introduces the model systems used: Sec. 2.1.1 for the gain model and Sec. 2.1.2 for the investigation of the reservoir dependency of the Coulomb scattering rates. Furthermore, Sec. 2.1.3 provides a short description of the conditions in a laser.

The subsequent Section (Sec. 2.2) introduces the framework of the theoretical description. In Sec. 2.3, the Hamiltonian will be introduced. Connected with that, Sec. 2.4 discusses the associated eigenfunctions, in particular the construction of orthogonal plane waves (OPWs), cf. Sec. 2.4.2. Finally, Sec. 2.5 discusses the Coulomb matrix.

2.1. Quantum Dots

Quantum dots are 3D-structures with an extension of between several tens and several hundred ångström in each direction [7].

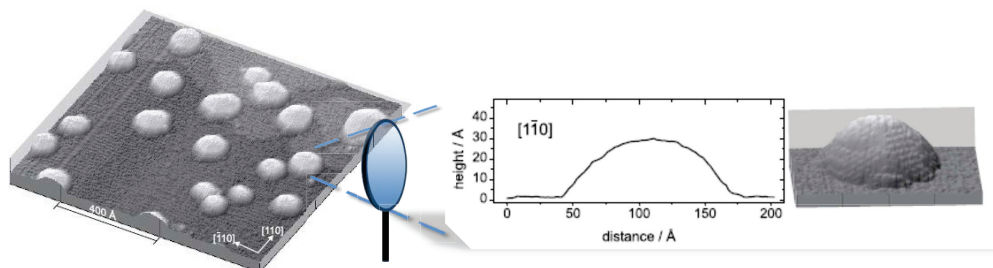


Figure 2.1.: Scanning tunneling microscope (STM) pictures of InAs QDs. The pictures are taken from Ref. [1]

A crucial distinction from other quantum confined structures is an extension of the carrier wavefunction below its de Broglie wavelength and the resulting δ -distribution like density of states (DOS), cf. Fig. 2.2.

Due to this strong spatial confinement, the movement of the carriers in QDs is restricted in all three dimensions. That is why they are also designated *0D structures* or respective as *artificial atoms*. The latter designation also refers to the discrete energy levels of QDs. A detailed description of QDs can be found in Ref. [7] among others.

In this thesis, GaAs/In(Ga)As material systems are examined due to their vital importance to telecom devices. In principle the (mathematical) material description used in this thesis is also valid for other material systems. However, other material systems

2. Setting of the model systems and the theoretical framework

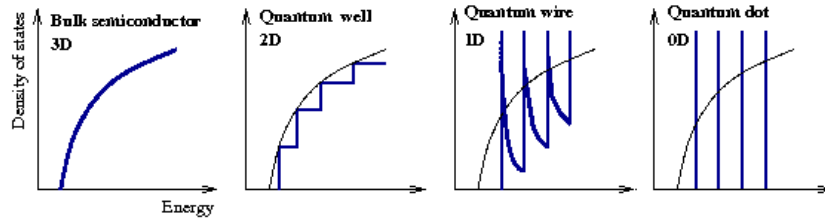


Figure 2.2.: Illustration of the density of states for different quantum confined structures in comparison to bulk material. The picture is taken from [2].

might include additional effects of great importance, such as internal electric fields in nitride structures. Such effects are not taken into consideration here.

Typical QD laser devices in the GaAs/In(Ga)As material systems, obey self-organized grown QDs with area densities of several 10^{10} cm^{-2} and size fluctuations of about 10 %, cf. Fig. 2.1. The size fluctuations of the QDs lead to a Gaussian-shaped, inhomogeneous broadening of the spectra, with a full width at half maximum (FWHM) of about 60 meV [33]. This line broadening is significant to the gain model presented in Sec. 5.3.

2.1.1. System used for the gain model

For the gain model a single layer with so called *shallow QDs* is considered. These shallow QDs exhibit two confined (spin degenerate) energy states –one related to the conduction band (CB), and one related to the valence band (VB). See Fig 2.3.

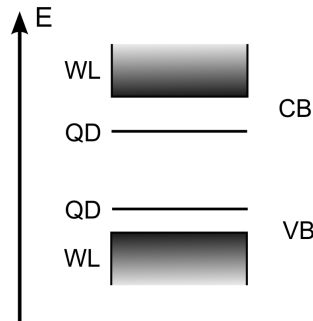


Figure 2.3.: Illustration of the considered systems for the gain model.

The QDs are embedded in a 2D carrier reservoir. There will be no distinction between WL and QW structures. Furthermore, equal effective masses in the QD and 2D material will be assumed.

Assuming shallow QDs is a model simplification. Most QDs used for devices exhibit at least one further (degenerate) excited state. This simplification is assumed (i) in order to achieve a basic model for easier understanding of the underlying physics of the dephasing induced by Coulomb scattering. (ii) In a multi-level QD scattering processes

appear that cannot be treated within the framework of the approximations used in this thesis, cf. [24].

2.1.2. Model comparing 2D and 3D scattering rates

In Chap. 4 two different QD samples are investigated. (i) First is a QD from an ensemble of equal QDs with an s-like ground state (GS) and two degenerate p-like excited states (ES) for each band. The QD is coupled to a 2D carrier reservoir with a 2D parabolic dispersion relation. (ii) Second, the same QD (ensemble), but coupled to a 3D carrier reservoir with a parabolic 3D dispersion relation, cf. Fig. 2.4.

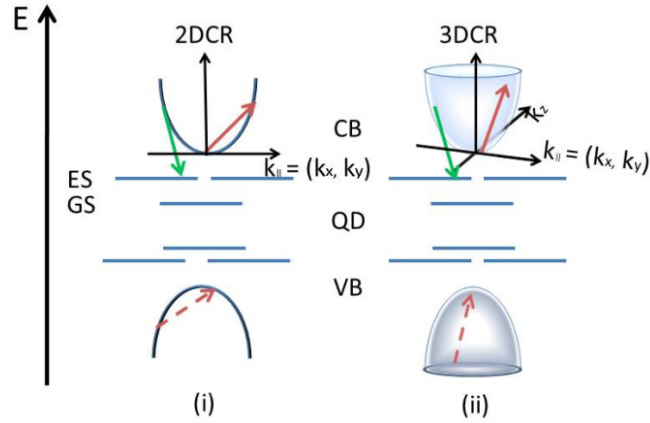


Figure 2.4.: Illustration of systems used for comparison. Sample (i): QD coupled to a 2D carrier reservoir (e.g. a dot in a well system). Sample (ii): QD coupled to a 3D carrier reservoir (e.g. a Vollmer-Weber QD bulk system). The capture process into a QD excited state is depicted for both systems (cf. Eq. (4.4)).

To ensure a fair comparison of the two samples, QDs with equal wavefunctions (and thus the same QD-material parameters) are assumed. Unless otherwise stated, the same effective masses for the 2D carrier reservoir as for the QD have been used in calculations [20, 34, 21], whereas GaAs effective masses have been used for the 3D carrier reservoir.

2.1.3. Setting in a device

A typical laser device, e.g. a vertical cavity surface emitting laser (VCSEL), has a size range within several micrometers. In contrast, the optically active region has a height on the order of several tens, and up to a few hundred, of nanometers, cf. Fig. 2.5.

The carrier density within such a device is spatially inhomogeneous, as can be seen in Fig. 2.6. Figures 2.6 and 2.5 were made by T. Koprucki. Calculations by T. Koprucki et al. clearly reveal that the carrier density varies (different colors) in in-plane direction, as well as in growth direction.

causing what is referred to as “current crowding” at the borders of the optically active region. However, at a length of about $0.5 \mu\text{m}$, the carrier densities can be assumed as constant.

For simplicity, charge neutrality is assumed to be restricted to the carrier reservoirs:

$$n_{2\text{D}/3\text{D}} = n_{2\text{D}/3\text{D}}^e = n_{2\text{D}/3\text{D}}^h. \quad (2.1)$$

$n_{2\text{D}/3\text{D}}^{e/h}$ denotes the the 2D/ 3D carrier density for electrons/ holes. For more details, cf. Sec. 4.2 and Sec. 5.1.2.

2.2. Theoretical frame work

In this thesis, the description of the system is based on the framework of the second quantization. A detailed introduction to that formalism, can be found in Refs. [36, 37, 38, 39] among others.

In second quantization, the well-known annihilation / creation operators a_i / a_i^\dagger are used to describe the destruction / creation of fermions in the (multi-particle) state “ i ”:

$$a_i^\dagger|0\rangle = |\psi_i\rangle, \quad \langle \vec{r} | \psi_i \rangle = \psi_i(\vec{r}), \quad (2.2)$$

where $|0\rangle$ denotes the vacuum state. The compound index “ i ” defines the set of quantum numbers of the system state $|\psi_i\rangle$. Here for example, i could identify a QD state $i = D$, or either a 2D or 3D reservoir state $i = \mathbf{k}_i$. D includes the quantum numbers for the valence / conduction band Λ_D^1 , quantum numbers describing the type of the state, the spin σ_D and the QD position \vec{R}_D , cf. Ref. [20]. \mathbf{k}_i mainly includes band Λ_{k_i} and spin σ_{k_i} , as well as the carrier wavenumber \vec{k}_i :

$$\mathbf{k}_{i,3D} = (\Lambda_i, \vec{k}_i = (k_x^i, k_y^i, k_z^i), \sigma_i) \quad (2.3)$$

defines the 3D reservoir states and

$$\mathbf{k}_{i,2D} = (\Lambda_i, \vec{k}_i = (k_x^i, k_y^i), \sigma_i, R_z^i) \quad (2.4)$$

defines the 2D ones. The z-position of the 2D reservoir is also a quantum number here, as different QD-layers need to be specified (in Chap. 4). In turn R_z^i can be left if one considers a single QD-layer.

¹In this thesis the calculations in the formalism of second quantization are performed in a pure electron picture (valence band / conduction band). The related band indices are denoted by $\Lambda = c, v$. For the evaluation of the results the electron-hole picture is preferable. Then the band indices will be denoted by $\lambda = e, h$.

2. Setting of the model systems and the theoretical framework

As usual, the fermionic creation / annihilation operators should fulfill the anticommutator relations

$$\left[a_i, a_j^\dagger \right]_+ = a_i a_j^\dagger + a_j^\dagger a_i = \delta_{i,j}. \quad (2.5)$$

$$\left[a_i, a_j \right]_+ = 0, \quad (2.6)$$

$$\left[a_i^\dagger, a_j^\dagger \right]_+ = 0. \quad (2.7)$$

So the set of states associated with the creation / annihilation operators used here should form an orthonormal basis (ONB).

2.3. Hamiltonian

Unless noted otherwise, the following Hamiltonian is considered in this thesis:

$$H = H_{0,el} + H_{\text{int}} + H_C \quad (2.8)$$

$$H_{0,el} = \sum_m \varepsilon_m a_m^\dagger a_m, \quad (2.9)$$

$$H_{\text{int}} = - \sum_{m,n} \vec{E}(t) \cdot \vec{d}_{mn} a_m^\dagger a_n, \quad (2.10)$$

$$H_C = \frac{1}{2} \sum_{abcd} V_{abcd} a_a^\dagger a_b^\dagger a_c a_d. \quad (2.11)$$

$H_{0,el}$ describes the particles in the unperturbed potential of the model system. H_{int} describes the interaction of the carriers with a classical E-field $\vec{E}(t)$, mediated by the dipole matrix elements \vec{d}_{mn} . So the light-matter interaction is assumed in dipole approximation. The Coulomb part H_C describes a two particle interaction: Particles in the states c and d are destroyed, whereas particles in the states a and b are created. V_{abcd} is an unscreened Coulomb matrix element

$$V_{abcd} = - \int d^3 r \int d^3 r' \psi_a^*(\vec{r}) \psi_b^*(\vec{r}') V(|\vec{r} - \vec{r}'|) \psi_d(\vec{r}') \psi_c(\vec{r}), \quad (2.12)$$

and W_{abcd} will denote the related screened ones. Screening will be included in the static limit of the Lindhard formula [39], cf. Sec. 2.5.1

In this thesis, carrier-phonon interaction is omitted. In the high density regime under consideration, carrier-phonon and carrier-carrier interactions are of comparable significance to the device dynamics. Typically, those interactions are treated separately and focusing on one of them is common practice [40, 41]. However, via a non-Markovian treatment of the system, Lorke et al. pointed out that both interactions are coupled by line-broadening effects [24, 42]. Nevertheless, it has been shown that a coupled treatment of Coulomb and carrier-phonon interaction is more important for the carrier-phonon than for the Coulomb interaction [43].

2.4. Wave functions

The Hamiltonian Eq.(2.8)–(2.11) does not contain off-diagonal elements of the form $\sum_{m,n} \varepsilon_{mn} a_m^\dagger a_n$. So the basis associated with the creation / annihilation operators should be an eigenbasis of $H_{0,el}$ [44]. The spectra of nanodevices considered here reveals clear fingerprints of the respective subsystems. As a result, the eigenstates can be allocated² to a certain subsystem and therefore each subsystem forms a complete subspace. The starting point for various wavefunctions is a factorizing envelope ansatz:

$$\psi_l(\vec{r}) = \hat{\psi}_l(\vec{r}) u_{(\Lambda_l, \sigma)}(\vec{r}) = \varphi_l(\vec{r}_{||}) \xi_l(z) u_{(\Lambda_l, \sigma)}(\vec{r}). \quad (2.13)$$

So it is assumed, that the 3D wavefunction $\psi_l(\vec{r})$, with $\vec{r} = (x, y, z)$, can be decomposed into a combined Bloch function at $\vec{k} = 0$ times spin part $u_{(\Lambda_D, \sigma_D)}(\vec{r})$, and an envelope part $\hat{\psi}_l(\vec{r})$. Furthermore, the envelope part itself is also assumed to be decomposable into an in-plane part, $\varphi_i(\vec{r}_{||})$, with $\vec{r}_{||} = (x, y)$ times the envelope part $\xi_l(z)$ in growth direction z .

2.4.1. Quantum dot wavefunctions

The in-plane part of the QD wavefunctions is approximated by the lowest eigenstates of a 2D harmonic oscillator, fitted to the energy spacing of the QD-states, cf. Refs. [45, 46, 19]:

$$\varphi_{\text{GS}}^\Lambda(\vec{\rho}) = \sqrt{\frac{m_\Lambda \omega_{\text{QD}}^\Lambda}{\hbar \pi}} \exp\left(-\frac{m_\Lambda \omega_{\text{QD}}^\Lambda}{2\hbar} \rho^2\right), \quad (2.14)$$

for the ground state and

$$\varphi_{\text{ES}, \pm}^\Lambda(\vec{\rho}) = \frac{m_\Lambda \omega_{\text{QD}}^\Lambda}{\hbar \sqrt{\pi}} \rho \exp\left(-\frac{m_\Lambda \omega_{\text{QD}}^\Lambda}{2\hbar} \rho^2\right) \exp(\pm i\alpha). \quad (2.15)$$

for the excited states. Here, $\omega_{\text{QD}}^\Lambda$ denotes the oscillator strength and m_Λ is the QD in-plane effective mass of the particle, cf. Appx. F. The vector $\vec{\rho} := \vec{r}_{||} - \vec{R}_{||}$, with $|\vec{\rho}| = \rho$ and $\vec{R}_{||} := (R_x, R_y)$, describes the distance to the QD-center in the xy-plane.

The eigenfunction in the z-direction is approximated by the ground state eigenfunction of an infinite square well, with an effective height L :

$$\xi_l(z) = \sqrt{\frac{2}{L}} \cos\left(\frac{\pi}{L} z\right) \chi_{[R_z^l - L/2, R_z^l + L/2]}(z). \quad (2.16)$$

$\chi_{[a,b]}(z)$ denotes the indicator function in the interval $[a, b]$:

$$\chi_{[a,b]}(z) = \begin{cases} 1 & \text{for } z \in [a, b], \\ 0 & \text{else.} \end{cases}$$

²Nevertheless, the related wavefunctions could be mixtures of the unperturbed QD and reservoir wavefunctions.

2. Setting of the model systems and the theoretical framework

There are methods to calculate the effective height for a given structure, cf. [47]. Hence it is not a fit parameter. However, since the correct confinement potential is unknown here, the effective height has been arbitrarily chosen so that that electrons in the conduction and valence bands have the same z -wavefunction Eq. (2.16).

2.4.2. Reservoir wavefunctions- Orthogonalized Plane Waves

Typically, an ideal device structure is assumed, disregarding any spatial inhomogeneities such as local fields, growth impurities or density variations [20, 21]. A common choice for the basis then becomes Bloch wavefunctions, in which the envelope wavefunctions are plane waves (PW). So for the 3D carrier reservoir, one chooses the ansatz

$$\begin{aligned}\psi_{\mathbf{k},3DCR}^0(\vec{r}) &= \varphi_{\vec{k}_{||}}^0(\vec{r}_{||})\phi_{k_z}^0(z)u_{(\Lambda_k,\sigma_k)}(\vec{r}), \quad \text{with} \\ \varphi_{\vec{k}_{||}}^0(\vec{r}_{||}) &= \frac{1}{\sqrt{A}} e^{i\vec{k}_{||}\cdot\vec{r}_{||}} \quad \text{and} \quad \phi_{k_z}^0(z) = \frac{1}{\sqrt{L_z}} e^{ik_z\cdot z}.\end{aligned}\quad (2.17)$$

For the envelope of the 2D carrier reservoir, one distinguishes between a strong confined z -direction and the in-plane direction. The in-plane component of the envelope functions $\varphi_{\mathbf{k},2D}(\vec{r}_{||})$ are approximated by PWs, corresponding to the Bloch wavefunctions Eq. (2.17). In the z -direction the same wavefunction Eq. (2.16) as for the QD states will be assumed. In particular, the same effective height is assumed. This leads to the ansatz

$$\begin{aligned}\psi_{\mathbf{k},2DCR}^0(\vec{r}) &= \varphi_{\vec{k}_{||}}^0(\vec{r}_{||})\xi_{\mathbf{k}}(z)u_{(\Lambda_k,\sigma_k)}(\vec{r}) \\ &= \frac{1}{\sqrt{A}} e^{i\vec{k}_{||}\cdot\vec{r}_{||}} \sqrt{\frac{2}{L}} \cos\left(\frac{\pi}{L}z\right)\chi_{[Z_j-L/2,Z_j+L/2]}(z)u_{(\Lambda_k,\sigma_k)}(\vec{r}).\end{aligned}\quad (2.18)$$

Here L_z and A are the height and area of the quantization volume and $\vec{k}_{||} = (k_x, k_y)$ denotes the in-plane wavevector in the 2D carrier reservoir, or a projection of the 3D wavevector $\vec{k} = (k_x, k_y, k_z) = (\vec{k}_{||}, k_z)$ onto the xy -direction.

However, in the system here, the reservoir wavefunctions are perturbed by the QDs: Unfortunately, the chosen QD wavefunctions are not orthogonal to Eq. (2.17) and (2.18). Thus, using those PW based wavefunctions would be contradictory to the assumption that the creation / annihilation operators are associated with an (orthonormal) eigenbasis of $H_{0,el}$. In practice, this would lead to an over-estimation of the Coulomb scattering rates, cf. [20]. For that purpose, a new orthonormal eigenbasis of $H_{0,el}$ will be constructed.

Orthogonalized Plane Waves

Assuming that the QDs merely cause local perturbations of the PW states, a Gram-Schmid like procedure is used to orthogonalize the reservoir states with respect to the QDs. Therefore the orthogonalization scheme suggested by Nielsen et al. [20] is used:

$$|\psi_{\mathbf{k},X}\rangle = \frac{1}{N_{\mathbf{k},X}} \left(|\psi_{\mathbf{k},X}^0\rangle - \sum_l \langle\psi_l|\psi_{\mathbf{k},X}^0\rangle |\psi_l\rangle \right) \quad (2.19)$$

$N_{\mathbf{k},X}$ is a normalization factor of the form

$$N_{\mathbf{k},X} = \sqrt{1 - \sum_l |\langle \psi_l | \psi_{\mathbf{k},X}^0 \rangle|^2}, \quad (2.20)$$

X is a placeholder describing the reservoir state and $|\psi_l\rangle$ denotes the states to which the PW should be orthogonalized. Note that Eqs. (2.19) and (2.20) explain just the orthogonalization scheme, details can be found in Appx. A. In the following the orthogonalized plane waves (OPWs) basis states will be denoted by $|\psi_{\mathbf{k},X}\rangle$.

In contrast to an original Gram-Schmidt procedure, the new basis is not orthogonal by construction, rather the sum includes only a few states of the quantum structures, and the new reservoir states are not orthogonalized to each other. A full Gram-Schmidt procedure (cf. [48]) would not be manageable in practice due to the extremely large number of reservoir states. However, Nielsen et al. showed [20] orthogonality of the new basis states within the thermodynamic limit. Without going into further detail, it should be noted that the transition to the thermodynamic limit seems an appropriate approximation for the in-plane part of the wavefunctions, but a difficult one for the z-direction. For more details see Appx. A.

Standard use OPWs

For a system containing QDs embedded in a 2D carrier reservoir, Nielsen et al. also showed that it is sufficient to orthogonalize the in-plane part of the 2D carrier reservoir wavefunctions with respect to QD states [20]. Under the assumption used here of equal z-wavefunctions for QDs and 2D carrier reservoir, this proves to be exact. As a result, the wavefunctions

$$|\psi_{\mathbf{k},2DCR}\rangle = \frac{1}{N_{\mathbf{k},2D}} \left(|\varphi_{k_{\parallel}}^0\rangle - \sum_{\substack{v \in \text{QD} \\ \Lambda_v = \Lambda_k, \sigma_v = \sigma_k}} \langle \varphi_v | \varphi_{k_{\parallel}}^0 \rangle |\varphi_v\rangle \right) |\xi_{\mathbf{k}}\rangle |u_{(\Lambda_k, \sigma_k)}\rangle \quad (2.21)$$

are used for the 2D carrier reservoir. Note that band- and spin indices are fixed for the QD states entering the sum. In contrast, for the 3D carrier reservoir, the orthogonalization Eq. (2.19) is applied to the full 3D wavefunctions $\psi_{\vec{k}}(\vec{r})$ unless noted:

$$|\psi_{\mathbf{k},3DCR}\rangle = \frac{1}{N_{\mathbf{k},3D}} \left(|\psi_{\mathbf{k},3D}^0\rangle - \sum_l \langle \psi_l | \psi_{\mathbf{k},3D}^0 \rangle |\psi_l\rangle \right) =: |\psi_{\mathbf{k},3DCR}\rangle. \quad (2.22)$$

This is the most general ansatz using the orthogonalization scheme (2.19), as the full 3D wavefunctions enter. However, it should be noted that wavefunctions Eq. (2.22) are no longer decomposable into z- and in-plane-parts.

Unless otherwise noted, OPWs Eqs. (2.21) and (2.22) have been used in Chap. 4. In Chap. 5, the OPWs Eq. (2.21) have been used.

Further possible OPWs for bulk states

Instead of orthogonalization with respect to the full 3D wavefunctions in according to Eq. (2.22), the question arises whether it is sufficient to orthogonalize the 3D states

2. Setting of the model systems and the theoretical framework

with respect to:

1. The QD in-plane wavefunctions,

$$|\psi_{\mathbf{k},2\text{DOPW}}\rangle = \frac{1}{N_{2D}(\vec{k}_{\parallel})} \left(|\varphi_{k_{\parallel}}^0\rangle - \sum_{\substack{v \in \text{QD} \\ \Lambda_v = \Lambda_k, \sigma_v = \sigma_k}} \langle \varphi_v | \varphi_{k_{\parallel}}^0 \rangle |\varphi_v\rangle \right) |\phi_{k_z}^0\rangle |u_{(\Lambda_k, \sigma_k)}\rangle. \quad (2.23)$$

2. The z-direction

$$|\psi_{\mathbf{k},z\text{OPW}}\rangle = \frac{1}{N_z(k_z)} |\varphi_{k_{\parallel}}^0\rangle \left(|\phi_{k_z}^0\rangle - \sum_{\text{QD layer } l}^{N_{2D}} \langle \xi_l | \phi_{k_z}^0 \rangle |\xi_l\rangle \right) |u_{(\Lambda_k, \sigma_k)}\rangle. \quad (2.24)$$

3. The in-plane and z-direction separately³

$$\begin{aligned} |\psi_{\mathbf{k},2\text{D}\times z\text{OPW}}\rangle &= \frac{1}{N_{2D}(\vec{k}_{\parallel})N_z(k_z)} \left(|\varphi_{k_{\parallel}}^0\rangle - \sum_{\substack{v \in \text{QD} \\ \Lambda_v = \Lambda_k, \sigma_v = \sigma_k}} \langle \varphi_v | \varphi_{k_{\parallel}}^0 \rangle |\varphi_v\rangle \right) \\ &\quad \times \left(|\phi_{k_z}^0\rangle - \sum_{\text{QD layer } l}^{N_{2D}} \langle \xi_l | \phi_{k_z}^0 \rangle |\xi_l\rangle \right) |u_{(\Lambda_k, \sigma_k)}\rangle. \end{aligned} \quad (2.25)$$

Here the normalization factors have the form

$$N_{2D}(\vec{k}_{\parallel}) = \sqrt{1 - \sum_{\substack{v \in \text{QD} \\ \Lambda_v = \Lambda_k, \sigma_v = \sigma_k}} |\langle \varphi_v | \varphi_{k_{\parallel}}^0 \rangle|^2}, \quad (2.26)$$

for the in-plane wavefunctions, respective

$$N_z(k_z) = \sqrt{1 - \sum_{\text{QD layer } l}^{N_{2D}} |\langle \xi_l | \varphi_{k_z}^0 \rangle|^2}, \quad (2.27)$$

for the z-component. Note that the band- and spin-indices are fixed in the sum over all QD states v in the 2D reservoir.

All of these wavefunctions have in common that they are possible eigenbases of $H_{0,el}$. So in principle, they are in agreement with the assumptions considered. Furthermore, Eqs. (2.23)–(2.25) have in common that they all retain the factorizability of the 3D carrier reservoir wavefunctions, which was lost in Eq. (2.22). A disadvantage of the basis Eq. (2.22) is that these wavefunctions are not orthogonal to the 2D ones Eq. (2.23). An extension of the QD-2D model to a full QD-2D-3D model would be advantageous, but relatively costly, since it would require construction a new eigenbasis.. By contrast, this would not be necessary for the basis Eq. (2.24) and Eq. (2.25).

³This basis was chosen in Ref. [49].

2.5. Coulomb matrix

Use of the Fourier representation of the Coulomb potential, the unscreened Coulomb matrix elements are:

$V_{abcd} = - \int d^3r \int d^3r' \psi_a^*(\vec{r}) \psi_b^*(\vec{r}') V(|\vec{r} - \vec{r}'|) \psi_d(\vec{r}') \psi_c(\vec{r})$ can be expressed as⁴ [50]:

$$\begin{aligned}
V_{abcd} &= - \delta_{R_z^a, R_z^c} \delta_{R_z^b, R_z^d} \delta_{R_z^a, R_z^b} \frac{\delta_{\Lambda_a, \Lambda_c} \delta_{\Lambda_b, \Lambda_d} \delta_{\sigma_a, \sigma_c} \delta_{\sigma_b, \sigma_d}}{A} \\
&\times \sum_{\vec{q}_{||}} \frac{e_0^2}{2\epsilon q_{||}} \int dz \int dz' \xi_a^*(z) \xi_b^*(z') e^{-q_{||}|z-z'|} \xi_d(z') \xi_c(z) \\
&\times \int d^2r_{||} \varphi_a^*(\vec{r}_{||}) \varphi_c(\vec{r}_{||}) e^{-i\vec{q}_{||} \cdot \vec{r}_{||}} \int d^2r'_{||} \varphi_b^*(\vec{r}'_{||}) \varphi_d(\vec{r}'_{||}) e^{i\vec{q}_{||} \cdot \vec{r}'_{||}} \\
&=: \sum_{\vec{q}_{||}} V_{\vec{q}_{||}}^{2D}, \tag{2.28}
\end{aligned}$$

to describe the QD-2D sample and

$$\begin{aligned}
V_{abcd} &= - \frac{\delta_{\Lambda_a, \Lambda_c} \delta_{\Lambda_b, \Lambda_d} \delta_{\sigma_a, \sigma_c} \delta_{\sigma_b, \sigma_d}}{AL_z} \sum_{\vec{q}} \frac{e_0^2}{\epsilon(q_{||}^2 + q_z^2)} \\
&\times \int d^3r \hat{\psi}_a^*(\vec{r}) \hat{\psi}_c(\vec{r}) e^{-i\vec{q} \cdot \vec{r}} \int d^3r' \hat{\psi}_b^*(\vec{r}') \hat{\psi}_d(\vec{r}') e^{i\vec{q} \cdot \vec{r}'} \\
&=: \sum_{\vec{q}} V_{\vec{q}}^{3D}, \tag{2.29}
\end{aligned}$$

for the description of the QD-3D sample. If dimensionality is not specified, the notation $V_{\vec{q}}$ will be used. The Kronecker-deltas $\delta_{R_z^a, R_z^c}$ and $\delta_{R_z^b, R_z^d}$ in Eq. (2.28) are a consequence of the strong confinement in z direction of the nanostructures, cf. Eq. (2.16). The Kronecker delta $\delta_{R_z^a, R_z^b}$ expresses the assumption that only interactions within one layer are considered. Note that this is only an assumption. Here it is justified as the distance of the different QD layers to each other is assumed to be sufficiently large. The further Kronecker-deltas in the numerators of Eqs. (2.28) and (2.29) originate from the scalar product of Bloch spin part, cf. Eq. (2.13). They describe that the scattered carriers keep their spin and no inter-band processes appear. Therefore, it was assumed that the Coulomb potential is quasi constant on the length scales of the Bloch functions, cf. [50, 20, 39]. Furthermore, in Eq. (2.28) the factorizability of the envelope was used.

The in-plane part of Coulomb matrix elements are tabulated in Ref. [46]. The Coulomb integrals for the z -direction can be found in Refs. [51, 52] for the 3D sample, and in Ref. [2] for the 2D samples.

⁴ $\vec{q} = (\vec{q}_{||}, q_z) = (q_x, q_y, q_z)$

2. Setting of the model systems and the theoretical framework

2.5.1. Screening

In the model used here, screening effects are included “by hand”⁵, in terms of screened Coulomb matrix elements

$$W_{\vec{q}} := \frac{V_{\vec{q}}}{\epsilon(q, \omega)}. \quad (2.30)$$

Motivation of the dielectric function $\epsilon(q, \omega)$, can be found in Sec. C and in more detail in Ref. [39]. In this thesis $\epsilon(q, \omega)$ is considered within the static limit ($\omega = 0$) of the Lindhard formula.

Screening in a quasi two-dimensional material

Following [39], in a quasi two-dimensional system like a WL or a QW, the static dielectric function $\epsilon(q, 0)$ has the form

$$\epsilon(q, 0) = 1 + \frac{\kappa_{2D}}{q}. \quad (2.31)$$

κ_{2D} is the so called *screening wavenumber*

$$\kappa_{2D} = \sum_{\lambda=e,h} \frac{e_0^2}{2\epsilon} \left(\frac{\partial n_{2D}^\lambda}{\partial \mu_{2D}^\lambda} \right). \quad (2.32)$$

Assuming a Fermi-distributed occupation in the respective bands, with the 2D chemical potential [39]

$$\mu_{2D}^\lambda = k_B T \ln \left[e^{\frac{n_{2D}^\lambda \hbar^2 \pi}{m_\lambda k_B T}} - 1 \right], \quad (2.33)$$

the derivative of the carrier (area-)density n_{2D}^λ with respect to μ_{2D}^λ can be determined analytically. This leads to

$$\kappa_{2D}(n_{2D}^e, n_{2D}^h) = \sum_{\lambda=e,h} \frac{m_\lambda e_0^2}{2\pi\epsilon\hbar^2} \left[1 - \exp\left(-\frac{\hbar^2 \pi n_{2D}^\lambda}{k_B T m_\lambda}\right) \right]. \quad (2.34)$$

Screening in a three dimensional material

Here, $\epsilon(q, 0)$ has the form

$$\epsilon(q, 0) = 1 + \frac{\kappa_{3D}^2}{q_{\parallel}^2 + q_z^2}, \quad (2.35)$$

⁵It is possible to deduce screening effects from the derivation of the EOM, so that the incorporation of screening is not just a phenomenological model assumption.

with the 3D screening wavenumber

$$\kappa_{3D} = \sqrt{\sum_{\lambda=e,h} \frac{e_0^2}{\varepsilon} \left(\frac{\partial n_{3D}^\lambda}{\partial \mu_{3D}^\lambda} \right)}. \quad (2.36)$$

For a Fermi-distributed carrier occupation, it is not possible to evaluate Eq. (2.36) analytically. A typical simplification leading to an analytical result is to assume a Boltzmann distributed carrier occupation instead: One achieves the ‘‘Debye-Hückel’’ screening wavenumber

$$\kappa_{\text{Debye}} = \sqrt{\frac{\sum_{\lambda=e,h} n_{3D}^\lambda}{\varepsilon k_B T}}. \quad (2.37)$$

A more accurate approximation is used in this thesis. As described in the book of Haug and Koch [39], Joyce and Dixon [53] and Aguilera-Navarro et al. [54] found an analytical approximation for $\frac{\mu_{3D}^\lambda}{k_B T}$ that is very accurate over a wide density range:

$$\beta \mu_{3D}(n_{3D}^\lambda) \approx \ln \left[\frac{n_{3D}^\lambda}{n_0^\lambda} \right] + 4.897 \ln \left[0.045 \frac{n_{3D}^\lambda}{n_0^\lambda} + 1 \right] + 0.133 \frac{n_{3D}^\lambda}{n_0^\lambda}, \quad (2.38)$$

with the normalization constant

$$n_0^\lambda = \frac{1}{4} \left(\frac{2m_\lambda k_B T}{\hbar^2 \pi} \right)^{3/2}. \quad (2.39)$$

Using the inverse derivative yields

$$\begin{aligned} \frac{\partial n_{3D}^\lambda}{\partial \mu_{3D}^\lambda}(n_{3D}^\lambda) &= \left(\frac{\partial \mu_{3D}^\lambda}{\partial n_{3D}^\lambda} \right)^{-1} (n_{3D}^\lambda) \\ &\approx 0.133 + \frac{0.220365}{1 + 0.045 \frac{n_{3D}^\lambda}{n_0^\lambda}} + \frac{n_0^\lambda}{n_{3D}^\lambda}. \end{aligned} \quad (2.40)$$

And finally

$$\kappa_{\text{Joyce}} = \sqrt{\sum_{\lambda=e,h} \frac{e_0^2}{\varepsilon} \left(0.133 + \frac{0.220365}{1 + 0.045 \frac{n_{3D}^\lambda}{n_0^\lambda}} + \frac{n_0^\lambda}{n_{3D}^\lambda} \right)}. \quad (2.41)$$

2. Setting of the model systems and the theoretical framework

From Fig. 2.7 one can see, that the difference between Debye-Hückel screening wavenumber and the one calculated via the approximation of Ref. [53, 54] is small.

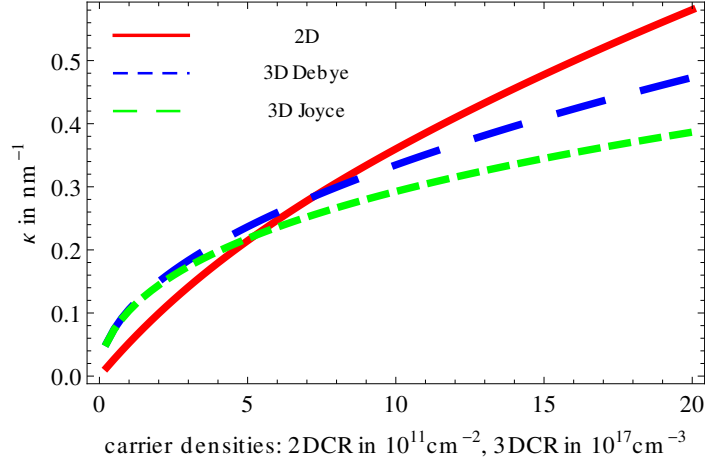


Figure 2.7.: Screening wavenumber κ for a 2D carrier reservoir, for a 3D carrier reservoir after Debye-Hückel, and via the approximation of Ref. [53, 54]. Equal carrier densities $n_{3D}^e = n_{3D}^h$ and $n_{2D}^e = n_{2D}^h$ are assumed. Parameters from Tab. F.2

Furthermore Fig. 2.7 shows that for this set of parameters, κ_{2D} is smaller than κ_{3D} for small carrier densities, crosses κ_{3D} , at carrier densities of about $7 \times 10^{11} \text{ cm}^{-2}$ (respective $7 \times 10^{17} \text{ cm}^{-3}$), and goes on with a higher slope. Note that a comparison of κ_{3D} and κ_{2D} cannot be exactly transferred onto the screening due to variance in dependency on κ , cf. Eq. (2.35), (2.31).

3. Equations of motion

In the previous chapter the model system was introduced: On the one hand, the nanostructures under investigation were described. On the other, the Hamiltonian, which defines the considered interactions, was introduced. Via the definition of the model system, it was possible to choose a suitable eigenbasis for the system. This is necessary for the calculation of all quantities in the Hamiltonian - here the Coulomb matrix. The last section was closed with a short discussion of screening corrections to the Coulomb matrix elements. In summary, the previous chapter defined both, the physical system and the theoretical settings under investigation. With all significant quantities well-defined, system dynamics can be determined. This will be done in this chapter.

This chapter is structured as follows: In Sec. 3.1 the quantities of interest will be introduced. Section 3.2, describes the analytical approach to setting up the equations of motion. These will be discussed in Sec. 3.3. Finally Sec. 3.4 describes numerical integration methods.

3.1. Quantities of interest

A fundamental condition for lasing is carrier population inversion. So the dynamics of the occupation probability of the laser states, here the QD ground state, is of interest. Those dynamics are coupled to carrier occupation in other system states. The time evolution of the microscopic polarization, which is related to the material gain and the refractive index, is also of interest, cf. Appx. E.

These quantities can be described by the diagonal- and off-diagonal elements of the density matrix ρ . Within the frame-work of second quantization [39], elements of the density matrix can be expressed via expectation values of the form

$$\rho_{xy} = \langle a_x^\dagger a_y \rangle \text{ (arbitrary system state),} \quad (3.1)$$

$$\rho_x := \rho_{xx} = \langle a_x^\dagger a_x \rangle \text{ (diagonal element } \hat{=} \text{ occupation probability),} \quad (3.2)$$

$$p_{nm} = \langle a_m^\dagger a_n \rangle \text{ (inter-band polarization, with different band indices } \Lambda_m \neq \Lambda_n), \quad (3.3)$$

where the multi-indices introduced in Sec. 2.2 have been used.

3.2. Hierarchy problem and Cluster Expansion

The dynamics of the system quantities under investigation can be described via their Heisenberg equation of motion (EOM):

$$\begin{aligned} \frac{d}{dt}\rho_{xy} &= \frac{i}{\hbar}\langle [H, a_x^\dagger a_y] \rangle + \frac{i}{\hbar}\langle \frac{\partial a_x^\dagger a_y}{\partial t} \rangle \\ &= \frac{i}{\hbar}\langle (H a_x^\dagger a_y - a_x^\dagger a_y H) \rangle + \frac{i}{\hbar}\langle \frac{\partial a_x^\dagger a_y}{\partial t} \rangle. \end{aligned} \quad (3.4)$$

Since these system quantities exhibit no explicit time dependency, the partial-time derivative is zero.

The Hamiltonian Eq. (2.11) under consideration contains the Coulomb interaction. It is well known that the inclusion of a two-particle interaction of this type leads to the *hierarchy problem* [39]: The EOM of single-particle expectation values $\langle a_x^\dagger a_y \rangle$ couples to two-particle expectation values $\langle a_i^\dagger a_j^\dagger a_l a_m \rangle$, the dynamics of the two-particle expectation values couple to three-particle expectation values $\langle a_i^\dagger a_j^\dagger a_l^\dagger a_m a_n a_o \rangle$ and so on. Obviously, in an N-particle system this hierarchy of coupled equations ends at N+1 particle expectation values, as they are exactly zero. Nevertheless, a closed non-perturbative treatment is feasible only in few particle systems, cf. [55]). For the description of many-particle systems, there are a variety of approaches to overcome the hierarchy problem, cf. [56, 57]. In this thesis a *cluster expansion* will be used.

3.2.1. A short description of the cluster expansion

The cluster expansion [39] is an established method, used in various branches of physics. The idea behind the technique is to decompose a many particle expectation value, into (known) terms of expectation values of fewer (*here*: single-)particles plus a rest. This rest contains information about the many-particle correlation effects. That is why they are denoted as correlation terms.

The decomposition of the many-particle expectation values is done via the following

recursive scheme, which also defines the correlation terms [39, 58, 59, 2]:

$$\langle a_1^\dagger a_2 \rangle = \langle a_1^\dagger a_2 \rangle^c \quad (3.5)$$

$$\langle a_1^\dagger a_2^\dagger a_3 a_4 \rangle = \left(\langle a_1^\dagger a_4 \rangle \langle a_2^\dagger a_3 \rangle - \langle a_1^\dagger a_3 \rangle \langle a_2^\dagger a_4 \rangle \right) + \langle a_1^\dagger a_2^\dagger a_3 a_4 \rangle^c \quad (3.6)$$

$$\begin{aligned} \langle a_1^\dagger a_2^\dagger a_3^\dagger a_4 a_5 a_6 \rangle &= \langle a_1^\dagger a_6 \rangle \langle a_2^\dagger a_5 \rangle \langle a_3^\dagger a_4 \rangle - \langle a_1^\dagger a_6 \rangle \langle a_2^\dagger a_4 \rangle \langle a_3^\dagger a_5 \rangle \\ &\quad - \langle a_1^\dagger a_5 \rangle \langle a_2^\dagger a_6 \rangle \langle a_3^\dagger a_4 \rangle + \langle a_1^\dagger a_5 \rangle \langle a_2^\dagger a_4 \rangle \langle a_3^\dagger a_6 \rangle \\ &\quad - \langle a_1^\dagger a_4 \rangle \langle a_2^\dagger a_5 \rangle \langle a_3^\dagger a_6 \rangle + \langle a_1^\dagger a_4 \rangle \langle a_2^\dagger a_6 \rangle \langle a_3^\dagger a_5 \rangle \\ &\quad + \langle a_1^\dagger a_2^\dagger a_5 a_6 \rangle^c \langle a_3^\dagger a_4 \rangle + \langle a_1^\dagger a_2^\dagger a_4 a_5 \rangle^c \langle a_3^\dagger a_6 \rangle - \langle a_1^\dagger a_2^\dagger a_4 a_6 \rangle^c \langle a_3^\dagger a_5 \rangle \\ &\quad + \langle a_1^\dagger a_3^\dagger a_4 a_6 \rangle^c \langle a_2^\dagger a_5 \rangle - \langle a_1^\dagger a_3^\dagger a_5 a_6 \rangle^c \langle a_2^\dagger a_4 \rangle - \langle a_1^\dagger a_3^\dagger a_4 a_5 \rangle^c \langle a_2^\dagger a_6 \rangle \\ &\quad + \langle a_2^\dagger a_3^\dagger a_4 a_5 \rangle^c \langle a_1^\dagger a_6 \rangle + \langle a_2^\dagger a_3^\dagger a_5 a_6 \rangle^c \langle a_1^\dagger a_4 \rangle - \langle a_2^\dagger a_3^\dagger a_4 a_6 \rangle^c \langle a_1^\dagger a_5 \rangle \\ &\quad + \langle a_1^\dagger a_2^\dagger a_3^\dagger a_4 a_5 a_6 \rangle^c \end{aligned} \quad (3.7)$$

⋮

In Eqs. (3.6) and (3.7), Eq. (3.5) was already used.

Before discussing the further approach of the cluster expansion towards the derivation of a Boltzmann equation, a few words are needed about the interpretation of the correlation terms.

Correlation Terms

Correlation terms can be understood as a kind of black-box in the following sense:

For example, a two-particle expectation value contains more information about the system (and the impact of a variety of interactions on the system) than a combination of the related single-particle expectation values. A three-particle expectation value contains more information about the system than a combination of related single and two-particle expectation values. And so on... . This “more information” is stored in the correlation terms. The gain of the cluster expansion is the empirical knowledge, that in many systems, the impact of many-particle correlation terms on the system dynamics becomes very small [39]. As a result, the expansion could be truncated by neglecting the correlation term. Or literally expressed in the picture of a black-box: in many systems, the additional information stored in a $N + 1$ -particle expectation value, in comparison to the combination of $N, N - 1, \dots$ -particle expectation values, becomes negligible for higher particle numbers. Hence, the system dynamics can be expressed in terms of $N, N - 1, \dots$ -particle expectation values.

Approach to deriving the Boltzmann equation

To highlight the main ideas of the following derivation, according to [39], several notations should be introduced. With $\langle N \rangle$ an arbitrary N -particle expectation value will be denoted. The functionals $T[\cdot]$ and $V[\cdot]$ map N -particle operators onto combinations

3. Equations of motion

of N-particle operators, e.g. $T[\langle 1 \rangle] = \sum_{i,j} \Lambda_{i,j} \langle a_i^\dagger a_j \rangle + \sum_k \beta_k \langle a_x^\dagger a_k \rangle + \dots$ ¹. To emphasize that two N-particle operators within one equation are not identical, the notation $\langle N \rangle, \langle N' \rangle, \dots$ will be used. Two expectation values $\langle N \rangle$ in different equations can belong to different operators. If they explicitly belong to the same operator, they are colored.

The starting point here is $N = 1$. With the considered Hamiltonian Eqs. (2.8)–(2.11), the schematic EOM can then be expressed in the form

$$\begin{aligned} i\hbar \frac{d}{dt} \langle 1 \rangle &= T[\langle 1 \rangle] + V[\langle 2 \rangle] \\ &\stackrel{\text{Eq. (3.6)}}{=} T[\langle 1 \rangle] + \tilde{V}[\langle 1' \rangle \langle 1'' \rangle] + V[\langle 2 \rangle^c]. \end{aligned} \quad (3.8)$$

If the expansion on this level were stopped by neglecting the two-particle correlation terms, it would be denoted as *Hartree-Fock approximation*. The Hartree-Fock approximation is generally used to describe carrier density dependent shifts of the eigenenergies. To derive a Boltzmann like equation in order to incorporate scattering effects, the two-particle correlation terms must be included. Therefore, it is necessary to solve the EOM of $\langle 2 \rangle^c$:

$$i\hbar \frac{d}{dt} \langle 2 \rangle^c \stackrel{\text{Eqs. (3.6)}}{=} i\hbar \frac{d}{dt} \left[\langle 2 \rangle - \left(\langle 1' \rangle \langle 1'' \rangle - \langle 1''' \rangle \langle 1'''' \rangle \right) \right]. \quad (3.9)$$

The derivative of the single-particle expectation values has been schematically depicted in Eq. (3.8).

The derivative of the two-particle expectation value has the form

$$\begin{aligned} i\hbar \frac{d}{dt} \langle 2 \rangle &= T_{II}[\langle 2 \rangle] + V_{II}[\langle 2' \rangle, \langle 3 \rangle] \\ &\stackrel{\text{Eqs. (3.6),(3.7)}}{=} T_{II}[\langle 2 \rangle] + \tilde{V}_{II}[\langle 1 \rangle \langle 1' \rangle, \langle 1'' \rangle \langle 1''' \rangle \langle 1'''' \rangle] + \hat{V}_{II}[\langle 2'' \rangle^c, \langle 1'''' \rangle \langle 2''' \rangle^c, \langle 3 \rangle^c]. \end{aligned} \quad (3.10)$$

Neglecting the three-particle correlations, leads to the Born approximation. The EOM (3.9) can be solved by inserting Eq. (3.10) and the derivatives of the single-particle expectation values, which have the form of Eq. (3.8). Furthermore, a Markov approximation will be applied (cf. Appx. D). The solution of Eq. (3.9) can be inserted into Eq. (3.8). The derived equation thus derived contains the desired terms describing carrier-carrier scattering. It should be noted that, within the framework of this thesis, the Hartree-Fock energy renormalization, as well as the two-particle correlation contributions in Eq. (3.10), will not be taken into consideration.

The advantages of the cluster expansion are: (i) The steps taken are easy to interpret, so one still can see the physical meaning in the steps. (ii) The comparative compactness of the steps taken, at least up to second expansions (Born approximation). Nevertheless it should be noted that even a third order expansion easily becomes so demanding that it is not usable in practice (at least for a single person and "by hand" calculations).

¹ In the Liouville-Space [60] the functional T as one example, could be identified with the Liouvillian $\mathcal{L} = \frac{1}{\hbar}[H, \cdot]$ in such a way that $T[\langle a_i^\dagger a_j \rangle] = \langle \mathcal{L} a_i^\dagger a_j \rangle$, where H contains only single-particle interactions such as $H_{0,el}$ or H_{int} . However, V could not be easily identified with a two-particle Liouvillian.

3.3. Equations of motion describing carrier-carrier scattering

The following discussion will be split into two parts:

1. A discussion of Coulomb scattering in a spatial homogeneous system in Sec. 3.3.1,
2. A discussion of the equation of motion in a system with a spatially inhomogeneous carrier distribution in Sec. 3.3.2.

In this thesis, the incorporation of Coulomb scattering effects remains within the limit of the Born-Markov approximation, see Sec. 3.2.1 and Appx. D. Although Lorke et al. [24] showed that the omission of non-Markovian effects is a strong limitation², calculations within the Born-Markovian limit of Nilsson et al. [21] are in good agreement to the experimental results of Woggon et al. [61]. This indicates that the simplifications assumed here are reasonable, especially as (i) it leads to a significant reduction in numerical effort. (ii) The reservoir dimensionality is more a question of the magnitude of the scattering rates relative to each other than of the highest achievable accuracy.

In this thesis, Hartree-Fock renormalizations will not be taken into consideration. For the investigation of the reservoir dimensionality, this can be justified as follows:

If energy renormalizations for the 2D- and the 3D sample are nearly equal, they would change only the absolute value of the scattering rates. But according to the findings in Sec. 4.3.8, this would not significantly change the ratio of the scattering rates relative to each other, which is the more important quantity here.

If the energy renormalizations were very different for the 2D and the 3D samples, comparing the two samples would be hardly justified.

For the gain model, the inclusion of Hartree-renormalizations would be a useful model extension.

3.3.1. Equations in a spatially homogeneous system

In this section, discussion is restricted to effects caused by Coulomb interaction. Light-matter interaction H_{int} will be omitted in this section.

According to the Sec. 3.3.2 it is a reasonable approximation to assume a spatially homogeneous carrier reservoir, cf. Fig. 2.6. Using this assumption, Majer et al. [62], among others, achieved a close agreement between theory and experiment for the description of gain recovery dynamics in optical amplifiers³.

The EOM for the occupation probabilities ρ_x will be discussed first, in Sec. 3.3.1. They define a coupled set of rate equations suitable for the description of switch-on dynamics [63, 64], or gain recovery [62], for example. Following that, the EOM of the QD polarization p_{nm} will be discussed in Sec. 3.3.1. This can be used to achieve a microscopic description of material gain and refractive index.

Before discussing the EOM, it should be noted that screening effects in this thesis will be included “by hand”, cf. Sec. 2.5.1. This is done by substituting in the second order

² This applies particularly to the polarization dynamics, but the dynamics of the occupation probability are also strongly underestimated if the QD systems contain further shells beyond the p-shell, as pure intra QD dynamics cannot be treated within the Markovian limit.

³In Ref. [62] a dot in a well structure has been assumed.

3. Equations of motion

contribution of the scattering terms the related screened ones W_{abdc} for the Coulomb matrix elements V_{abdc} .

Note that in the following equations, the notation belongs to a valence / conduction band picture.

Dynamics of the occupation probability

Within the limit of Born-Markov approximation, the EOM of the occupation probability ρ_D in a QD state D can be cast in the form of the quantum Boltzmann equation [20, 39].

$$\begin{aligned} \dot{\rho}_D &= \frac{2\pi}{\hbar} \sum_{a,b,c} W_{Dabc} (W_{Dabc}^* - W_{Dacb}^*) \left[\rho_b \rho_c (1 - \rho_a) (1 - \rho_D) - (1 - \rho_b) (1 - \rho_c) \rho_a \rho_D \right] \\ &\quad \times \delta(\varepsilon_D + \varepsilon_a - \varepsilon_b - \varepsilon_c) \quad (3.11) \\ &= S_{\text{in}}^D (1 - \rho_D) - S_{\text{out}}^D \rho_D, \quad (3.12) \end{aligned}$$

It describes the in and out scattering of carriers into the state D in terms of the scattering rates S_{in}^D and S_{out}^D . The δ -distribution in Eq. (3.12), describing energy conservation, originates from the Markov approximation. Details of the derivation of the EOM via a cluster expansion can be found in [65, 2, 66] and Appx. D.

For the evaluation of the scattering rates, the occupation probabilities are approximated by Fermi-distributions $\rho_x = f_x$, with

$$f_x(n) = \frac{1}{1 + e^{\frac{1}{k_B T} [\varepsilon(x) - \mu_{2D/3D}^{\lambda_x}(n)]}}. \quad (3.13)$$

Here, $\varepsilon(x)$ denotes the energy of the state x , relative to the reservoir band edge, and $\mu_{2D/3D}^{\lambda_x}$ is the chemical potential of the 2D / 3D carrier reservoirs, defined in Eqs. (2.33) (μ_{2D}) and (2.38) (μ_{3D}). The usage of Fermi distributions fits with the situation of a device in a quasi equilibrium (neglecting the optical field). Furthermore, for the evaluation of the scattering rates, it is beneficial to switch into the electron-hole picture via the substitution $f_h = 1 - f_v$. Therefore, $\mu_{2D/3D}^{\lambda_x}$ describes the chemical potential for electrons ($\lambda_x = e$) respective holes ($\lambda_x = h$). However, the further description of the processes keeps the valence-/ conduction-band picture, as it leads to a more compact notation.

Dynamics of the microscopic polarization

The derivation of the polarization dynamics in the Markovian limit is similar to that of the occupation probabilities (see App. D). However, additional scattering channels appear in the polarization dynamics. Without regard to a coupling to other polarizations, the polarization dynamics can be expressed in terms of a dephasing time T_2 defined by

$$\dot{p}_{D_1 D_2} = \frac{i}{\hbar} (\varepsilon_{D_1} - \varepsilon_{D_2}) p_{D_1 D_2} - \frac{1}{T_2} p_{D_1 D_2}, \quad (3.14)$$

3.3. Equations of motion describing carrier-carrier scattering

with

$$\begin{aligned}
T_2^{-1} = \frac{\pi}{\hbar} \left\{ \right. \\
& \sum_{a,b,c} \left[W_{abD_1c} (W_{D_1cab} - W_{D_1cba}) [\rho_c(1 - \rho_b)(1 - \rho_a) + (1 - \rho_c)\rho_b\rho_a] \right. \\
& \quad \times \delta(\varepsilon_a + \varepsilon_b - \varepsilon_c - \varepsilon_{D_1}) \\
& \quad + W_{D_2abc} (W_{bcD_2a} - W_{cbD_2a}) [\rho_b\rho_c(1 - \rho_a) + (1 - \rho_b)(1 - \rho_c)\rho_a] \\
& \quad \left. \times \delta(\varepsilon_{D_2} + \varepsilon_a - \varepsilon_b - \varepsilon_c) \right] \\
& - 2 \sum_{a,c} \left(W_{aD_1D_1c} W_{D_2caD_2} - W_{aD_1D_1c} W_{D_2cD_2a} - W_{D_1aD_1c} W_{D_2caD_2} \right) [(1 - \rho_c)\rho_a] \\
& \quad \times \delta(\varepsilon_a - \varepsilon_c) \\
& - \sum_{a,b} \left(W_{abD_1D_2} W_{D_2D_1ba} \right) [\rho_{D_2}(1 - \rho_b)(1 - \rho_a) + (1 - \rho_{D_2})\rho_b\rho_a] \\
& \quad \times \delta(\varepsilon_a + \varepsilon_b - \varepsilon_{D_2} - \varepsilon_{D_1}) \\
& - \sum_{b,c} \left(W_{D_2D_1bc} W_{cbD_1D_2} \right) [\rho_b\rho_c(1 - \rho_{D_1}) + (1 - \rho_b)(1 - \rho_c)\rho_{D_1}] \\
& \quad \left. \times \delta(\varepsilon_{D_2} + \varepsilon_{D_1} - \varepsilon_b - \varepsilon_c) \right\}. \tag{3.15}
\end{aligned}$$

As will be shown in Appx. E, the T_2 -time is connected with the homogeneous line width Γ_h via the relation

$$\Gamma_h = \frac{\hbar}{T_2}. \tag{3.16}$$

The black terms of Eq. (3.15) are structurally related to the scattering rates (3.12). Therefore the dephasing time is often roughly approximated via the relation $T_2 = 2T_1$ [61], where

$$T_1 = \frac{1}{\sum_i S_i} \tag{3.17}$$

equates the sum over all scattering processes in and out of the states D_1 and D_2 .

However, in contrast to the scattering rates so called *pure dephasing processes* have to be taken into account. These processes describe scattering events which in total do not change the occupation probability of the QD levels under consideration. Therefore they cancel each other in the scattering rates. The pure dephasing processes give rise to additional terms in the black section of Eq. (3.15). These are partly compensated for by the blue terms in Eq. (3.15), where the first line also describes pure dephasing processes. Here, the pure dephasing terms are independent of the occupation probability

3. Equations of motion

of the QD states. Only the 2D carrier reservoir occupation factor $\rho_k(1 - \rho_k)$ enters into these contributions, as can be seen from the first [blue](#) line.

The [blue](#) terms have a different origin than the black ones, cf. Appx. D. They are structurally related to the off-diagonal contributions [39, 67, 24]. These terms mainly describe coupling between different polarizations. However, coupling to other polarizations is not considered in this thesis. There are works [24, 68, 67] pointing out the importance of those couplings. In these models, the definition of a dephasing in terms of a T_2 -time is no longer useful. The homogeneous linewidth can then be achieved by a Lorentzian fit to the QD peaks of the gain spectra, cf. [69, 70].

However, there are many models that remain on the level of an (effective) T_2 -time, achieving close agreement between theory and experiment [21, 62]. For the purposes of this thesis the approximation performed seems appropriate.

For the evaluation of the dephasing time as well, the occupation probabilities are approximated by Fermi distributions $\rho_x = f_x$, with the chemical potential Eq. (2.33), and the final evaluation is done in the electron-hole picture via the transformation $f^v \rightarrow 1 - f^h$, see Sec. 3.3.1.

3.3.2. Equations in a system with an inhomogeneous carrier density

What primarily emerges from this section is it is not necessary to set up a spatially resolved theory for the Coulomb processes addressed in this thesis. Thus one could skip this section on first reading. However, given the conditions in a real device, this is not obvious.

As discussed in Sec. 2.1.3, the carrier density distribution in the device is spatially inhomogeneous. The validity of the assumption of a homogeneous system is particularly questionable in a 3D-0D device, since the carrier concentration in bulk material varies greatly throughout the device. In principle, this makes a spatially resolved theory necessary.

The most pragmatic approach to handling this problem, would be to split the device into fictive compartments. Each of these compartments could be assumed as an effective quantization volume with a homogeneous carrier density (cf. Ref. [71]). However, this would cause several problems: (i) the apparent artificial discontinuity on borders of the various quantization volumes would inhibit a spatio-temporal device description, and (ii) small parcels, containing only several tens of QDs, would adulterate assumptions concerning the OPW orthogonality, cf. [20]. Kuhn, Hess, Rossi and Steininger et al. [72, 73, 44, 74] solved this problem via a *gradient expansion*: Instead of describing the laser system states in terms of occupation probabilities ρ_x and polarizations p_{nm} , they set up the EOM for the *Wigner representatives* of the different quantities. This concept will be used to derive spatially resolved EOM for the QDs. Note that this spatially resolved EOM is not suitable for the descriptions of a device with inhomogeneities that cause different Bloch functions, cf. Ref. [44].

Derivation

One first has to introduce relative coordinates

$$\vec{Q} := \frac{\vec{k} + \vec{k}'}{2} \quad \vec{q} := \vec{k} - \vec{k}'. \quad (3.18)$$

The Wigner representatives are then given by the Fourier transformed inter-band (for the polarizations p_{nm}) and intra-band (for the occupation probabilities) polarizations of the form⁴

$$\rho_{\mathbf{Q}}(\vec{r}) = \sum_{\vec{q}} e^{i\vec{q}\cdot\vec{r}} \rho_{\mathbf{Q}-\frac{\mathbf{q}}{2}, \mathbf{Q}+\frac{\mathbf{q}}{2}}, \quad (3.19)$$

$$p_{\mathbf{Q}\mathbf{Q}}(\vec{r}) = \sum_{\vec{q}} e^{i\vec{q}\cdot\vec{r}} p_{\mathbf{Q}-\frac{\mathbf{q}}{2}, \mathbf{Q}+\frac{\mathbf{q}}{2}}, \quad \text{for interband polarizations.} \quad (3.20)$$

This definition fails in QD materials, since there is no wavevector defined. For this purpose, the gradient expansion of Kuhn et al. is not directly transferable. One might solve this problem by setting up the related spatially resolved EOM for the reservoir and determines the QD in scattering rate via the reservoir out scattering rate at position of the QD. However, this causes further difficulties, since the reservoir density at a certain point is also affected by QDs in the surrounding, due to the delocalized nature of the eigenfunctions. Therefore here another ansatz will be used: The QD position vector \vec{R} is by definition a quantum number for the QD states. As a result, the EOM of a QD state ρ_D is inherently position-dependent. So the task is to include spatial dependency of the reservoir occupation probabilities in the quantum Boltzmann equation, cf. Refs. [75, 71, 76]. In order to write QD and reservoir density matrix elements formally in the same manner, the notation

$$\begin{aligned} \rho_{(X-\frac{\alpha}{2}), (X+\frac{\alpha}{2})} &:= \delta_{\alpha, y} \rho_{DD} \\ &\quad , \text{ for } X \in \text{QD}, \alpha \in \text{Reservoir}, \\ \delta_{(X-\frac{\alpha}{2}), (X+\frac{\alpha}{2})} &:= \delta_{\alpha, y} \delta_{D, D} \end{aligned} \quad (3.21)$$

will be used. Here y denotes an arbitrary reservoir state.

The starting point for the derivation of the spatially dependent quantum Boltzmann equation is the general EOM for the QD state occupation probability in Born-Markov approximation, before omitting off-diagonal terms by applying a *random phase approximation* [39].

⁴ For definitions of the multi-indices, see Sec. 2.2. The comma in $\rho_{\mathbf{Q}-\frac{\mathbf{q}}{2}, \mathbf{Q}+\frac{\mathbf{q}}{2}}$ and $p_{\mathbf{Q}-\frac{\mathbf{q}}{2}, \mathbf{Q}+\frac{\mathbf{q}}{2}}$ is just an optical placeholder and has no further meaning.

3. Equations of motion

$$\begin{aligned}
\dot{\rho}_D = & -\frac{\pi}{2\hbar} \sum_{a,b,c} \sum_{U,X,Y,Z} \left\{ \right. \\
& (W_{abDc} - W_{baDc})(W_{UXYZ} - W_{XUYZ}) \\
& \times \left[\rho_{U,D} \rho_{X,c} (\delta_{b,Y} - \rho_{b,Y}) (\delta_{a,Z} - \rho_{a,Z}) - (\delta_{U,D} - \rho_{U,D}) (\delta_{X,c} - \rho_{X,c}) \rho_{b,Y} \rho_{a,Z} \right] \\
& \times \delta(\varepsilon_Z + \varepsilon_Y - \varepsilon_X - \varepsilon_U) \\
& - (W_{Dabc} - W_{Dacb})(W_{UXYZ} - W_{UXZY}) \\
& \times \left[\rho_{U,b} \rho_{X,c} (\delta_{a,Y} - \rho_{a,Y}) (\delta_{D,Z} - \rho_{D,Z}) - (\delta_{U,b} - \rho_{U,b}) (\delta_{X,c} - \rho_{X,c}) \rho_{D,Y} \rho_{a,Z} \right] \\
& \left. \times \delta(\varepsilon_U + \varepsilon_X - \varepsilon_Y - \varepsilon_Z) \right\} \quad (3.22)
\end{aligned}$$

This equation also appears in the derivation of the homogeneous quantum Boltzmann equation (3.11), cf. Ref. [2] and in Eqs. D.13 and D.14. However, instead of restricting the EOM to diagonal elements as in the spatially homogeneous system intra-band reservoir polarizations will also be taken into account. Using relative momenta Eq. (3.18) and the notation Eq. (3.21), Eq. (3.22) can be expressed as

$$\begin{aligned}
& \dot{\rho}_D(\vec{R}) \\
= & \frac{2\pi}{\hbar} \left\{ \sum_{X,Y,Z} \sum_{\alpha,\beta,\gamma} W_{D(X-\frac{\alpha}{2})(Y+\frac{\beta}{2})(Z+\frac{\gamma}{2})} \right. \\
& \left(W_{(Y-\frac{\beta}{2})(Z-\frac{\gamma}{2})D(X+\frac{\alpha}{2})} - W_{(Z-\frac{\gamma}{2})(Y-\frac{\beta}{2})D(X+\frac{\alpha}{2})} \right) \\
& \times \left[\rho_{(Y-\frac{\beta}{2})(Y+\frac{\beta}{2})} \rho_{(Z-\frac{\gamma}{2})(Z+\frac{\gamma}{2})} (\delta_{(X-\frac{\alpha}{2})(X+\frac{\alpha}{2})} - \rho_{(X-\frac{\alpha}{2})(X+\frac{\alpha}{2})}) (1 - \rho_D(\vec{R})) \right. \\
& \left. - (\delta_{(Y-\frac{\beta}{2})(Y+\frac{\beta}{2})} - \rho_{(Y-\frac{\beta}{2})(Y+\frac{\beta}{2})}) (\delta_{(Z-\frac{\gamma}{2})(Z+\frac{\gamma}{2})} - \rho_{(Z-\frac{\gamma}{2})(Z+\frac{\gamma}{2})}) \rho_{(X-\frac{\alpha}{2})(X+\frac{\alpha}{2})} \rho_D(\vec{R}) \right] \\
& \left. \times \delta(\varepsilon_D + \varepsilon_{X-\frac{\alpha}{2}} - \varepsilon_{Y+\frac{\beta}{2}} - \varepsilon_{Z+\frac{\gamma}{2}}) \right\} \quad (3.23)
\end{aligned}$$

The spatial dependency of the reservoir carrier density is incorporated into the EOM via the phase factor of the Coulomb matrix elements. In the Appendix of Ref. [20] and in Eq. (A.5), it is shown that Coulomb integrals, which contain QD states, exhibit a phase factor, so that

$$\begin{aligned}
W_{D(X-\frac{\alpha}{2})(Y+\frac{\beta}{2})(Z+\frac{\gamma}{2})} & \sim e^{i[(\vec{Z}+\frac{\vec{\gamma}}{2})+(\vec{Y}+\frac{\vec{\beta}}{2})-(\vec{X}-\frac{\vec{\alpha}}{2})]\cdot\vec{R}}, \\
W_{(Y-\frac{\beta}{2})(Z-\frac{\gamma}{2})D(X+\frac{\alpha}{2})} & \sim e^{-i[(\vec{Z}-\frac{\vec{\gamma}}{2})+(\vec{Y}-\frac{\vec{\beta}}{2})-(\vec{X}+\frac{\vec{\alpha}}{2})]\cdot\vec{R}} \sim W_{(Z-\frac{\gamma}{2})(Y-\frac{\beta}{2})D(X+\frac{\alpha}{2})}. \quad (3.24)
\end{aligned}$$

With the related adjointed respective exchange terms, one can see that the phase factor

$$e^{i[(Z+\frac{\gamma}{2})+(Y+\frac{\beta}{2})-(X-\frac{\alpha}{2})]\cdot\vec{R}} e^{-i[(Z-\frac{\gamma}{2})+(Y-\frac{\beta}{2})-(X+\frac{\alpha}{2})]\cdot\vec{R}} = e^{i\vec{\alpha}\cdot\vec{R}} e^{i\vec{\beta}\cdot\vec{R}} e^{i\vec{\gamma}\cdot\vec{R}} \quad (3.25)$$

is incorporated into the EOM (3.23). It is useful to draw the phase factors out of the

3.3. Equations of motion describing carrier-carrier scattering

Coulomb matrix elements. $W =: e^{-i\vec{\Gamma}\cdot\vec{R}}\hat{W}$ ⁵. The next step is a further reduction of the number of intra-band polarizations, taken into account: Thus far, the considered states $\vec{X} \pm \frac{\vec{\alpha}}{2}$ form a complete basis in the subspace of the reservoir. Now, only small vectors $\vec{\alpha}$ will be considered. In the picture of the density matrix, the restriction of the $\vec{\alpha}$ -sum corresponds to a restriction to diagonal elements and elements in the near surroundings. In the picture of the \vec{k} -space, in which the definitions Eq. (3.18) $\vec{X} = \frac{\vec{k}+\vec{k}'}{2}$, $\vec{\alpha} = \vec{k} - \vec{k}'$ were introduced, this corresponds to assuming $\vec{k}' = \vec{k} - \Delta\vec{k}$, with small $|\Delta\vec{k}|$. Despite that simplification, many more elements of the density matrix are included for the spatially resolved EOM than in the homogeneous system for the Boltzmann equation. For small wavevectors $\vec{\alpha}, \vec{\beta}, \vec{\gamma}$, the approximations

$$W_{D(X-\frac{\alpha}{2})(Y+\frac{\beta}{2})(Z+\frac{\gamma}{2})} \approx W_{DXYZ} \quad \text{and} \quad \varepsilon_{X-\frac{\alpha}{2}} \approx \varepsilon_X \quad (3.26)$$

seems to be appropriate. The EOM (3.23) then simplifies to

$$\begin{aligned} \dot{\rho}_D(\vec{R}) &= \frac{2\pi}{\hbar} \left\{ \sum_{X,Y,Z} \sum_{\alpha,\beta,\gamma} e^{i(\vec{\alpha}+\vec{\beta}+\vec{\gamma})\cdot\vec{R}} \hat{W}_{DXYZ} (\hat{W}_{YZDX} - \hat{W}_{ZYDX}) \right. \\ &\times \left[\rho_{(Y-\frac{\beta}{2})(Y+\frac{\beta}{2})} \rho_{(Z-\frac{\gamma}{2})(Z+\frac{\gamma}{2})} (\delta_{(X-\frac{\alpha}{2})(X+\frac{\alpha}{2})} - \rho_{(X-\frac{\alpha}{2})(X+\frac{\alpha}{2})}) (1 - \rho_D(\vec{R})) \right. \\ &- (\delta_{(Y-\frac{\beta}{2})(Y+\frac{\beta}{2})} - \rho_{(Y-\frac{\beta}{2})(Y+\frac{\beta}{2})}) (\delta_{(Z-\frac{\gamma}{2})(Z+\frac{\gamma}{2})} - \rho_{(Z-\frac{\gamma}{2})(Z+\frac{\gamma}{2})}) \rho_{(X-\frac{\alpha}{2})(X+\frac{\alpha}{2})} \rho_D(\vec{R}) \left. \right] \\ &\times \delta(\varepsilon_D + \varepsilon_X - \varepsilon_Y - \varepsilon_Z) \left. \right\} \\ &\stackrel{\text{Eq. (3.20)}}{=} \frac{2\pi}{\hbar} \left\{ \sum_{X,Y,Z} \hat{W}_{DXYZ} (\hat{W}_{YZDX} - \hat{W}_{ZYDX}) \right. \\ &\times \left[\rho_Y(\vec{R}) \rho_Z(\vec{R}) (1 - \rho_X(\vec{R})) (1 - \rho_D(\vec{R})) - (1 - \rho_Y(\vec{R})) (1 - \rho_Z(\vec{R})) \rho_X(\vec{R}) \rho_D(\vec{R}) \right] \\ &\times \delta(\varepsilon_D + \varepsilon_X - \varepsilon_Y - \varepsilon_Z) \left. \right\} \quad (3.27) \end{aligned}$$

For the previous equation, the definition of the Wigner distribution Eq. (3.20) was used. The EOM has the same structure as Eq. (3.11), however position-dependent carrier occupation probabilities enter Eq. (3.27). For further evaluation of the scattering rates (and T_2 -time), refer to Eq. (3.11), describing Coulomb scattering in a spatially homogeneous system. Nevertheless, one should keep in mind that spatial effects could be in principle included.

The advantage of the method outlined above is that no artificial discontinuities appear, as would be the case for a segmented quantization volume. This is of great importance for consistent description of reservoir dynamics. Similar results appeared in Ref. [77] and it can be assumed that T. Kuhn et al. also performed similar calculations [44] to achieve a spatially resolved description carrier scattering, although they are not explicitly shown. However, these works are about 3D respective 2D materials where due to momentum conservation less simplifications are necessary.

It is important to note that Eq. (3.26) leads to a reduction in the spatial resolution, or to put it into another way: It is not the reservoir density at the QD that enters the

⁵ $\vec{\Gamma}$ is an arbitrary wavevector, depending on the matrix-element.

3. Equations of motion

EOM, but rather the average reservoir density in an area around the QD.

About spatial resolution

To provide a brief estimate: The first Brillouin zone in GaAs is extended up to $|\vec{k}| = 5\text{nm}^{-1}$. For an evaluation of the scattering rates, an integration domain of up to ca. $|\vec{k}_{\text{max}}| = 1.2\text{nm}^{-1}$ is of significance⁶. If one assumes Eq. (3.26) to be appropriate up to $|\vec{\alpha}| = |\Delta\vec{k}| < \frac{|\vec{k}_{\text{max}}|}{100}$, the spatial resolution of the 1D Wigner function $\sum_{q_x=-|\vec{k}_{\text{max}}|}^{|\vec{k}_{\text{max}}|} e^{iq_x x} \rho_{Q-\frac{q_x}{2}, Q+\frac{q_x}{2}}$ becomes [78]

$$\Delta l_x = \frac{\pi}{\Delta\vec{k}}, \quad (3.28)$$

and so here $\Delta l_x > 210\text{nm}$. This would mean that the densities entering Eq. (3.27) are averaged in an area of about $210 \times 210\text{nm}^2$ around the QD with the state D .

One could debate whether $|\Delta\vec{k}| > \frac{|\vec{k}_{\text{max}}|}{100}$ is a too strong or too weak assumption to perform the approximation Eq. (3.26). However, the important point for this thesis is, that the spatial resolution is of the order of the homogeneous density region in a device, cf. Sec. 2.1.3. So in principle a spatially resolved theory is not necessary in this thesis. On the other hand, it displays restriction for a spatio-temporal description of devices, namely the spatial resolution. To achieve better spatial resolution, therefore, one might need to look for greater approximations than (3.26) to achieve a better spatial resolution.

3.4. Numerical Integration

Equation (3.11) shows a triple sum over all states. These states could either belong to discrete QD states, or to quasi-continuous reservoir states. In the latter case, the related sum can be transformed into an integral via the formula [39]

$$\sum_{\vec{k}} \rightarrow \left(\frac{L_d}{2\pi}\right)^d \int d^d k, \quad (3.29)$$

where d denotes the subsystem dimensionality, and L_d an extension in the respective dimensions. For some processes, such as the capture processes depicted in Fig. 2.4, this leads to the necessity of evaluating high-dimensional integrals, especially in a QD-3DCR

⁶ For pure e-e processes, for mixed e-h processes, it is about $|\vec{k}_{\text{max}}| = 3.5\text{nm}^{-1}$

sample⁷:

$$\begin{aligned}
 S_{\text{in,cap}}^e &= \frac{2\pi}{\hbar} \sum_{\vec{k}_a, \vec{k}_b, \vec{k}_c} W_D(\vec{k}_a, \vec{k}_b, \vec{k}_c) \left(2W_D^*(\vec{k}_a, \vec{k}_b, \vec{k}_c) - W_D^*(\vec{k}_a, \vec{k}_c, \vec{k}_b) \right) \\
 &\quad \times f_{\vec{k}_b} f_{\vec{k}_c} (1 - f_{\vec{k}_a}) \delta(\varepsilon_D + \varepsilon_{\vec{k}_a} - \varepsilon_{\vec{k}_b} - \varepsilon_{\vec{k}_c}) \\
 &= \frac{2\pi}{\hbar} \left(\frac{V}{(2\pi)^3} \right)^3 \int d^3 k_a \int d^3 k_b \int d^3 k_c W_D(\vec{k}_a, \vec{k}_b, \vec{k}_c) \left(2W_D^*(\vec{k}_a, \vec{k}_b, \vec{k}_c) - W_D^*(\vec{k}_a, \vec{k}_c, \vec{k}_b) \right) \\
 &\quad \times f_{\vec{k}_b} f_{\vec{k}_c} (1 - f_{\vec{k}_a}) \delta(\varepsilon_D + \varepsilon_{\vec{k}_a} - \varepsilon_{\vec{k}_b} - \varepsilon_{\vec{k}_c}) \\
 &=: \int d\vec{x} F(\vec{x}), \tag{3.30}
 \end{aligned}$$

Evaluating the δ -distribution Eq. (3.30) can be interpreted as an 8-dimensional integral. As the evaluation of high dimensional integrals is a challenging task on it's own, this section is devoted to numerical integration methods. First the ‘‘standard methods’’ are presented in Sec. 3.4.1. The sections that follow give a short introduction into Monte-Carlo and Quasi-Monte-Carlo integration (cf. 3.4.2 and 3.4.2). The results of the latter two sections are taken from [31], which is also recommended for a detailed description of Quasi-Monte Carlo methods.

In this section, without loss of generality (WLOG), a d -dimensional unit cube $\mathcal{I}^d = [0, 1]^d$ is assumed as integration volume. An extension to arbitrary finite domains can be easily done via appropriate substitutions, and/or splittings of the integrals. Furthermore only integrable functions f , not to be mixed up with the Fermi-distribution, are considered.

3.4.1. Grid based methods

The most intuitive approach to numerical integration is to perform a Riemann sum numerically: One divides the integration domain into N_h equal segments with distance

$$s_m - s_{m-1} = h = 1/N_h. \tag{3.31}$$

One then can approximate the integral value via step functions at the node point t_m (cf. 3.1):

$$RI_1(f) := h \sum_{i=0}^{N_h-1} f(t_i), \text{ with } t_i \in [s_{m+1}, s_m], t_m - t_{m-1} = h, \tag{3.32}$$

Obviously the error of that approximation decreases for decreasing interval length h , or increasing number of node points N_h . Via a Taylor expansion one can proof that for continuous functions and $t_m = s_m$ (cf. [79])

$$I_1(f) := \int_0^1 f(x) dx = RI_1(f) + \mathcal{O}(N_h^{-1}). \tag{3.33}$$

⁷In Eq. (3.30) the spin sum has already been performed.

3. Equations of motion

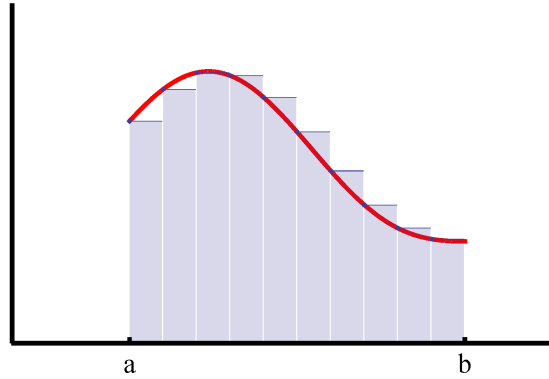


Figure 3.1.: Illustration of a numerical integration via a Riemann sum

The extension to the multi-dimensional case, is done by applying the one dimensional integration rules to each dimension [31]:

$$I_d(f) := \int_{\mathcal{I}^d} f(\vec{x}) d^d x = \int_0^1 dx_1 \dots \int_0^1 dx_d f(x_1, \dots, x_d). \quad (3.34)$$

One divides the integration domain of the respective coordinates x_i , $i = 1, \dots, d$ into N_i equal intervals. This leads to a partition of the d -dimensional integration domain into $N = N_1 \cdot \dots \cdot N_d$ volume segments, or a d -dimensional grid with N node points. For simplicity, it will be assumed in the following that $N_i = N_j$ for arbitrary $i, j \in [1, \dots, d]$, so that $N = N_i^d$. The error approximation Eq. (3.33) then holds for each dimension, and the total error of the d -dimension Riemann sum RI_d is on the order of⁸

$$|I_d(f) - RI_d(f)| = \mathcal{O}(N^{-1/d}). \quad (3.35)$$

So the numerical demand of calculating the multi-dimensional integral increases exponentially with the dimensionality. This is the "curse of dimensionality" [31].

Of course there are various possibilities to increase the accuracy. The most convenient one, for example is to improve the approximation of the integrand f within the intervals Eq. (3.31): Instead of using step-functions, one could fit polynomials of the order n , cf. [79]. Those methods are denoted as "Newton-Cotes rules". Typically used orders of the fit polynomials are $n = 0$ (*rectangular rule*, which is equivalent to the Riemann sum), $n = 1$ (*trapezoidal rule*), and $n = 2$ (*Simpson's rule*). Due to symmetry arguments, the latter is exact even up to third-order polynomials, leading to an error for a d -dimensional integral on the order of

$$\mathcal{O}(N^{-4/d}). \quad (3.36)$$

However, the latter approximation holds only if $\frac{\partial^4 f}{\partial^4 x_i}$ is continuous on I^d . This demonstrates a further disadvantage of these methods: In general, for a higher accuracy, a

⁸If the partial derivatives $\frac{\partial f}{\partial x_i}$ are continuous.

higher degree of regularity of the integrated function is needed.

There are a large variety of methods using the common idea to approximate the integrand f , by a fit function g_f , that can be integrated analytically. The integral value can then be evaluated via the function values of f at specific, not necessarily equidistant, node points x_i , where $f(x_i) = g_f(x_i)$. These *Gauss quadrature formulas* have the common ansatz

$$\int_0^1 f(x)dx \approx \sum_{i=0}^{N_j} w_i f(x_i), \quad (3.37)$$

with the weighting factors w_i . However, all of these methods underly the curse of dimensionality.⁹ Furthermore, increased accuracy is generally connected with the need for a higher degree of regularity of the integrand.

3.4.2. Monte Carlo estimates

Monte Carlo

Monte Carlo integration uses a different ansatz than the grid based methods to approximate an integral value, namely a stochastic approach: By interpreting the function f to be integrated as a random variable, the value of the integral $\int_{\mathcal{I}^d} f(\vec{x}) d^d x$ equates the expectation value of f (cf. [31]):

$$\mathbb{E}f = \int_{\mathcal{I}^d} f d\lambda_d. \quad (3.38)$$

The expectation value can be approximated by the mean value

$$\mathbb{E}f \approx \frac{1}{N} \sum_{i=1}^N f(\vec{x}_i), \quad (3.39)$$

where the \vec{x}_i are independently distributed random vectors in \mathcal{I}^d . One can show that the error of that approximation is, “*on the average*”, proportional to $\frac{1}{\sqrt{N}}$, **independent of the dimensionality of \vec{x}** (cf. [31]). A further advantage of Monte Carlo integration is the relatively small degree of regularity needed for the error estimate: It holds for all $f \in \mathcal{L}^2$, in contrast to, for example, Simpson’s rule, where $f \in \mathcal{C}^4(\mathcal{I}^d)$ was needed.

However, MC integration also has several disadvantages. For example, one achieves only a probabilistic error estimation: Since the node points in Eq. (3.39) are random vectors, there is no guarantee, that increasing the number nodes improves the approximation Eq. (3.39). As a result, Monte Carlo simulations should be performed several times with different random numbers. That, in turn, increases the calculation time. Furthermore, for the problem considered in this thesis, Simpson’s rule also offers an error estimation of the order $\mathcal{O}(\frac{1}{\sqrt{N}})$ in $d = 8$. So for the problem under consideration, there is no advantage of Monte Carlo integration compared to Simpson’s rule, except a reduced need for regularity of the function. However this has to be paid by the probabilistic error bounds [31].

⁹Although there are methods to reduce the dimensions dependency of the convergence.

3. Equations of motion

Quasi-Monte Carlo

According to [31], there are point sequences $X = (\vec{x}_1, \dots, \vec{x}_N)$ that lead to a better approximation of the expectation value Eq. (3.39), and others that lead to a worse one. So the question behind quasi-Monte Carlo (QMC) is what are “better point sets” and is it possible to construct them? That first question can be answered by the

Koksma–Hlawka inequality [31]:

$$\left| \int_{\mathcal{I}^d} f d\lambda_d - \frac{1}{N} \sum_{j=1}^N f(x_j) \right| \leq D_n^*(x_1, \dots, x_N) V(f), \quad (3.40)$$

where $V(f)$ denotes the variation of f in the sense of Hardy and Krause[31] and

$$D_n^*(x_1, \dots, x_N) = \sup_{0 < x < 1^d} \left| \frac{\#\{j, x_j \in [0, x)\}}{N} - \lambda_d([0, x)) \right| \quad (3.41)$$

is what is called the $*$ -discrepancy. The message of the *Koksma–Hlawka inequality* (3.40) is: For $V(f) < \infty$ (bounded variation), the error of the integral approximation is ruled by the $*$ -discrepancy [80]. The goal of this finding is, that **the $*$ -discrepancy is independent of the integrand f** . It depends solely upon the chosen point set.

The $*$ -discrepancy is a measure for how uniform the points are distributed. An illustration of the meaning of the $*$ -discrepancy can be seen in Fig. 3.2:

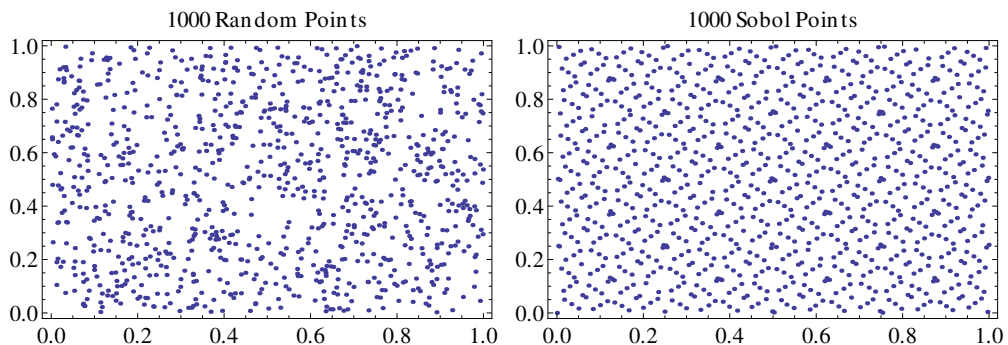


Figure 3.2.: (*left*): 1000 random points in 2D, generated via code of Matsumoto et al. [81], (*right*): 1000 Sobol points in 2D generated via code of Kuo et al. [32, 82].

The random numbers depicted in Fig. 3.2(*left*) are relatively non-uniformly distributed. There are regions with point clusters and relatively large regions without points. The value of the $*$ -discrepancy becomes large. In contrast the Sobol points Fig. 3.2(*right*) are uniformly distributed. The value of the $*$ -discrepancy becomes small.

There are several approaches to constructing point sets with a low $*$ -discrepancy,

so called low-discrepancy point sets (LDPs). This answers the second question. The error estimate of LDP's is better than that of MC integration. The best approaches provide a $*$ -discrepancy for N points in \mathcal{I}^d in the order $\log^{d-1}(N)/N$ as $N \rightarrow \infty$. By contrast, independent and identically distributed random points, as used in classical MC integration, have a $*$ -discrepancy of the order $\sqrt{\log(N)/N}$ [80]. The price one has to pay by using QMC, is that the error becomes dimensionality-dependent again and the integrands have to be of bounded variation. However, the dimension dependency is notably smaller and the constraints for the approximations are significantly diminished compared to Gauss quadrature formulas. QMC techniques provide deterministic results since such LDPs are constructed.

In this thesis code provided by S. Joe and F. Kuo [32, 82] is used to generate the QMC point set. It is based on the calculation of Sobol sequences [31].

3.4.3. Summary

The previous discussion of numerical integration methods can be roughly summarized as in the following table:

Table 3.1.: Comparison of different integration techniques, showing how many nodes are needed to achieve an error estimation of $\mathcal{O}(\frac{1}{N_{\text{goal}}})$

Integration method	required regularity	# of nodes to achieve $\mathcal{O}(1/N_{\text{goal}})$
Simpson's Rule	$\mathcal{C}^4(\mathcal{I}^d)$	$N_{\text{goal}}^{d/4}$
Monte Carlo	$\mathcal{L}^2(\mathcal{I}^d)$	N_{goal}^2
Quasi-Monte Carlo	$\mathcal{L}^2(\mathcal{I}^d), V(f) < \infty$	$\approx^{10} N_{\text{goal}} \log^{d-1}(N_{\text{goal}})$

¹⁰The exact number of grid points is for $d > 1$: $\left(-\frac{(d-1)N_{\text{goal}}^{1/(d-1)}}{\ln(10)} W \left(-\frac{\ln(10)}{[(d-1)N_{\text{goal}}^{1/(d-1)}]} \right) \right)^{d-1}$, where W is the Lambert W-Function, cf. [83].

4. Comparison of 2D and 3D scattering

In this chapter, microscopic Coulomb scattering rates will be calculated for QD-2D and QD-3D samples, cf. Eq. (3.12). A comparison of the results should clarify how reservoir dimensionality influences Coulomb scattering. The statements in this thesis refer to a comparison of a 2D carrier reservoir and a 3D carrier reservoir. Quantum wires (1D) are not considered.

This chapter is structured as follows:

Before the scattering rates are presented in Sec. 4.3, the model under consideration must be further explained.

In Sec. 4.1, the relevant scattering processes will be specified. Section 4.2 discusses the question of how to relate scattering rates that depend on different carrier densities to one another: The area density in the 2D reservoir on the one hand, and the volume density of the 3D reservoir on the other. Finally, in Sec. 4.4 conclusions and in Sec. 4.5 an outlook will be presented.

4.1. Relevant scattering processes

A detailed discussion of possible scattering processes and their efficiency in structures similar to the 2D-QD sample under consideration here can be found in [20] and will not be repeated here.

If one compares the scattering processes in a QD-2D system with the related processes in a QD-3D system, it is intuitive to assume that significant differences in the respective rates stem from processes containing subsystem transitions (transitions between QD and reservoir states)¹. Therefore, the total scattering rate S_{in}^D will be decomposed into the processes similar to those classified in Ref. [62]. Here, they are ordered by the number of occurring subsystem transitions (SSTs),

$$S_{\text{in}}^D = \underbrace{S_{D,\text{rel},1}^{\text{in}}}_{0 \text{ SST}} + \underbrace{S_{D,\text{cap}}^{\text{in}} + S_{D,3\text{QD}}^{\text{in}}}_{1 \text{ SST}} + \underbrace{S_{D,\text{rel},2}^{\text{in}}}_{2 \text{ SSTs}} - \underbrace{S_{D,\text{exch.}}^{\text{in}}}_{\text{not classified}}. \quad (4.1)$$

The various processes will be defined below. As a system in quasi-equilibrium is considered, the related out-scattering rates can be determined via the principle of *detailed balance*, cf. Ref. [64]. The out-scattering rate is then given by

$$S_{\text{out}}^D = S_{\text{in}}^D \frac{1 - f_D}{f_D}, \quad (4.2)$$

¹The QD wavefunctions are equal for both reservoir types, and the character of delocalized carrier states is also similar for 2D and 3D reservoirs. As a result, the Coulomb overlap integrals should be relatively similar for both reservoir types in those types of carrier transitions.

4. Comparison of 2D and 3D scattering

where $f_D = 1/(1 + \exp[(E_D - \mu_{2D/3D})/(k_B T)])$ is the quasi-equilibrium occupation of the QD state D . The most important scattering processes into the QD ground state (GS) are illustrated in Fig. 4.1. The processes are defined as follows:

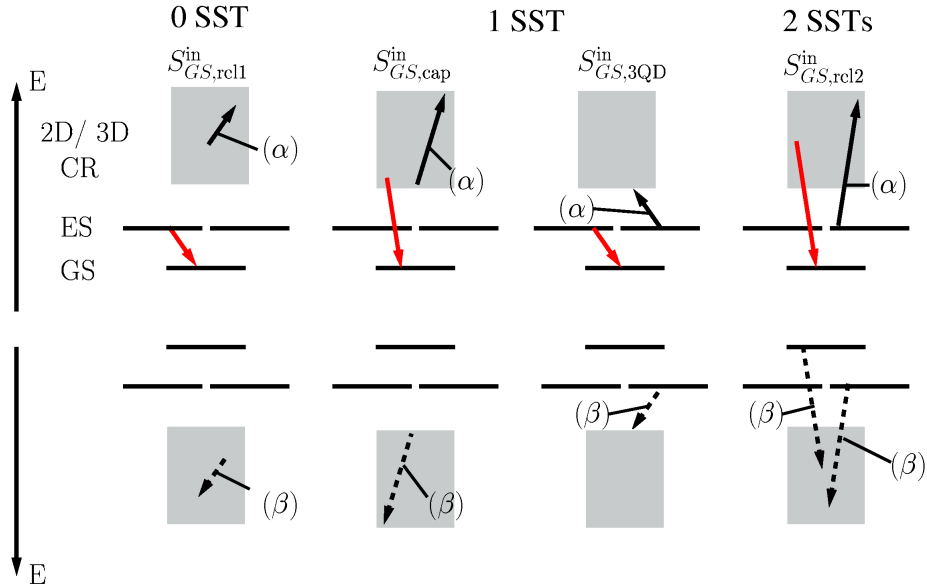


Figure 4.1.: Illustration of the main scattering processes in order of the number of subsystem transitions (SST). Pure electron processes are denoted with (α) ; mixed processes with (β) . The processes are shown in the electron-hole picture, the formulas (3.11)–(4.5) are in a valence band / conduction band picture. Not depicted: mixed relaxation process containing the hole ground state in $S_{D,3QD}^{in}$ and the corresponding processes involving the second excited for the rates $S_{D,rel,2}^{in}$, $S_{D,rel,2}^{in}$ and $S_{D,3QD}^{in}$.

- Without subsystem transition, relaxation process 1:

$$S_{D,rel,1}^{in} = \frac{2\pi}{\hbar} \sum_{k_a, k_b, D_2} |W_{D k_a k_b D_2}|^2 f_{k_b} f_{D_2} (1 - f_{k_a}) \delta(\varepsilon_D + \varepsilon_{k_a} - \varepsilon_{k_b} - \varepsilon_{D_2}), \quad (4.3)$$

Here, a carrier from the QD excited state (ES) relaxes into the ground state (GS) and a reservoir carrier is scattered to a state with higher momentum.

- With one subsystem transition:

1. The capture process

$$S_{D,cap}^{in} = \frac{2\pi}{\hbar} \sum_{k_a, k_b, k_c} W_{D k_a k_b k_c} (W_{D k_a k_b k_c}^* - W_{D k_a k_c k_b}^*) \times f_{k_b} f_{k_c} (1 - f_{k_a}) \delta(\varepsilon_D + \varepsilon_{k_a} - \varepsilon_{k_b} - \varepsilon_{k_c}). \quad (4.4)$$

Here, three reservoir states participate, cf. Fig. 4.1. The capture process

describes the filling of the QD states by means of a redistribution of carriers in the reservoir. It includes both, direct and exchange interaction. According to Ref. [62], this process determines primarily the long-time dynamics of the QD states.

2. The three QD states relaxation process

$$\begin{aligned}
 S_{D,3\text{QD}}^{\text{in}} &= \frac{2\pi}{\hbar} \sum_{k_a, D_2, D_3} W_{D k_a D_2 D_3} (W_{D k_a D_2 D_3}^* - W_{D k_a D_3 D_2}^*) \\
 &\quad \times f_{D_2} f_{D_3} (1 - f_{k_a}) \delta(\varepsilon_D + \varepsilon_{k_a} - \varepsilon_{D_2} - \varepsilon_{D_3}) \\
 &\quad + \frac{2\pi}{\hbar} \sum_{k_a, k_b, D_2} |W_{D D_2 k_a D_3}|^2 f_{k_a} f_{D_3} (1 - f_{D_2}) \delta(\varepsilon_D + \varepsilon_{D_2} - \varepsilon_{k_a} - \varepsilon_{D_3}),
 \end{aligned} \tag{4.5}$$

where a carrier from a QD excited state relaxes into the ground state and a third QD carrier enters the reservoir, see Fig. 4.1.

- With two subsystem transitions, relaxation process 2:

$$S_{D,\text{rel},2}^{\text{in}} = \frac{2\pi}{\hbar} \sum_{k_a, k_b, D_2} |W_{D k_a D_2 k_b}|^2 f_{k_b} f_{D_2} (1 - f_{k_a}) \delta(\varepsilon_D + \varepsilon_{k_a} - \varepsilon_{k_b} - \varepsilon_{D_2}) \tag{4.6}$$

$$+ \frac{2\pi}{\hbar} \sum_{k_a, k_b, D_2} |W_{D D_2 k_a k_b}|^2 f_{k_a} f_{k_b} (1 - f_{D_2}) \delta(\varepsilon_D + \varepsilon_{D_2} - \varepsilon_{k_a} - \varepsilon_{k_b}), \tag{4.7}$$

This process describes the in-scattering of a reservoir carrier into the QD-GS by means of the out-scattering of a QD-ES carrier into the reservoir. The second term in Eq. (4.7) as well as in Eq. (4.5) for $D = \text{GS}$, describes the related mixed electron-hole processes, cf. Fig. 4.1 (β). These terms are non-zero only for carriers in different bands. In Eqs. (4.4) and (4.3), these processes are hidden in the sums over all multi-indices, which still contain sums over spin, carrier bands, and other quantum numbers describing the state, cf. Sec. 2.2 .

The related exchange term of $S_{D,\text{rel},2}^{\text{in}}$ and $S_{D,\text{rel},2}^{\text{in}}$ has the form

$$\begin{aligned}
 S_{D,\text{exch.}}^{\text{in}} &= \frac{2\pi}{\hbar} \sum_{k_a, k_b, D_2} \text{Re} \left[W_{D k_a D_2 k_b} W_{D k_a k_b D_2}^* + W_{D k_a k_b D_2} W_{D k_a D_2 k_b}^* \right] \\
 &\quad \times f_{D_2} f_{k_b} (1 - f_{k_a}) \delta(\varepsilon_D + \varepsilon_{k_a} - \varepsilon_{D_2} - \varepsilon_{k_b}).
 \end{aligned} \tag{4.8}$$

It is a mixture of these two processes. Therefore, it cannot be classified by the number of subsystem transitions.

Note that the sums in the scattering rates $S_{D,\text{rel},2}^{\text{in}}$, $S_{D,\text{rel},2}^{\text{in}}$, $S_{D,\text{exch.}}^{\text{in}}$, and $S_{D,3\text{QD}}^{\text{in}}$ include both excited states. For clarity, only one of the two excited state transitions will be depicted in the illustrations of these processes, although both processes will be included in the scattering rates.

4.2. How to compare 2D and 3D carrier densities?

The scattering rates are calculated as functions of the respective carrier densities since that is essential for rate equation models [84, 34, 85, 62, 86]. So the question arises of how to relate the area carrier density n_{2D} [cm^{-2}] in the 2D reservoir, to the 3D (volume) density n_{3D} [cm^{-3}]. Unless otherwise noted, the ratio [87, 88]:

$$n_{3D} = \frac{n_{2D}}{L}, \quad (4.9)$$

will be used to relate the two densities to each other. The idea behind that relation is that the 3D volume carrier density is compared with the carrier density in the effective volume of the 2D reservoir cf. Fig 4.2. It is emphasized that the effective width L of

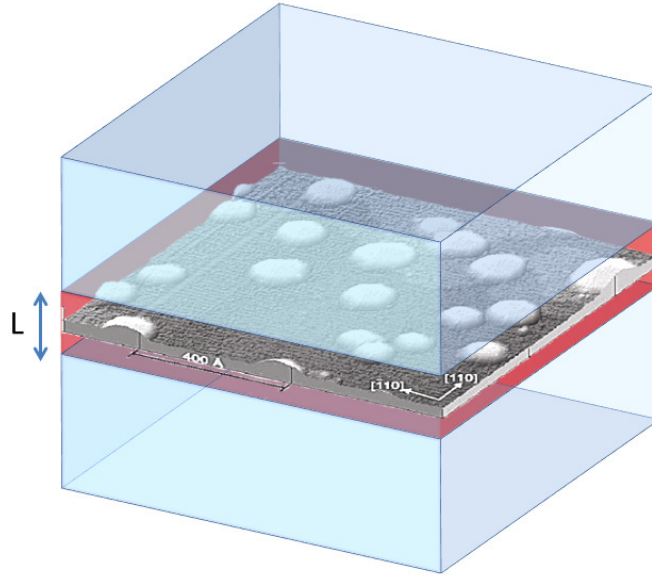


Figure 4.2.: Illustration of a QD device with an effective height L of the mesoscopic structures. A scanning tunneling microscope picture of Ref. [1] has been used.

the 2D reservoir (and the QD) is not a fit parameter, but can be calculated if all QD parameters are known, cf. Ref. [47]. Here the confinement potential of the mesoscopic structures is unknown, so L has been chosen arbitrarily.

For the parameters under consideration, Eq. 4.9 causes very similar occupation probabilities for the electrons, whereas there is a more pronounced difference in the hole distributions, cf. Fig. 4.3. Hence, for a comparison on a fair basis, this thesis focuses on scattering processes into electron states.

Although Eq. (4.9) is an intuitive and also established way to relate the scattering rates, it is not the only possibility. To clarify whether the results are dependent on the specifics of Eq. (4.9), a second way of relating 2D and 3D scattering rates will be investigated. The rates will be considered as functions of the chemical potential μ , which is then assumed to be equal for the 2D and 3D reservoir, cf. Sec. 4.3.8.

4.2. How to compare 2D and 3D carrier densities?

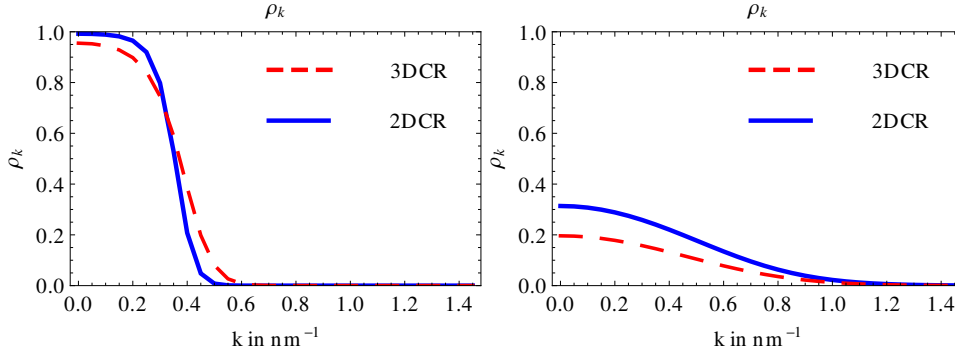


Figure 4.3.: Fermi distribution for electrons (left) and holes (right) for the respective reservoirs @ $20 \times 10^{11} \text{cm}^{-2}$ and $20 \times 10^{17} \text{cm}^{-3}$. This fits a comparison of two samples with $L = 10 \text{nm}$.

Charge neutrality conditions

In this thesis the condition

$$n_{2D/3D} = n_{2D/3D}^e = n_{2D/3D}^h \quad (4.10)$$

is assumed. This corresponds to charge neutrality in the respective reservoirs, but not in the entire active region. Instead, one could assume equal carrier densities in the active region [20, 21], so that

$$N_{\text{sys}}^{2D} := n_{2D}^e + \frac{2N_{\text{QD}}}{A} \sum_i f_{\text{QD},i}^e = n_{2D}^h + \frac{2N_{\text{QD}}}{A} \sum_i f_{\text{QD},i}^h, \quad (4.11)$$

or

$$N_{\text{sys}}^{3D} := n_{3D}^e + \frac{2N_{2D}N_{\text{QD}}}{AL_z} \sum_i f_{\text{QD},i}^e = n_{3D}^h + \frac{2N_{2D}N_{\text{QD}}}{L_z} \sum_i f_{\text{QD},i}^h, \quad (4.12)$$

where N_{QD} is the number of QDs per layer, N_{2D} the number of layers and AL_z the 3D representation volume, cf. Tab. F.2 and Tab. F.3. The question then arises what to compare:

(i) Assuming $N_{\text{sys}}^{2D}/L = N_{\text{sys}}^{3D}$ would cause strongly different reservoir carrier densities in the low² carrier regime. The reason is the larger representative volume of the 3D reservoir as compared to the 2D one. As a result, $\frac{2N_{2D}N_{\text{QD}}}{AL_z} \sum_i f_{\text{QD},i}^{\lambda=e,h} < \frac{2N_{\text{QD}}}{AL} \sum_i f_{\text{QD},i}^{\lambda=e,h}$.

(ii) If one assumes Eq. (4.9) under the conditions Eqs. (4.11) and (4.12), the result would be different ratios between electron and hole densities in the two samples, cf. Fig. 4.3. This is not desirable for a comparison either.

However, in the high-density regime, the impact of the QD carriers on the total charge

²In principal, the lowest densities under consideration are still much higher than the intrinsic carrier concentration at 300 K, which is about $2.1 \times 10^6 \text{cm}^{-3}$ for GaAs and $1.3 \times 10^{15} \text{cm}^{-3}$ for InAs cf. Ref. [47]. Therefore “low” refers to the density range under investigation.

4. Comparison of 2D and 3D scattering

density becomes negligible and so the approximation Eq. (4.10) becomes appropriate. Furthermore, Hartree-Fock energy renormalizations are not included in the calculations, so that unwanted effects caused by space charges do not appear.

In this thesis, the conditions Eq. (4.9) and Eq. (4.10) are assumed. The plots in this chapter are scaled in such a way, that points on the x-axis fulfill these conditions.

4.3. Numerical results

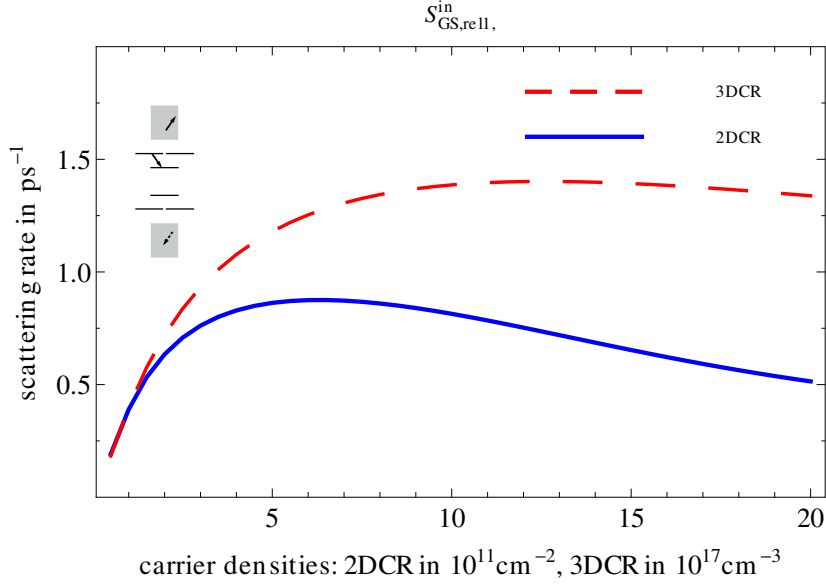
In brief, one can summarize the detailed results as follows: The calculated scattering rates show a nonlinear dependency on the carrier densities [20]. **In agreement with the experimental findings of Ref. [4], the scattering rates of the 2D and 3D samples show very similar qualitative and quantitative behavior for the main scattering processes.** This holds for most of the various scattering processes, as well as a wide parameter range, cf. Sec. 4.3.8. Nevertheless, beyond global behavior, specific differences were observable. This concerns the dependency on the (effective) QD height, or the behavior at high carrier densities.

This section is structured as follows: Initially, the different scattering processes will be discussed, in order of the number of subsystem transitions. Firstly $S_{D,\text{rel},1}^{\text{in}}$ (Sec. 4.4), followed by $S_{D,\text{cap}}^{\text{in}}$ and $S_{D,3\text{QD}}^{\text{in}}$ (Sec. 4.3.2). Then $S_{D,\text{rel},2}^{\text{in}}$ will be discussed (Sec. 4.3.3). Following that, a comparison of the pure electron contributions to $S_{D,\text{rel},1}^{\text{in}}$ and $S_{D,\text{rel},2}^{\text{in}}$ will be done (Sec. 4.3.4). Section 4.3.6 summarizes the intermediary results. This is followed by a comparison with the experimental findings (Sec. 4.3.7). Finally, the robustness of the results with regard to parameter variations will be investigated (Sec. 4.3.8).

4.3.1. Scattering rates without transitions between QD and reservoir:

$$S_{GS,\text{rel},1}^{\text{in}}$$

In Fig. 4.4 one sees, that the 2D and 3D scattering rates $S_{GS,\text{rel},1}^{\text{in}}$ exhibit similar characteristics. As described in Ref. [63], the scattering rates obey two different regimes. First, they increase with increasing carrier density, due to the increasing number of scattering partners. Eventually, for higher carrier densities, they start to decrease, due to Pauli blocking. In the following we will denote the regime where Pauli blocking becomes visible via a reduction of the slope of the scattering rates, as *blocking regime*. Here $S_{GS,\text{rel},1}^{\text{in}}$ the 2D rate starts to decrease for densities above $6 \times 10^{11} \text{ cm}^{-2}$ or above $12 \times 10^{17} \text{ cm}^{-3}$ for the 3D sample, cf. Fig. 4.4. The two rates are almost equal in the first regime (up to ca. $2 \times 10^{11} \text{ cm}^{-2}$, or $2 \times 10^{17} \text{ cm}^{-3}$). The close similarity of these two rates up to blocking regime could be expected, since the absence of subsystem transitions, causes very similar Coulomb-matrix elements. However, the 2D-rate reaches the blocking regime earlier. In consequence, one can observe a 3D rate that is up to about three times higher for high carrier densities.

Figure 4.4.: Carrier relaxation rate $S_{GS,rel,1}^{in}$.

4.3.2. Processes with one transition between QD and reservoir

$S_{D,cap}^{in}$ - Capture processes

Figure 4.5 depicts the capture rates into ground (Fig. 4.5(a)) and excited states (Fig. 4.5(b)), see insets of the figures. For both capture processes, the respective 2D- and 3D rates exhibit similar qualitative characteristics and are of the same magnitude.

For both processes plotted in Fig. 4.5, the 2D rate is slightly more efficient for lower carrier densities. However, for higher densities, the 3D rate exceeds the 2D one. It is difficult to ascertain a precise reason for this behavior, due to the interaction of many effects. Nevertheless, for large densities, screening effects averages over details of Coulomb potential and the increasing density of states (DOS) in the 3DCR are of dominant importance.

The latter argument is also in agreement with the fact that the capture rate into the QD-ES reaches the blocking regime earlier for the 2D-rate, than for the 3D rate, cf. Fig. 4.5 (b). However, this behavior is heavily dependent on system parameters, especially the (effective) height L of the 2DCR, cf. Sec. 4.3.8.

Processes involving three QD states: $S_{GS,3QD}^{in}$

Similarly to the previous findings, the 2D and 3D rates $S_{GS,3QD}^{in}$, plotted in Fig. 4.6 resemble each other qualitatively and quantitatively. However, the 3D rate is here about two times higher than the 2D one. The 2D rate exceeds its maximum at about $n_{2D} = 8 \times 10^{11} \text{ cm}^{-2}$ (which refers to a volume density of $n_{2D}/L = 8 \times 10^{17} \text{ cm}^{-3}$) whereas the 3D rate increases up to about $n_{3D} = 14 \times 10^{17} \text{ cm}^{-3}$. Beyond their maxima, the rates decrease due to Pauli blocking. The position of the maximum is heavily parameter-dependent, cf. Sec. 4.3.8. However, comparing Fig. 4.5 and Fig. 4.6

4. Comparison of 2D and 3D scattering

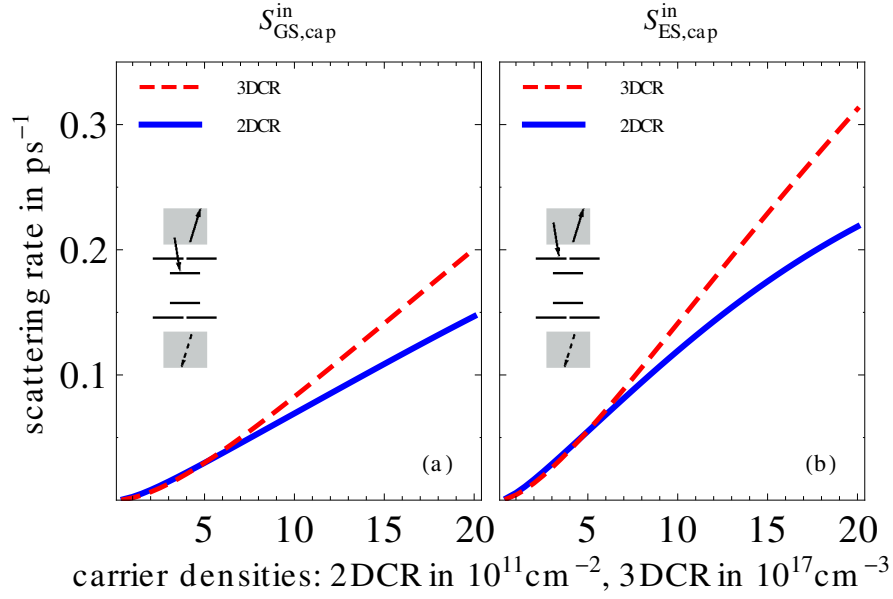


Figure 4.5.: Capture rates: $S_{D,\text{cap}}^{\text{in}}$ into the QD electron ground state $D = GS$ (a), and into an excited state $D = ES$ (b)

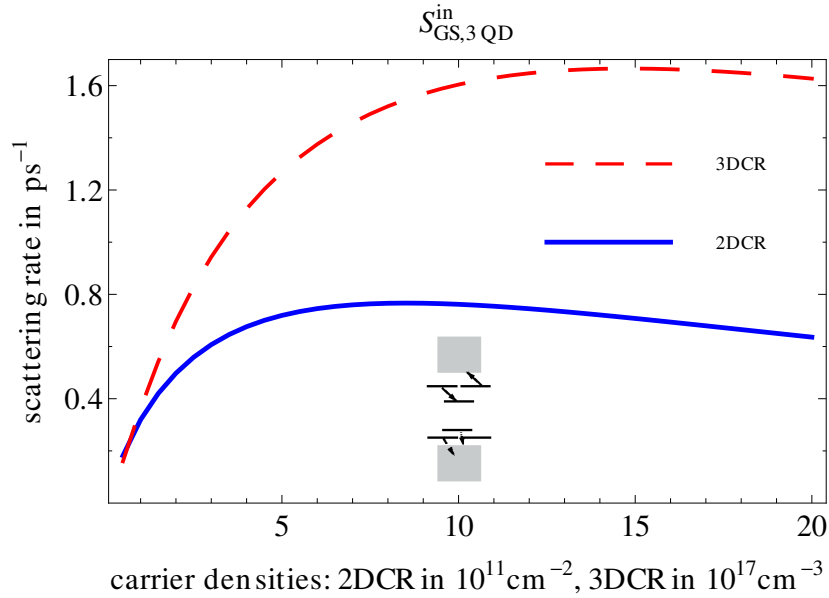


Figure 4.6.: Carrier relaxation rate $S_{GS,3QD}^{\text{in}}$

reveals a more pronounced difference between the rates in Fig. 4.6. This is in so far counterintuitive, since, for the energy spacings used here, the pure electron contribution to $S_{GS,3QD}^{\text{in}}$ is exactly zero for the 3D-QD sample. Nevertheless, its contribution to the related 2D process is also nearly negligible within the parameters used. The reason for

the higher 3D rate can be found in the, in k-space, fastly decreasing in-plane Coulomb integrals (see Ref. [46] and Appx. B) on the one hand side and the additional degree of freedom due to the k_z -component in the 3D reservoir, on the other. In Sec. 4.3.5, this aspect will be discussed in more detail.

4.3.3. Scattering rates with two transitions between QD and reservoir:

$$S_{GS,rel,2}^{in}$$

The 2D and 3D rates $S_{GS,rel,2}^{in}$ show comparable behavior. However, Fig. 4.7 reveals that the rates differ significantly even for low carrier densities. This is different compared to the scattering processes. Nevertheless, the rates are still of the same order of magnitude,

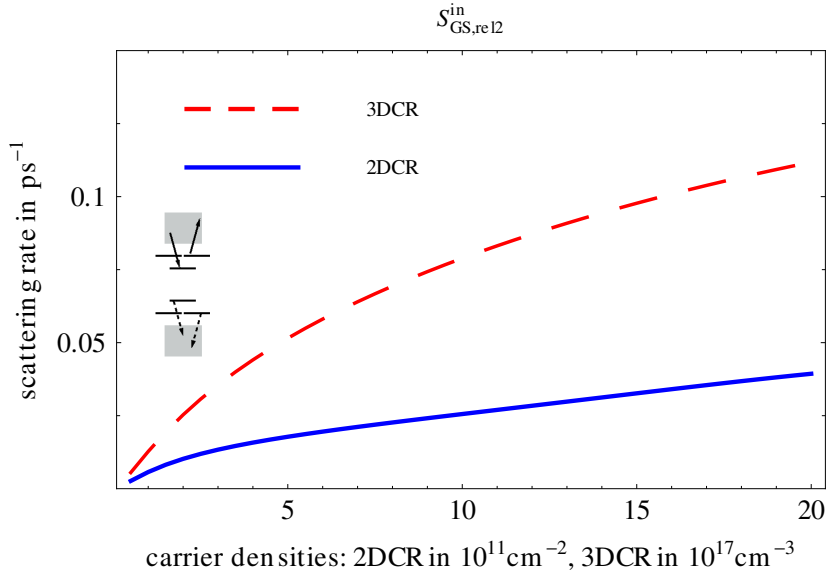


Figure 4.7.: Carrier relaxation rate $S_{D,rel,2}^{in}$.

although here the rate of the 3D sample is about three times higher than the 2D one. This is remarkable in that it is counterintuitive: One would expect that the subsystem transitions between the 2D carrier reservoir and the QD would be more effective, due to the fact the dimensionality is already reduced. This aspect will be discussed in more detail within the following section.

4.3.4. Comparison of the relaxation processes

Comparing the pure electron contribution of Eq. (4.3) and Eq. (4.6), one can see that both equations obey a very similar structure. They could be written as

$$S_{D,rel,1}^{in,e} + S_{D,rel,2}^{in,e} = \frac{2\pi}{\hbar} \times \sum_{k_a, k_b, D2 \in CB} \left(|W_{D k_a k_b D2}|^2 + |W_{D k_a D2 k_b}|^2 \right) f_{k_b} f_{D2} (1 - f_{k_a}) \delta(\varepsilon_D + \varepsilon_{k_a} - \varepsilon_{k_b} - \varepsilon_{D2}). \quad (4.13)$$

4. Comparison of 2D and 3D scattering

This shows that these two rates differ “only” in their Coulomb matrix elements. Nevertheless, $S_{D,rel,2}^{in,e}$ contains two subsystem transitions, whereas only one appears in $S_{D,rel,1}^{in,e}$. That favors these two processes for a detailed comparison: The pure electron contribu-

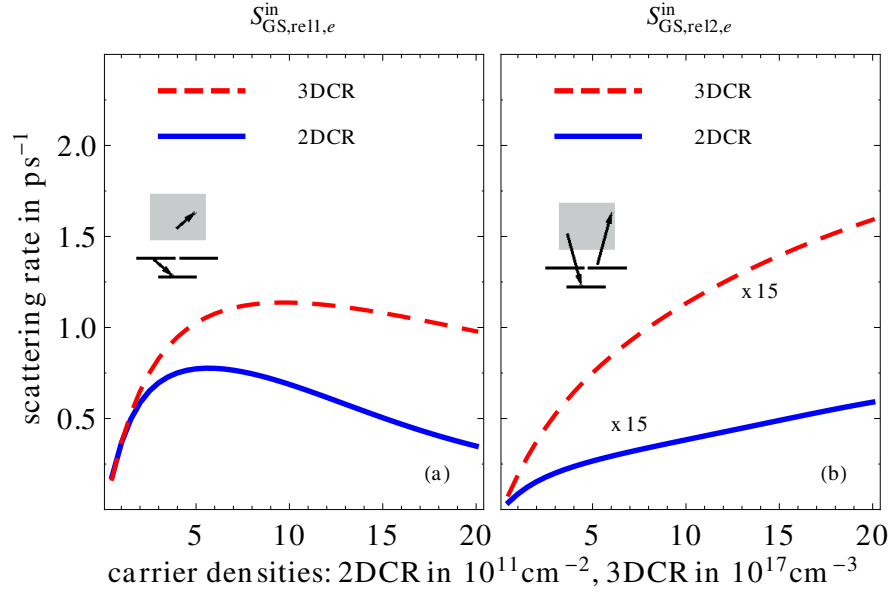


Figure 4.8.: Carrier relaxation rates, pure CB electron contribution of (a) $S_{GS,rel,1}^{in}$, and (b) $S_{GS,rel,2}^{in}$.

tions of the relaxation rates $S_{GS,rel,1}^{in}$ and $S_{GS,rel,2}^{in}$ show similar behavior compared to the complete processes, cf. Fig. 4.8. The 3D rate in particular is (mostly) larger than the 2D one. This behavior is even more pronounced for $S_{GS,rel,2}^{in,e}$ Fig. 4.8(b) than for $S_{GS,rel,1}^{in,e}$ Fig. 4.8(a).

The close similarity of the processes depicted suggests that the higher dimensionality step for the carrier transition in the 3D samples does not lead to reduced scattering efficiency in comparison to the 2D one. In other words, on average **scattering from a 3D carrier reservoir to QD states has similar efficiency as scattering from a 2D reservoir to QD**. This is astonishing in so far as one would expect a higher scattering efficiency in the 2D-QD sample, stemming from the high overlap of equal z -wavefunctions in the QD and 2D reservoir. However, this can be misleading since the Coulomb matrix elements are not pure overlap integrals.

Here, 3D-rates are usually even higher than the 2D ones. For $S_{GS,rel,1}^{in}$, the differences of the 2D and 3D scattering rates that appeared were mainly attributed to the earlier onset of Pauli blocking in the 2D sample. Generally, a higher efficiency of the 3D rate can be supported by several aspects:

- The smaller screening wavenumber κ see Fig. 2.7 of the 3D carrier reservoir at high carrier densities.
- The differing effective masses in 2D and 3D region (cf. Fig. 4.15).

- It is well known that, on average, the in-plane part of Coulomb matrix elements strongly decreases as momentum transfer increases cf. [20, 46] and Appx. B. For the energies of the scattered carriers given here, the additional z-direction in the 3D reservoir provides the opportunity for lower momentum transfer in the (x,y)-direction at the expense of higher momentum in the z-direction. However, this additional degree of freedom could increase the scattering efficiency.
- In general scattering rates show a complicated non-linear behavior in most of the parameters entering the scattering rates. For that reason, detailed behavior is strongly parameter-dependent and here they might support 3D scattering. Nevertheless, a comparison of the qualitative behavior and the magnitude of the scattering rates seems appropriate.

For completeness the rates of relaxation exchange terms $S_{GS,\text{exch.}}^{\text{in}}$ are plotted in Fig. 4.9. This process could not be classified within the suggested scheme, since it is a mixture of two processes with a different number of subsystem transitions.

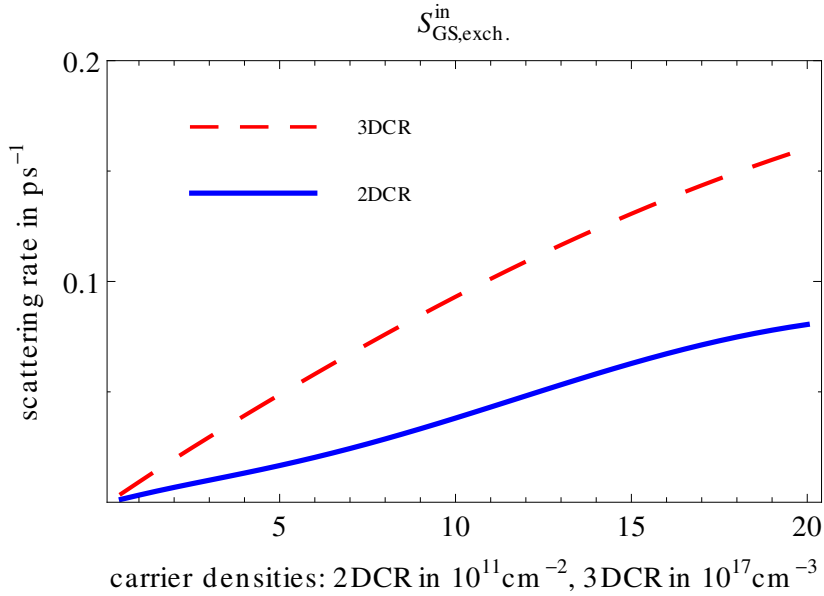


Figure 4.9.: Exchange terms $S_{GS,\text{exch.}}^{\text{in}}$ of the relaxation processes.

The 2D and 3D exchange terms show basically the same behavior and are of the same order of magnitude. However, Fig. 4.9 suggests in some respect more complex behavior of the 2D rate than the 3D one: Within the plotted parameter range, the slope of the 3D curve seems to decrease monotonically with increasing carrier density. By contrast, the 2D curve seems to have an inflection point. This difference reflects the slightly different behavior of the 2D and 3D samples concerning $S_{GS,\text{rel},1}^{\text{in}}$, where the 2D rate has a pronounced maximum and reaches the blocking regimes relatively early, cf. Fig. 4.8(a). However, the slope in Fig. 4.9 stays positive for both samples and therefore the differences are significant.

4.3.5. Do large deviations between 2D and 3D scattering rates appear?

In our previous calculations, a close similarity of scattering rates for the 2D and 3D samples could be observed. However, as noted in the previous sections, extreme differences between the rates could, in principle, appear due to the differing onset of Pauli blocking. Furthermore, the differing density of states (DOS) could also cause strong deviations: If only very energetically low reservoir states are involved in a scattering process, the square root-like 3D DOS is significantly smaller than the constant 2D one. Here, for example, the pure electron contribution to $S_{GS,3QD}^{\text{in}}$ is exactly zero for the 3D sample, whereas for the 2D sample it was “only” relatively small. So the question in the section title could be answered with:

Yes, it could be!

However, the findings in Fig. 4.10 are more interesting than the previous examples. Here the mixed electron-hole contribution of $S_{GS,Rel2}^{\text{in}}$ is plotted (see inset). For this

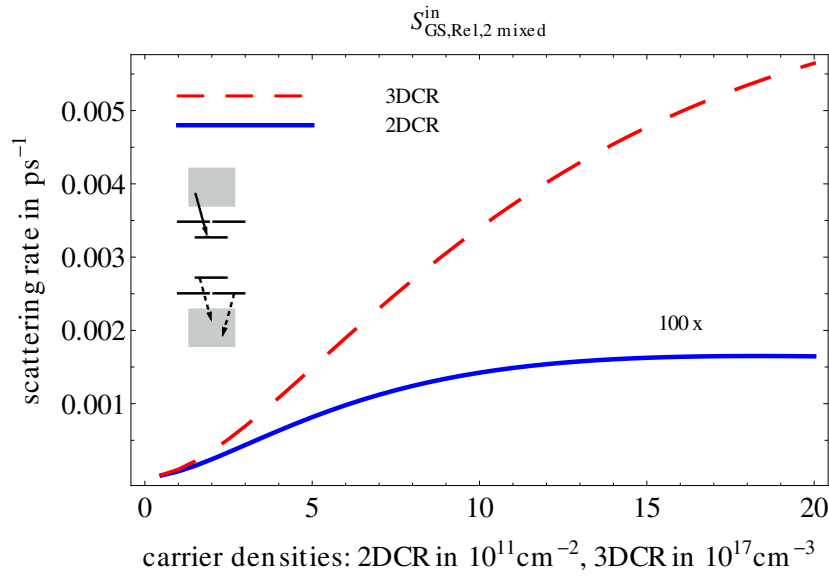


Figure 4.10.: Mixed electron-hole processes of $S_{GS,Rel2}^{\text{in}}$

process, the 3D rate is more than two magnitudes higher than the 2D rate. However, the absolute value of these scattering rates is much smaller than for most of the other processes. Therefore, the impact on system dynamics should be negligible.

The appearance of such different scattering rates is connected with the appearance of some kind of bottleneck in the process: The domain of integration of the reservoir state \vec{k}_a is restricted by the conservation of energy, cf. Eq. (4.7). Particularly, hole states³ with low momentum do not participate in the scattering processes. The smallest participating hole reservoir states have a momentum of $\hbar|\vec{k}_{\text{min}}| = \hbar\sqrt{\frac{2m_h(E_{GS,e}-|E_{GS,h}|)}{\hbar^2}} \approx \hbar 1.1 \text{ nm}^{-1}$. On average, this leads to strongly decreased Coulomb matrix elements, due to their Gaussian-shaped momentum dependency in the in-plane direction, cf. Ref. [46] and Sec. B: Assume a given vector \vec{q} , chosen in such a way, that the overlap integral of the

³Note that the formulas are in the valence-conduction band picture.

reservoir to QD-GS transition has a significant absolute value. Then, for the 2D sample in particular, it has considerable impact on the scattering rate, whether $|\vec{k}_{\min} \pm \vec{q}|$ is inside or outside 2σ of the Gauss curve. Due to the additional z-momentum in the 3D carrier reservoir, the 3D system effectively has an additional degree of freedom to balance the (fixed) energy transfer. Therefore it is less vulnerable to that kind of bottleneck.

This observation can be seen as a further principle difference between the 2D and 3D scattering rates. The 3D rates should be less vulnerable to bottleneck effects due to the additional degree of freedom of the wavevectors.

However, the Markovian treatment strongly supports the appearance of such bottlenecks. If conservation of energy does not need to be fulfilled, efficient scattering channels, to bypass bottlenecks could appear. Hence a non-Markovian treatment [24, 70] of the scattering rates might dissolve such bottlenecks. Furthermore, the assumed QDs with their Gaussian-shaped in-plane wavefunctions, might support such bottlenecks too, due to the rapid decrease of the Coulomb integrals for increasing momentum, cf. Ref. [89].

4.3.6. Summary of intermediary results

The previous findings can be briefly summarized as follows.

- In the main scattering processes, the scattering rates of the 2D and 3D samples show very similar qualitative and quantitative behavior.
- In particular, no significant differences related to the number of subsystem transitions was observed, by comparing the significant rates of a 2D and 3D sample. This indicates that the reduced dimensionality in the 2D sample does not, in average, cause more efficient carrier transitions to the QD states.
- Under certain conditions, for example if there were certain constraints on momentum integration, strong differences between the scattering rates can be observed. Here, the associated scattering processes do not significantly contribute to the scattering rates. Furthermore, these effects might benefit from the Markovian treatment. However, the 3D rates appear to be more robust versus constraints to momentum integration due to an additional degree of freedom (z-momentum).

4.3.7. Comparison with experiments

Several experiments support the idea that the impact of the reservoir dimensionality on carrier scattering is insignificant, for example [30, 4, 90]. Of special note are the works of Sanguinetti⁴ et al. [30, 4], in which the photoluminescence (PL)-rise time τ_r was measured. The PL-rise time is a measure of how fast a PL signal reaches its maximum. It is extracted via an exponential fit onto the time-resolved PL data, cf. Ref. [91].

Before a carrier can recombine radiatively from a certain level, it has to enter that level. Therefore, τ_r is also a measure of the average time carriers need to occupy that energy level (here the QD-GS). According to Siegert et al. [3], this involves, see also Fig. 4.11:

⁴Verma et al. observed in Ref. [90] a comparable capture efficiency of a 3D sample, however they investigated QD structures that strongly differ from the ones assumed here.

4. Comparison of 2D and 3D scattering

1. Thermalization of the high-energy carriers within GaAs towards the band edge.
2. Transport of the carriers (drift and diffusion) to the mesoscopic structures.
3. Capture in the 2D reservoir, if existent.
4. Capture and relaxation in and within the QDs.
5. Radiative recombination from the observed level (here QD-GS).

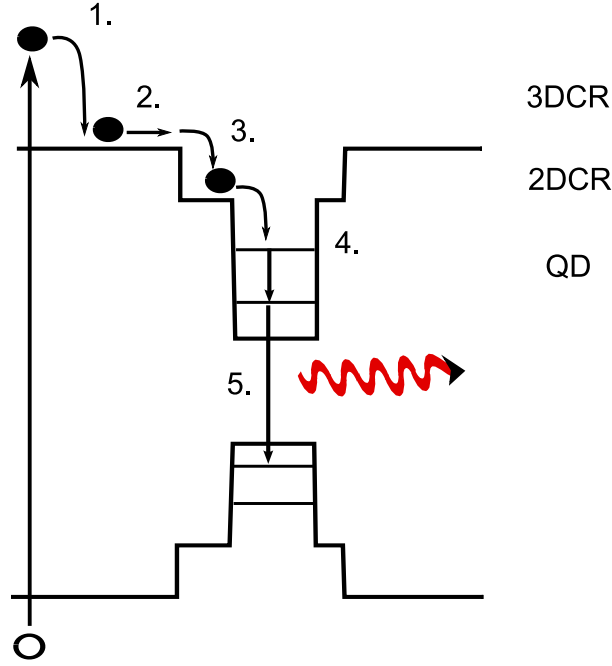


Figure 4.11.: Scheme of the processes involved in the PL-rise time, according to Ref. [3] .

In reality, the order of these processes could be partly mixed. In this thesis, step 4, the capture and relaxation in the QD, is investigated theoretically.

For comparison with the experiment, Eqs. (4.4) to (4.8) will be used to define the filling time of the QD-GS

$$\tau_{\text{fill}} = \frac{1}{2} \left[S_{\text{GS,cap}}^{\text{in}} + S_{\text{GS,rel,2,eh}}^{\text{in}} + \left(\frac{2}{\left(S_{\text{ES,cap}}^{\text{in}} + S_{\text{ES,rel,2,eh}}^{\text{in}} \right)} + \frac{2}{\frac{1}{2} \left(S_{\text{GS,rel,1}}^{\text{in}} + S_{\text{GS,rel,2,e}}^{\text{in}} - S_{\text{GS,exch.}}^{\text{in}} + S_{\text{GS,3QD}}^{\text{in}} \right)} \right)^{-1} \right]^{-1}. \quad (4.14)$$

τ_{fill} is the inverse scattering rate of the direct capture, plus twice the rate of the cascading

processes, accounting for the two excited states⁵. The suffixes e and eh denote the pure electron and the mixed electron–hole contribution to a certain process. The factor $\frac{1}{2}$ in front of Eq. (4.14) stems from the spin degeneracy.

τ_{fill} should mirror the processes in step 4 of the cascading scheme Fig. 4.11. In agreement with Refs. [20, 62] and Fig. 4.16, it was assumed that filling of the hole states is faster than for the electron states. Accordingly, there is always a hole present in the QD. As a result of that, the recombination time is governed by the electron filling time.

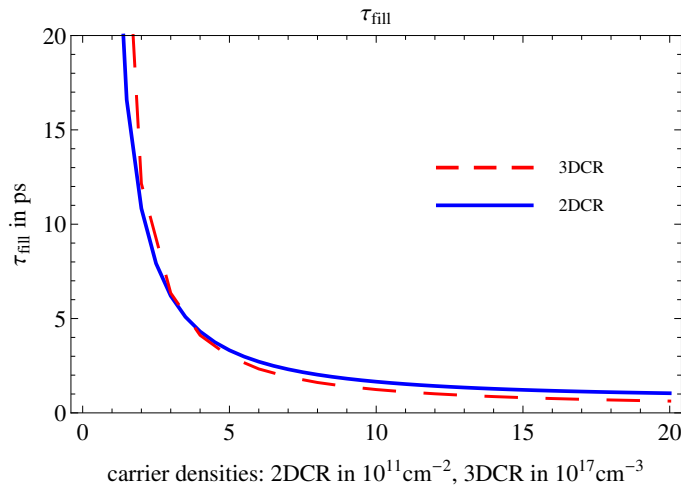


Figure 4.12.: Calculated rise time τ_{fill} .

If the highly nonlinear onset of Coulomb scattering at low densities is omitted, the calculated filling times reveal an approximately $\frac{1}{n}$ behavior for higher carrier densities, cf. Fig 4.12. This shows that the bottleneck for the QD filling are the capture processes, with their approximately linear rise for medium and higher densities, cf. Fig 4.5. This is in agreement with a dynamic simulation of the long-time behavior by Majer et al. [62]. However, here the close similarity of the rise times for the 2D and 3D samples is of higher significance.

The latter, is in agreement with the results of Sanguinetti et al. In Ref. [30], Sanguinetti et al. used time-resolved PL measurements to investigate a QD-3DCR system. They found both qualitative and quantitative behavior of the PL-rise time similar to typical QD-2D carrier reservoir samples investigated by Morris et al. [92]. From this, they concluded that

“...the two-dimensional character of the wetting layer is not relevant in determining the quantum dot capture...” (cite: Ref. [30], page 1, line 4–5 of the abstract).

In Ref. [4], Sanguinetti et al. tried to confirm their previous findings by comparing three QD devices, differing only in the dimensionality of the carrier reservoir: A QD-2D

⁵Note that in the relaxation processes Eqs. (4.5) to (4.8), both excited states are included, whereas in Eq. (4.14), there is twice the time for one relaxation path, producing the factor $\frac{1}{2}$ in front of the relaxation terms.

4. Comparison of 2D and 3D scattering

sample, a QD-3D sample, and a sample with QDs grown on a very thin WL. The latter one is assumed to have an intermediate dimensionality between 2D and 3D. Their main results concerning the PL-rise time can be seen in Fig. 4.13, which is taken from Ref. [4].

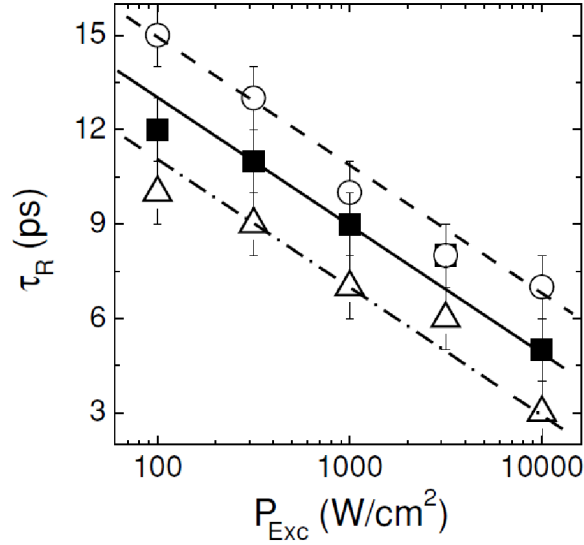


Figure 4.13.: . Photoluminescence rise time measured for a sample with wetting layer (triangles), a QD-3DCR system (squares) and a very thin wetting layer (circles). The Figure is taken from Ref. [4]

The plot parameter in Fig. 4.13 is the optical excitation power P_{exc} . It is a measure for the carrier density. Over several orders of magnitude of the excitation power P_{exc} , they found similar PL-rise times for all three samples. From this they concluded that the reservoir dimensionality is not significant for the carrier capture and relaxation, which is in agreement with the findings in this thesis.

However, even though the idea of comparing equal QDs with different reservoirs in this thesis is the same as in Ref. [4], a direct comparison of the results is not possible for several reasons:

- Although the QDs the various experimental samples have the same structure, the presence of a 2D carrier reservoir changes the energy spacings in the QDs. These were found to be sensitive parameters for Coulomb scattering rates (cf. Ref. [85]). In the situation of the Ref. [4], that would favor scattering from the 2D reservoir.
- In the experiment, electron-hole pairs were created in the bulk region via optical excitation. If at least one of the relaxation or recombination processes in the cascading scheme Fig. 4.11 is significantly slower than step 4. (capture and relaxation in the QDs), it would mask possible extreme differences between the different samples in step 4.
- It is not clear which excitation power causes which carrier density. Especially the

density in the respective reservoirs might strongly differ for the same excitation power.

- The QDs in the experiment are grown in a GaAs / AlGaAs system. Therefore they differ from those assumed here.
- The calculations in this thesis were performed for a system in a quasi equilibrium. In the experiment the carrier distributions were probably far away from equilibrium. Furthermore Eq. (4.14) is a sum over quasi equilibrium scattering rates. For better comparison, the fill time should be extracted from a dynamic calculation for the switch-on dynamics, cf. Ref. [93]. That would be closer to the experimental approach of determining τ_r .

However, although a direct comparison between the experimental findings and the calculations in this thesis is not useful, a rough comparison seems to be appropriate.

- There are several measurements [3, 91, 94] in which the different relaxation steps in a QD-2D reservoir system were time-resolved. However, in Ref. [3], the importance of phonon scattering is highlighted. Nevertheless, they indicate that the QD capture and relaxation is not magnitudes faster than the other processes. Hence, it leads to a significant footprint in the PL-rise time. As a result, the comparison of the PL-rise times in the experiment of Sanguinetti et al. [4] should reflect a comparison of the QD capture and relaxation times in step 4. in Fig. 4.11.
- The different material systems cause different input parameters. However, in Sec. 4.3.8 it will be shown for the capture processes that the main conclusion remain robust versus parameter variations.
- The effect of potentially different carrier densities in the 2DCR and 3DCR for the same excitation power can be estimated by noting that (a) the excitation power is varied over several orders of magnitude and (b) the PL-rise times stay in the same order of magnitude for all these excitation powers, cf. Fig. 4.13. In consequence, the results found by Sanguinetti et al. remain robust versus significantly different carrier densities.

Comparing the theoretical calculations Fig. 4.12 with the experimental findings Fig. 4.13, it is conspicuous that the curves have different shapes. This could be explained by the different plot parameters (P_{exc} in the experiment versus carrier density $n_{2D/3D}$ in the calculations). Furthermore, the experiment is a measure for a cascade of partially very different processes, whereas the calculations focus on the capture and relaxation into the QD. The latter arguments and the different material system also explain the quantitative differences.

Nevertheless, **the central conclusions of the theoretical and the experimental investigations are in agreement, namely that the reservoir dimensionality does not significantly affect the scattering rates.**

The comparison with the experiment highlights a great advantage of the theoretical calculations. Due to experimental settings, it is not possible to separate certain effects. As a consequence, the PL-rise time is a measure for a bunch of different processes, not

4. Comparison of 2D and 3D scattering

just the QD-reservoir transition that is the focus in the papers by Sanguinetti et al.. The theoretical investigation in this thesis enables selective study of specific processes. This allows to support the experimental observations.

4.3.8. Parameter studies

To confirm the previous findings that the reservoir dimensionality is not significant for the filling of the quantum dot states, parameter studies were done. These were intended to answer the following questions:

1. What is the influence of the reservoir height L entering Eq. (4.9)⁶?
2. Are the previous findings robust versus parameter variations?
3. Are the 2D and 3D scattering rates still similar, if the chemical potential μ is a plot parameter?
4. What is the influence of shifted Fermi-distributions to simulate a current flow through the device?

In this section, discussion is limited to the capture process in the excited state $S_{\text{ES,cap}}^{\text{in}}$. In dynamical calculations of a QD-2D sample similar to the system investigated here, Majer et al. [62] found that for the long-time behavior, this capture process is a bottleneck for filling the QD-GS. Therefore that limitation is deemed appropriate.

1. Dependency on the effective reservoir and QD height

Via Eq. (4.9), the effective height L of the 2D reservoir determines the ratio between related 2D and 3D carrier densities. Hence, it is necessary to investigate the robustness of the previous findings versus variations of the parameter L . Note that, for a given device, L has a fixed, computable [47] value. And as a result, the ratio Eq. (4.9) is, in principle, fixed.

The ES capture rates depicted in Fig. 4.14, basically show the behavior described in Fig. 4.5: Scattering in the QD-3D sample is less efficient for low carrier densities, whereas it becomes more efficient for higher densities. In particular, the 2D and 3D rates have the same order of magnitude. This supports the idea that the previous findings are not artifacts of the parameter L .

Figure 4.14 illustrates that the 3D rates increase with increasing L , whereas the 2D rates decrease (note the different scaling factor x in Fig. 4.14 for the 2D reservoir). This seems to be a principal difference in the behavior of the 2D and 3D rates. Furthermore, the opposite dependency on L partly (over-)compensates for the effect of a changed ratio of 2D and 3D carrier densities: As a result of Eq. (4.9), a large effective height L favors the 2D carrier density compared to the 3D one. Therefore, one might have expected higher in-scattering efficiency in the 2D sample, as long as the blocking regime is not reached.

However, Fig. 4.14(c) clearly reveals that the 2D rate approaches its maximum, leading to an evidently smaller scattering rate for high densities. This behavior is a

⁶ $n_{3D} = \frac{n_{2D}}{L}$

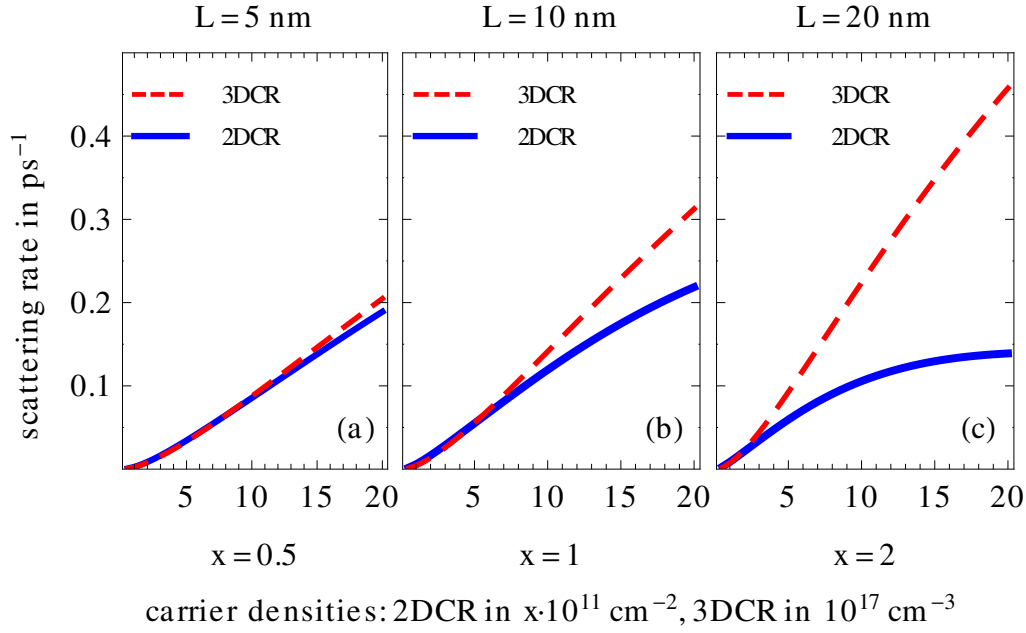


Figure 4.14.: $S_{ES,\text{cap}}^{\text{in}}$: (a) $L = 5 \text{ nm}$, (b) $L = 10 \text{ nm}$, (c) $L = 20 \text{ nm}$. The density range of the 3DCR was kept constant, whereas the density range of the 2DCR differs in the figures above, see scaling factor x .

consequence of the two regimes. First, they increase with increasing carrier density, due to the increasing number of scattering partners. Eventually, for higher carrier densities, they start to decrease due to Pauli blocking, described by the factor $(1 - \rho_i^{\lambda=e,h})$, cf. Eq. (3.11). This is typical for scattering rates, cf. Ref. [63].

However, here there are hints that the faster saturation of the 2D reservoir is essentially a parameter effect and not an articulate difference between the 2D and 3D samples. The carrier density affects the occupation probability $\rho_i^{\lambda=e,h} = f_i^{\lambda=e,h}$ via the chemical potentials $\mu_{2\text{D}/3\text{D}}^{\lambda}(n_{2\text{D}/3\text{D}})$. As a consequence, it also affects the point (for a certain process) at which Pauli blocking sets in. For a given 2D carrier density $n_{2\text{D}}^1$, the height L of the 2D carrier reservoir defines the carrier density $n_{3\text{D}}$ in the related 3D carrier reservoir. As a result, L “controls” the point relative to $n_{2\text{D}}^1$ at which Pauli blocking sets in for the 3D system.

Nevertheless, the 3D density of states supports a delayed onset of Pauli blocking effects in the 3D rate compared to the 2D rate, since the increasing number of high-energy states suppresses Pauli-blocking.

For usage in QD lasers Ref. [85] suggests 2D reservoir densities below the range plotted in Fig. 4.14(c), so that the blocking regime might not be reached for typical parameters.

In general, the existence of two regimes, and the different transition points in those regimes for the 2D and 3D rates, could possibly cause significantly different scattering rates.

4. Comparison of 2D and 3D scattering

2. Robustness concerning parameter variations

To confirm that the previous findings are not an artifact of the chosen parameters, the response of parameter variations will be examined here. Therefore the excited state capture rate $S_{ES, \text{cap}}^{\text{in}}$ is calculated for a 2D and a 3D sample with changed input parameters, cf. Fig. 4.15:

- The effective masses of the 3D carrier reservoir are artificially adapted to the masses of the 2D carrier reservoir.
- The energy spacings are changed. These parameters were found to be sensitive for the scattering rates [85].
- The layer density of the mesoscopic structures in the z-direction is adapted to the QD area-density, so that it is homogeneous in all directions.

All parameters can be found in Tab. F.3.

To investigate the effect of varying effective masses, and for completeness, the scattering rates of the holes are calculated, cf. Fig. 4.16. The effective hole masses are approximately ten times higher than the related electron masses and thus reflect a strong change in this parameter.

The calculations are done for three different values of L , to exclude the effects of Eq. (4.9), as discussed in the previous section.

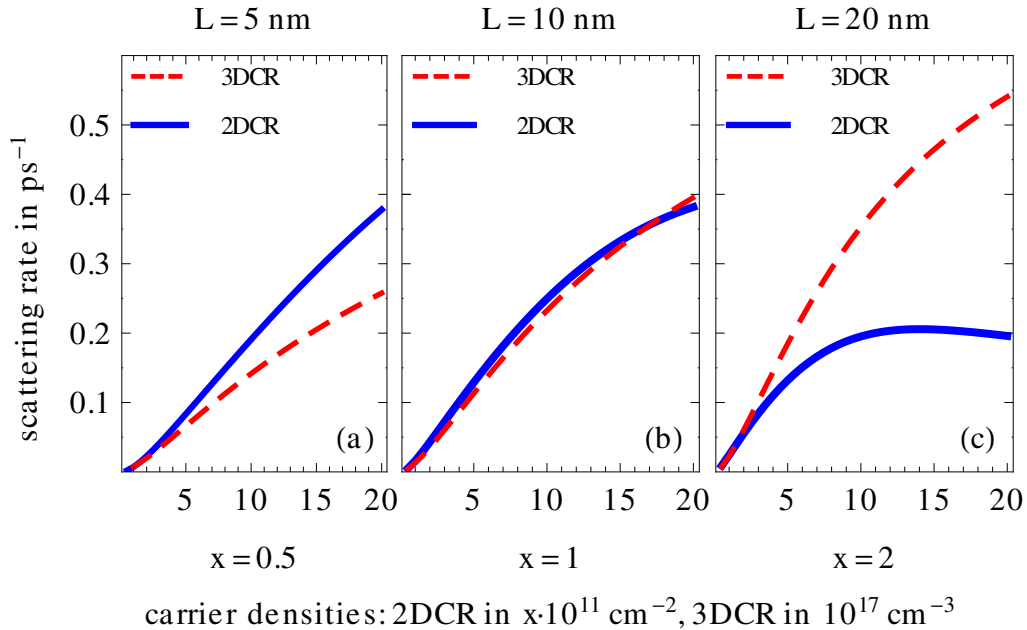


Figure 4.15.: $S_{ES, \text{cap}}^{\text{in}}$ for different parameters, see table F.3: (a) $L = 5 \text{ nm}$, (b) $L = 10 \text{ nm}$, (c) $L = 20 \text{ nm}$

In Fig. 4.15(a) and (b), the 2D rates are not significantly higher than the 3D ones for a wide density range. This supports the statement that the detailed behavior of the

scattering rates is strongly parameter-dependent cf. Sec. 4.3.2. In Fig. 4.15(c), the 2D rate is higher for low carrier densities, but reaches the blocking regime relatively quickly. Therefore, the 3D rate exceeds the 2D one with higher carrier densities.

In Fig. 4.16 the hole-ES capture rates are shown for the parameter sets Tab. F.2 (Fig. 4.16 (left)) and Tab. F.3 (Fig. 4.16 (right)).

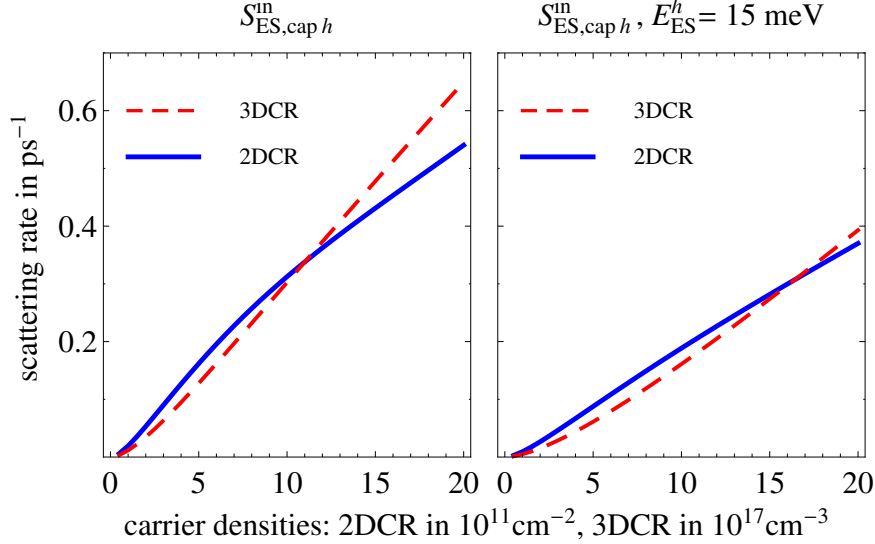


Figure 4.16.: $S_{ES,cap}^{in}$ for holes, (left): parameters of Tab. F.2, (right): parameters of Tab. F.3.

The rates of the 2D- and 3D sample are very similar under both parameter sets.

The absolute value of the rates plotted in Fig. 4.15 and 4.16 changes due to the different choice of parameters. But more importantly, the qualitative behavior is basically the same for the changed parameter sets. Note that the parameter set Tab. F.3 in particular represents a significant change to the QD wavefunctions, as can be seen from the factor $\frac{\hbar}{2m_{\Lambda}\omega_{QD}^{\Lambda}}$, cf. Eqs. (2.14) and (2.15). Compared to the standard set in Tab. F.2, this quantity changes by a factor of about 1.7 for electrons and 0.3 for holes. This suggests that the findings from the previous sections are not artifacts of the chosen parameter set, but describe general tendencies.

3. Comparison of the capture rates as functions of the chemical potential

As discussed in Sec. 4.2, Eq. (4.9) is not the only way to relate the 2D and 3D scattering rates. Another useful way is to relate the rates as a function of the chemical potential μ_e . Accordingly, the two samples are compared under conditions of equal chemical potentials for the electrons in the 2D and the 3D reservoir respectively ($\mu_e := \mu_e^{2D} = \mu_e^{3D}$)⁷. The mixed electron-hole processes are omitted to avoid dealing with deviations from charge

⁷ One should note that the 2D reservoir and the 3D reservoir belong to different samples. Therefore, this assumption has nothing to do with (quasi) equilibrium between the 2D and 3D reservoirs.

4. Comparison of 2D and 3D scattering

neutrality in the respective reservoirs⁸. Since the pure electron contribution is dominant for the chosen parameter set, this is a suitable limitation.

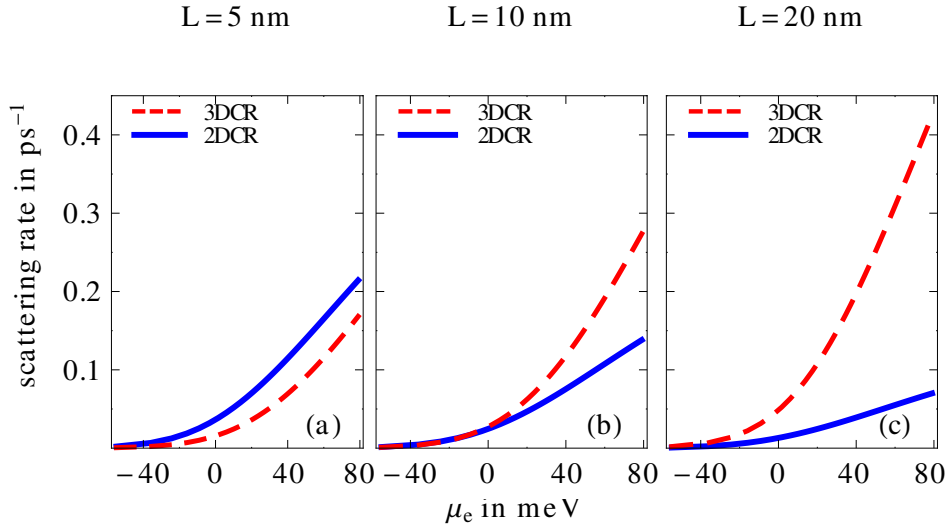


Figure 4.17.: pure CB-electron capture rates as a function of the chemical potential μ_e for different (effective) well width L

The rates plotted in Fig. 4.17 show similar behavior to those in Fig. 4.14: The 2D capture rate decreases with increasing well width L , whereas the 3D rate increases. Here, this effect is not compensated for by the density ratio Eq. (4.9), as is the case in Fig. 4.14. As a result, a more pronounced difference in the 2D / 3D rates for $L = 20$ nm is observed. However, despite this difference, the rates still have the same order of magnitude. This confirms the findings earlier in this chapter, since the main observations remain the same for different ways of comparing the 2D and 3D scattering rates.

In Fig. 4.17 the 2D rate does not reach the blocking regime. This confirms that the onsetting Pauli blocking in Fig. 4.14(c) is a parameter effect caused by the way of relating the 2D and 3D carrier densities⁹.

4. Shifted Fermi-distribution

So far, Fermi-distributions centered around zero were assumed. To simulate a current flow through a device, it is a typical approximation to assume shifted Fermi-distributions. Therefore the 3D-ES-capture rate is calculated for a Fermi-distribution shifted in the

⁸ In practice, charge neutrality would be ensured by shifts of the energy bands at the respective reservoir interfaces. This self-consistently ensures charge neutrality. Note that the hole density, which is assumed to be equal the electron density, also enters the pure electron scattering rate via screening effects.

⁹ Nevertheless, Eq. (4.9) seems to be the most useful way to relate the scattering rates.

z-direction:

$$f^\lambda(E(k_{||}, k_z)) \rightarrow \begin{cases} f^e(E(k_{||}, k_z + \Delta k)) \\ f^h(E(k_{||}, k_z - \Delta k)) \end{cases}$$

with

$$\Delta k = \frac{n_{3D}}{n_{3D}^0} \text{ nm}^{-1} \quad (4.15)$$

and $n_{3D}^0 = 5 \times 10^{18} \text{ cm}^{-3}$. Equation (4.15) is chosen arbitrarily. This represents a rough estimate of the situation in a VCSEL-device, where the current flows mainly in the growth direction, cf. Fig. 2.6. Hence it should not affect the carrier distribution in the 2D reservoir. For small shifts the influence on the capture rates is negligible, as

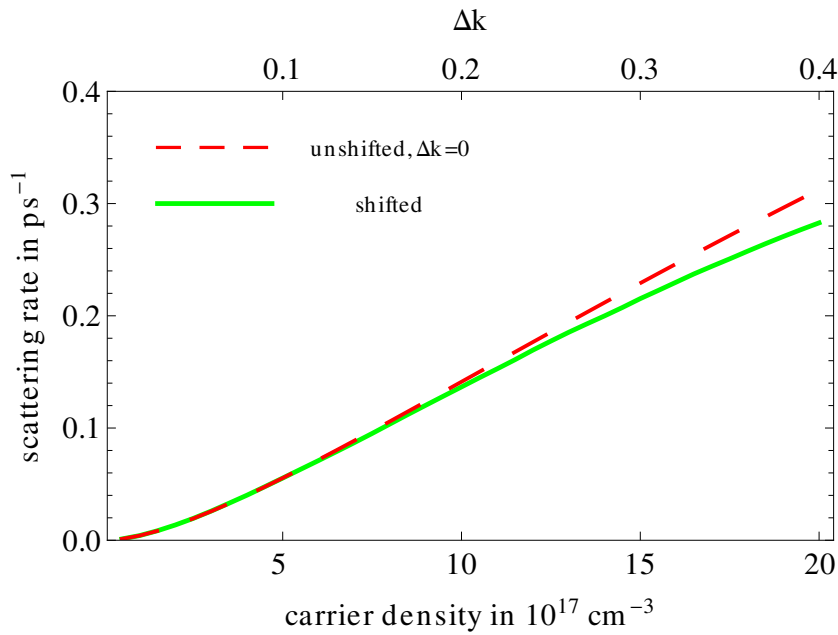


Figure 4.18.: Excited state capture rates for shifted and unshifted Fermi-distributions.

be can seen from Fig. 4.18. Higher shifts Δk , cause a reduction in the capture rate. However, within the parameter range under consideration, the difference remains small. This suggests that the previous findings remain robust versus moderate changes to the carrier distributions caused by the current flow.

4.3.9. Direction dependency of the scattering

In contrast to 2D structures, in which the carriers have only in-plane momentum, for 3D structures, the question arises from which direction (here it is only differentiated between in-plane and z-direction) the carrier has its highest in-scattering efficiency. For

4. Comparison of 2D and 3D scattering

this purpose, one can define a capture efficiency $Ec^D(k_{c,\parallel}, k_{c,z})$ by

$$Ec^D(k_{c,\parallel}, k_{c,z}) := \frac{2\pi}{\hbar} \int d^3k_a \int d^3k_b \int d\vartheta_c k_{c,\parallel} \times |W_{D\vec{k}_a\vec{k}_b\vec{k}_c}|^2 f_{k_b} f_{k_c} (1 - f_{k_a}) \delta(\varepsilon_D + \varepsilon_{k_a} - \varepsilon_{k_b} - \varepsilon_{k_c}). \quad (4.16)$$

This function describes the scattering efficiency in dependency of the absolute value of the in-plane- and z-wavevectors ($\vec{k}_c = (\vec{k}_{c,\parallel}, k_z)$, $|\vec{k}_{c,\parallel}| = k_{c,\parallel}$) of the electron that is scattered into the QD. In Fig. 4.19, one can see that the sum $Ec^{ES}(k_{\parallel}, k_z) + Ec^{ES}(k_{\parallel}, -k_z)$

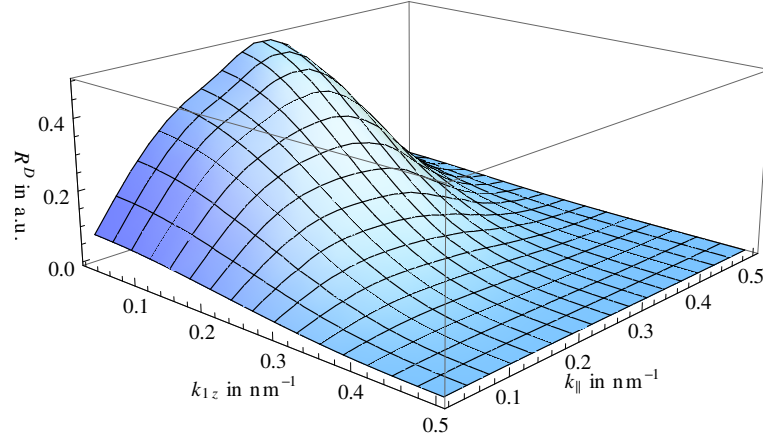


Figure 4.19.: Sum of $R^{ES}(k_{\parallel}, k_z) + R^{ES}(k_{\parallel}, -k_z)$ versus the absolute values of the in-plane- ($|\vec{k}_{\parallel}| = k_{\parallel}$) and z-wavevector ($|k_z|$) at a density of $5 \times 10^{17} \text{ cm}^{-3}$

decreases for an increasing absolute value of the z component of the in-scattering electron. The bow-shaped progress of the curve in dependence of the absolute value of the in-plane wavevector might be caused, on the one hand, by the interplay of a decreasing efficiency of the scattering processes with higher momentum transfer and the increasing density of states on the other. The latter causes an increasing number of possible scattering partners. Figure 4.19 suggests that scattering becomes more efficient for small absolute values of the z-wavevector, which might be of interest in technical application. The decreasing scattering efficiency for higher absolute values of k_z could be assumed from Fig. 4.18. In particular, one might wonder why the reduction in Fig. 4.18 is relatively small even for high shifts Δk . However, that conclusion is not useful due to the differences in the plotted functions.

4.3.10. The role of OPW approaches

In Sec. 2.4.2, it was discussed, that there are additional possible ways of constructing the 3D-reservoir orthogonalized plane waves (OPWs) beyond Eq. (2.22). Figure 4.20 shows the ES capture rate for various OPW approaches Eqs. (2.22)–(2.25). For comparison, the blue curve in Fig. 4.20 shows the 2D reservoir rate, corresponding to Eq. (2.21). The

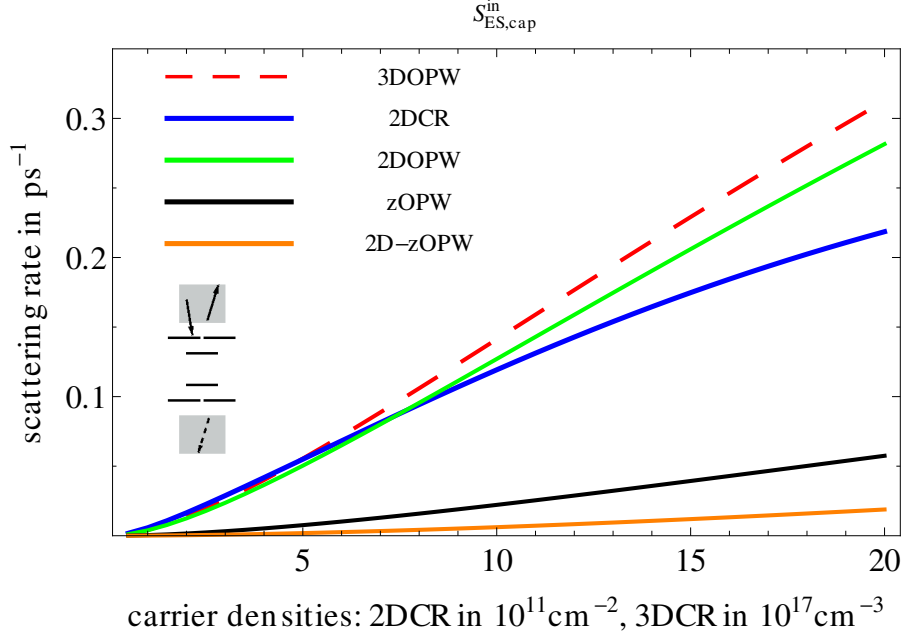


Figure 4.20.: Excited states capture rate for different OPW approaches.

pronounced difference between the various OPW states is surprising, since, in principle, all of these different OPW-forms are possible approaches.

One can see that an orthogonalization of the z-direction on its own in the $|\psi_{\mathbf{k},2D \times zOPW}\rangle$ - and $|\psi_{\mathbf{k},2D \times 2D-zOPW}\rangle$ -bases leads to a significant reduction in the scattering rates. By contrast, the restriction of the orthogonalization to the in-plane part of the QD wavefunction in the $|\psi_{\mathbf{k},2DOPW}\rangle$ -basis causes only minor corrections compared to $|\psi_{\mathbf{k},3DOPW}\rangle$. This last was also observed for QD-2D reservoir systems, cf. Ref. [20]. However, to explain the greater impact of the orthogonalization in the z-direction, one should look at the wavefunction: It is intuitive that the overlap between the reservoir plane waves (PWs) in the z-direction, and the sinus-shaped QD-z-wavefunction Eq. (2.16) is, on average, higher than the overlap of the in-plane PWs with the Gaussian-shaped QD in-plane wavefunctions.

Nevertheless, the question arises why the scattering rates of the $|\psi_{\mathbf{k},3DOPW}\rangle$ - and the $|\psi_{\mathbf{k},2D \times zOPW}\rangle$ -basis differ so much, although both have perturbed z-wavefunctions? This can be understood (i) with the empirical knowledge that OPW corrections to PW basis lead to a reduction in the scattering rates compared to the PW-rates [20, 21] and, in combination, (ii) by looking onto the spatial extension of the QD perturbation to the PW states, cf. Fig 4.21:

- In the $|\psi_{\mathbf{k},3DOPW}\rangle$ -basis, the perturbations are restricted to the effective QD volume, cf. Fig 4.21 a).
- For the $|\psi_{\mathbf{k},2D \times zOPW}\rangle$ and $|\psi_{\mathbf{k},zOPW}\rangle$ -bases, the z-orthogonalization is not restricted to the QDs, but to the whole effective volume of the QD layers, cf. Fig 4.21 d) and c).

4. Comparison of 2D and 3D scattering

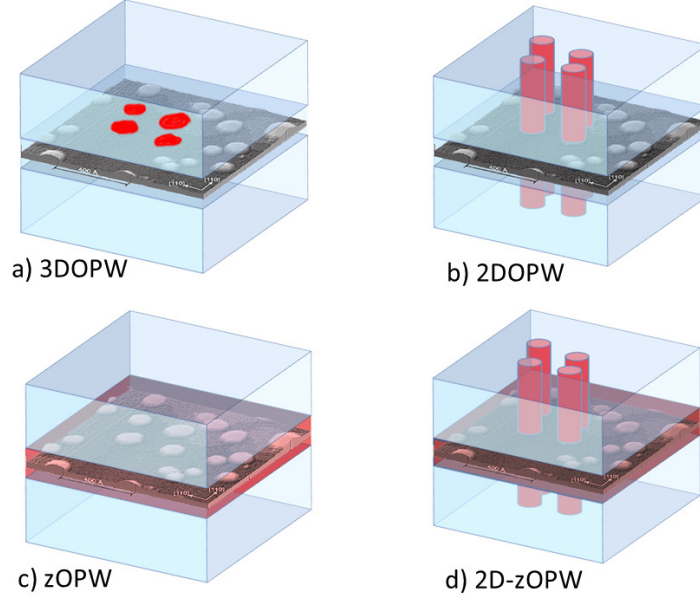


Figure 4.21.: Illustration of differences between the different OPW-types. The red regions indicate volumes where QD corrections to the PW wavefunctions appear (not all volumes are marked). A scanning tunneling microscope image by Marquez et al. [1] has been used.

This last is a much stronger perturbation of the PW states. Together with (i), this explains the significantly smaller scattering rate of the $|\psi_{\mathbf{k},2D \times zOPW}\rangle$ and $|\psi_{\mathbf{k},zOPW}\rangle$ -basis. A similar argumentation also explains why the scattering rates of the $|\psi_{\mathbf{k},3DOPW}\rangle$ -basis are even higher than those of the $|\psi_{\mathbf{k},2DOPW}\rangle$ -basis, although the $|\psi_{\mathbf{k},3DOPW}\rangle$ -basis contains corrections to the z-direction: Here, the in-plane corrections are extended through out the entire quantization volume in the z-direction, cf. Fig 4.21 b) . As a result, the perturbation of the PW-states is greater than the punctual perturbation of the $|\psi_{\mathbf{k},3DOPW}\rangle$ -bases, cf. Fig 4.21 a) .

Due to the localization of the QD perturbations, the $|\psi_{\mathbf{k},3DOPW}\rangle$ -basis is the most suitable choice of the presented bases. It reflects the settings better than the others.

However, the scattering rates of the $|\psi_{\mathbf{k},3DOPW}\rangle$ -basis and the $|\psi_{\mathbf{k},2DOPW}\rangle$ -basis are very similar. This is important, since the $|\psi_{\mathbf{k},2DOPW}\rangle$ -basis fulfills the ortho-normalization condition $\langle \psi_{\mathbf{k}_1,2DOPW} | \psi_{\mathbf{k}_2,2DOPW} \rangle = \delta_{\vec{k}_1, \vec{k}_2} = \delta_{\vec{k}_{1,||}, \vec{k}_{2,||}} \delta_{k_{1z}, k_{2z}}$, without any further assumptions on the QD-distribution in the z-direction. As discussed in Sec. A, this was a critical point for the $|\psi_{\mathbf{k},3DOPW}\rangle$ -basis. Consequently, the orthogonality expressed by Eq. (A.7) seems to be an appropriate assumption.

4.4. Conclusions

We compared scattering rates of a QD-2D sample with those of a QD-3D sample. In the presented calculations, the significant rates showed similar behavior in terms of

the carrier density dependency. The rates are of the same order of magnitude. In agreement with experimental observations, a reduction of the scattering efficiency due to a greater dimensionality gap between QD and 3D reservoir was not observed in the significant scattering processes. This holds for different parameter sets, as well as for different ways of relating the 2D and 3D rates. This suggests that in many applications the dimensionality of the carrier reservoir is insignificant for the Coulomb interaction with QD states. However, the detailed behavior differs for the two different reservoir types. They showed an opposing behavior in the QD height in particular. Furthermore, the 3D rates showed to be less sensitive to constraints of momentum integration. The latter effect could cause a bottleneck effect especially in the QD-2D sample. Then, the scattering rates are considerably different. In turn, the decreasing 3D density of states for lower energy states could reduce the 3D rate. However, these effects might be an artifact of the Markovian treatment.

The choice of the reservoir wavefunctions has been shown to have considerable impact on scattering rates. Therefore the basis should be chosen with caution.

4.5. Outlook

It was found that filling of the QD from a 3D reservoir is, in principle, not less efficient than from a 2D reservoir. As a result, the question arises whether it is a suitable assumption to leave the 3D states out of consideration in a sample with a 2D reservoir, as is commonly done (including here), cf. Refs. [20, 18]. The reason for disregarding the 3D states is the larger energy gap between the QD states and the 3D reservoir, as compared to the 2D one. This causes a significantly lower reservoir occupation in the 3D reservoir. Furthermore it is assumed that the higher energy transfer of participating states reduces the scattering efficiency, due to the momentum transfer, that is on average higher, cf. Appx. B. However, these assumptions seem reasonable for a dot in a well system, with a large QW confinement energy of several hundred meV. For simple QD-wetting layer systems, the wetting layer confinement energy is below 100 meV in some cases. Therefore, the role of the 3D reservoir should be investigated. This applies not only to direct capture in the QD states, but the additional reservoir states also give rise to further scattering channels, including states of all three subsystems. Furthermore, the inclusion of 3D reservoir states might be crucial for a detailed understanding of the pump-probe experiments. For example, Sun et al. [95] observed in time-resolved photoluminescence measurements that:

“Under high excitation intensity, the electronic states in the dots were populated mainly by carriers directly captured from the barrier.” (cite: Ref. [95], page 1, line 11–12 of the abstract)

The 3DOPWs used in this thesis are not suitable for an investigation of a full QD-2D-3D system, as they are not orthogonal to the 2D reservoir states. The construction of a suitable basis could be done via the continuum states of a finite potential well. These states would be orthogonal by construction to the corresponding bound states, which then should be the z-wavefunctions of the 2D reservoir, cf. refs. [96, 97]. In in-plane direction the 2DOPW wavefunctions should be still suitable for 2D and 3D reservoirs. With such a model, a full microscopic description of the active region should be possible.

4. Comparison of 2D and 3D scattering

An intermediate step, before a full model, would be an investigation of the dynamics of a QD-3D sample via a rate equation system, cf. Refs. [34, 63, 85, 98]. This might be interesting, since the dynamic behavior could differ from the QD-2D systems, due to the much higher number of carriers in the 3D reservoir.

Besides the findings presented here, the model presented represents a good starting point for further investigations.

5. A microscopic gain model

In this chapter, a microscopic gain model will be presented. First, the gain formula under consideration will be discussed. Section 5.1 then discusses the results of the microscopic model for the dephasing time T_2 . Finally, the numerical results of the gain calculation will be presented.

The gain formula Eq. (5.1) describes the contribution of the QDs to the material gain in dependence of the test beam frequency ω and the 2D carrier density n cf. [99, 19, 70].

$$g(\omega, n) = -\frac{|d_{vc}|^2 \omega}{n_r c} \int \frac{[n_{\text{QD}} - n_h(n) - n_e(n)] \Gamma_h(n)}{(\epsilon - \hbar\omega)^2 + \Gamma_h^2(n)} G(\epsilon) d\epsilon, \quad (5.1)$$

A detailed derivation of Eq. (5.1) can be found in Appx. E. The values of background permittivity ϵ_r , refractive index n_r , speed of light c and the dipole-moment d_{vc} are taken from the literature [69, 2, 93]. $n_{\text{QD}} = 2N_{\text{QD}}/(AL)$ denotes twice the QD volume density in the effective volume of the mesozoic structures. This factor also enters into the QD occupation factors $n_e(n) = n_{\text{QD}} f_{\text{QD}}^e(n)$ and $n_h(n) = n_{\text{QD}} f_{\text{QD}}^h(n)$. The microscopic nature of the gain formula (5.1) is reflected in the microscopically-determined homogeneous broadening $\Gamma_h = \frac{\hbar}{T_2}$, as well as its derivation via the microscopic polarization. The dephasing time T_2 describes the decay of the microscopic polarization. Details of its derivation within the limits of Born-Markov approximation and disregarded of Hartree-Fock energy shifts, as applied here, can be found in Sec. 3.3.1 and Appx. D. The sign of the gain is solely determined by the carrier inversion

$$n_{\text{QD}} - n_h(n) - n_e(n) = n_{\text{QD}} \left(1 - f_{\text{QD}}^e(n) - f_{\text{QD}}^h(n)\right).$$

5.1. Dephasing time and homogeneous broadening

Figure 5.1 depicts the dephasing time T_2 and the population lifetime $T_1 = (\sum_i S_i)^{-1}$. In contrast to T_1 , T_2 includes pure dephasing processes. The two quantities should fulfill approximately the relation¹ $T_2 = 2T_1$, disregarding pure dephasing, cf. Ref. [61] or Eq. (3.15). A comparison of both times allows for a good estimate of the influence of the pure dephasing processes.

In Fig. 5.1, one can see that the pure dephasing processes are particularly for carrier densities up to $20 \times 10^{11} \text{ cm}^{-2}$ of high importance. In turn, the impact of pure

¹ Note that the mixed relaxation process similar to Fig. 4.1 $S_{\text{GS,rel2}}^{\text{in}}(\beta)$, is taken into account only once.

5. A microscopic gain model

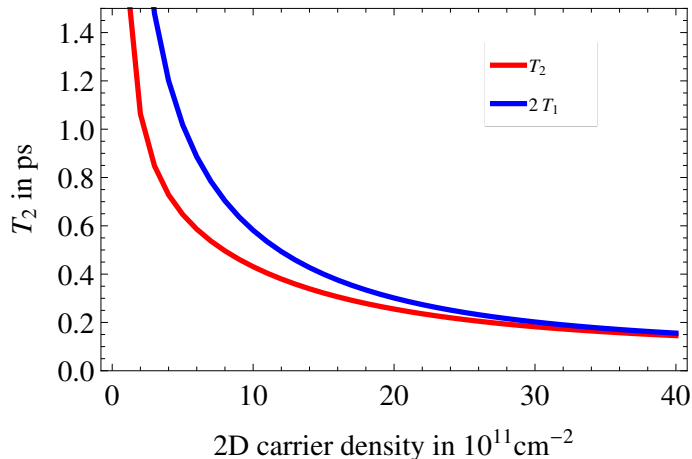


Figure 5.1.: Dephasing time T_2 and twice the carrier lifetime T_1 .

dephasing becomes negligible in the very high² density regime. Both quantities show an approximately $\frac{1}{n}$ behavior.

5.1.1. Comparison of the theoretical model with experiment

Borri et al. extracted the dephasing time from a four wave mixing experiment. Figure 5.2 (*right*) is taken from [61, 8]. It depicts homogeneous broadening $\gamma = \frac{2\hbar}{T_2}$ and population lifetime $\gamma_1 = \frac{\hbar}{T_1}$ of a multi-exciton transition, both measured for the GS transition. That means they investigated the s-shell transition in the presence of filled excited electron and hole QD states. Due to the differences in the systems investigated, a direct comparison to the results presented here is not useful. However, a comparison of the qualitative behavior seems appropriate.

Figure 5.2 reveals a monotonically increase of the broadenings with increasing carrier densities, and higher values of γ_h than of γ_1 , both in theory Fig. 5.2(*right*) and experiment Fig. 5.2(*left*).

In agreement with the experiment, the calculated data show an increasing difference between γ_1 and γ_h with increasing temperature. However, due to the lack of phonon processes and temperature-dependent energy shifts (e.g. via the Varshni equation [100]), the theory cannot be expected to reproduce the detailed temperature behavior of the experiment. The experimental data at 295 K show a steeper progression of the γ_h -curve as compared to the γ_1 -curve for high temperatures. Borri et al. attributed this behavior to Coulomb-induced pure dephasing. The calculated curves show approximately a shift of the γ_h -curve as compared to the γ_1 -curve. A steeper progression could be observed only for low³ carrier densities in the calculated curve at 300 K. One reason could be the restriction to a two level system, since important intra-dot dephasing channels are not

²High and low carrier regime refers to the density range under investigation.

³In principal, the lowest considered densities are still much higher than the intrinsic carrier concentration at 300 K, which is about $2.1 \times 10^6 \text{ cm}^{-3}$ for GaAs and $1.3 \times 10^{15} \text{ cm}^{-3}$ for InAs [47]. Therefore “low” refers to the density range under investigation.

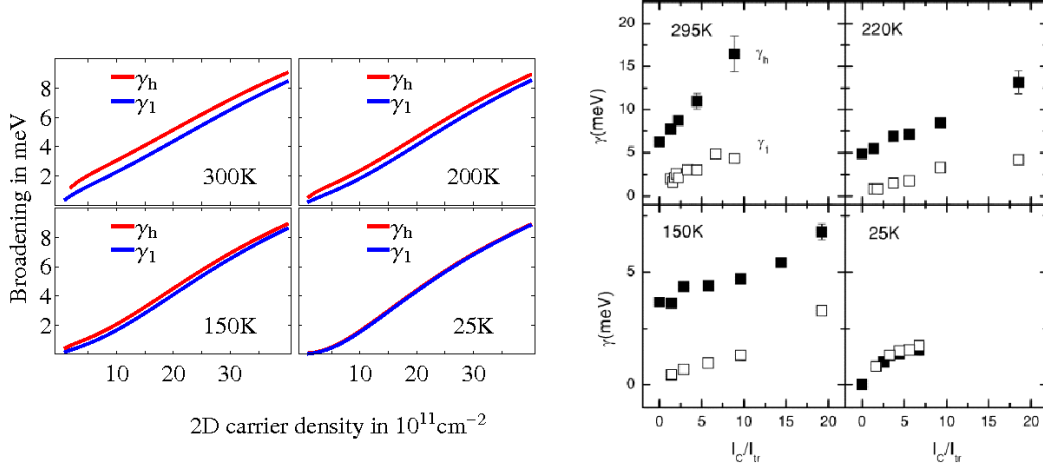


Figure 5.2.: Homogeneous broadening $\gamma_h = \frac{2\hbar}{T_2}$ and the population lifetime broadening $\gamma_l = \frac{\hbar}{T_1}$ for various temperatures. *left*: calculation, *right*: measured by Borri et al., taken from Ref. [61] ©2002 IEEE.

possible in such a system.

5.1.2. Comparison with a theoretical benchmark model

In this section results from the gain model of M. Lorke et al. [24, 69, 70] will be used as a benchmark. In that model, a non-Markovian treatment was used to determine homogeneous broadening. Hartree-Fock energy shifts, phonon scattering, and coupling to other polarizations are also incorporated in the Lorke model. Due to the incorporation of those couplings, the T_2 is not a useful quantity anymore. In the Lorke model, the homogeneous linewidth is determined via the full width at half maximum (FWHM) of a Lorentzian fit to the gain curve [69]. This value can be related to the homogeneous broadening $\gamma_h = \frac{2\hbar}{T_2} = 2\Gamma_h$ in the model presented here.

Furthermore the Lorke et al. model differs from the one presented here in details of the wavefunctions and screening effects. Figure 5.3(*bottom*) is taken from [69]. It depicts the homogeneous broadening calculated via the Lorke model versus the total carrier density⁴ in the system: $N_{\text{sys}} = n_{2D}^e + L n_{QD} f_{QD}^e = n_{2D}^h + L n_{QD} f_{QD}^h$. For low carrier densities, this leads to shifts in densities below 15%. For high carrier densities, the differences are negligible. Since Hartree-Fock renormalizations are not included, the deviations from total charge neutrality, caused by the assumption $n_{2D}^e = n_{2D}^h$ do not cause unwanted effects.

Figure 5.3(*top*) depicts the homogeneous broadening calculated with the model presented here. The fit function of the form $F(n) = a \left(\frac{n}{w_0}\right)^b$, with $a = 0.675605$ meV, $w_0 = 10^{11} \text{ cm}^{-2}$ and $b = 0.67$ follows the idea of a power law, as described in [69]. Approximately the same parameter set has been used as for the shallow dot [69]. However,

⁴ The unit in Fig. 5.3(*bottom*) should be cm^{-2} .

5. A microscopic gain model

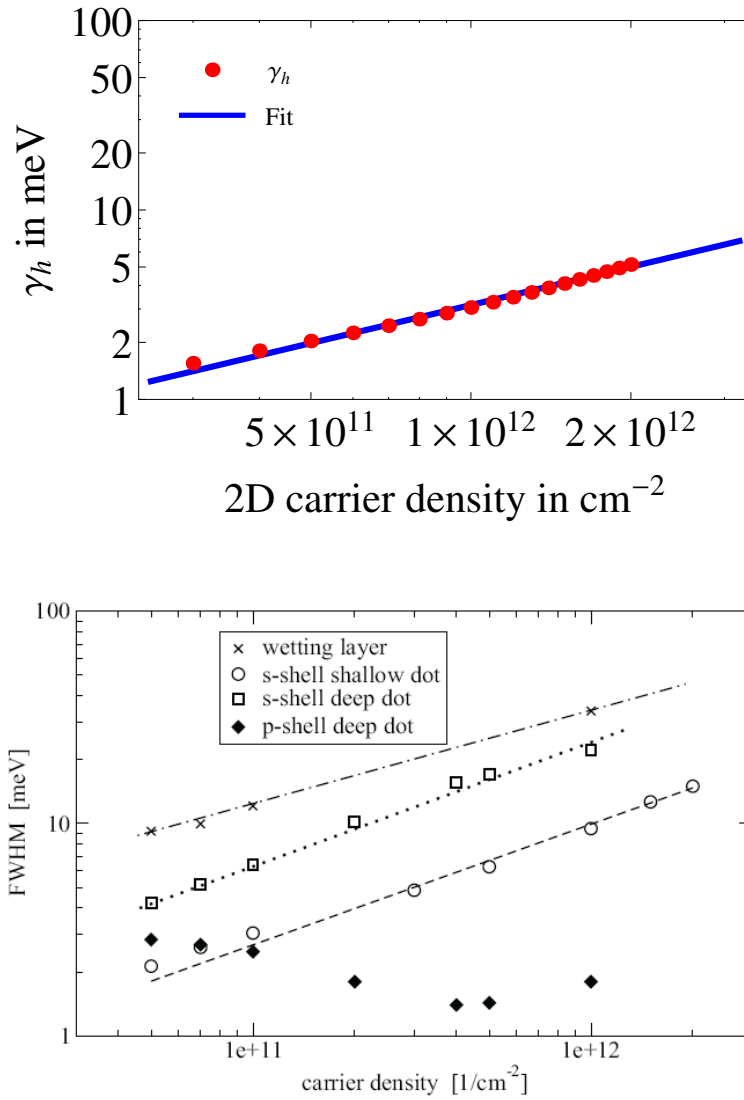


Figure 5.3.: *top*: homogeneous broadening $\gamma_h = \frac{2\hbar}{T_2}$ calculated via the eq. (3.15). *bottom*: homogeneous linewidth calculated by M. Lorke, taken from Ref. [69]

details about the QD wavefunctions might differ⁵

A comparison of the homogeneous broadening reveals qualitatively close agreement between the two models. However, quantitatively they differ by a factor of about three. If one assumes broadening due to phonon scattering of 2 meV, approximated by the broadening in Fig. 5.3(*bottom*) at very low carrier densities, quantitative agreement becomes slightly closer. For high densities, they differ by a factor of about two. However, the agreement in the high-density regime might improve, since via line broadening also the phonon scattering increases for high carrier densities.

⁵Here, different parameters enter the QD wavefunctions for electrons and holes.

5.2. Refractive Index

Figure 5.4 depicts the refractive index $n_r(\omega)$ for various carrier densities.

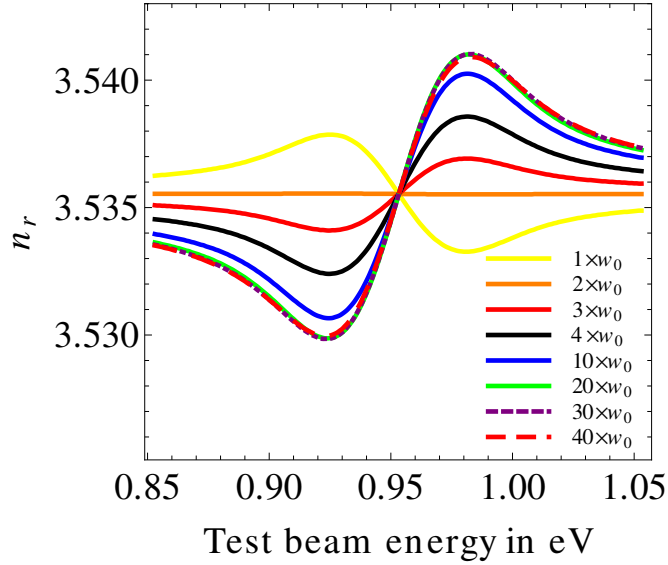


Figure 5.4.: Refractive index n_r for reservoir carrier densities $1, 2, 3, 5, 10, 20, 30, 40 \times w_0$, $w_0 = 10^{11} \text{ cm}^{-2}$. A Gaussian shaped inhomogeneous broadening of with $\gamma_{\text{inh}} = 50 \text{ meV}$ FWHM was assumed.

The formula

$$n_r(\omega) = \sqrt{\frac{1}{2} \left[\left(1 + \text{Re} \left[\frac{P_{QD}(\omega)}{\varepsilon_0 E(\omega)} + \varepsilon_{bg} \right] \right) + \left| \left(1 + \frac{P_{QD}(\omega)}{\varepsilon_0 E(\omega)} + \varepsilon_{bg} \right) \right| \right]}, \quad (5.2)$$

was used for the calculation, cf. Ref. [39] or Appx. E.3. The change in the refractive index induced by the QDs saturates for high carrier densities. However, the value of the refractive index is mainly determined by the background permittivity ε_{bg} . The changes caused by the QDs are relatively small. Consequently, for the calculation of the material gain via Eq. (5.1) it is appropriate to disregard the QD contribution. The well-known estimation [39]

$$n_r \approx \sqrt{\varepsilon_{bg}} \quad (5.3)$$

will be used.

5.3. Quantum dot material gain

Figure 5.5(right) depicts the QD contribution to the material gain for various carrier densities, described in (5.1). Due to the omission of Hartree-Fock energy renormalizations, the peaks all have the same position. Of course, neither phonon signatures nor signatures of the coupling between different polarizations can be observed, since neither

5. A microscopic gain model

effect was considered here. The folding of the Lorentzian-shaped homogeneous broadening and the Gaussian-shaped inhomogeneous broadening in Eq. (5.1) result in gain curves that have the shape of a Voigt profile [101].

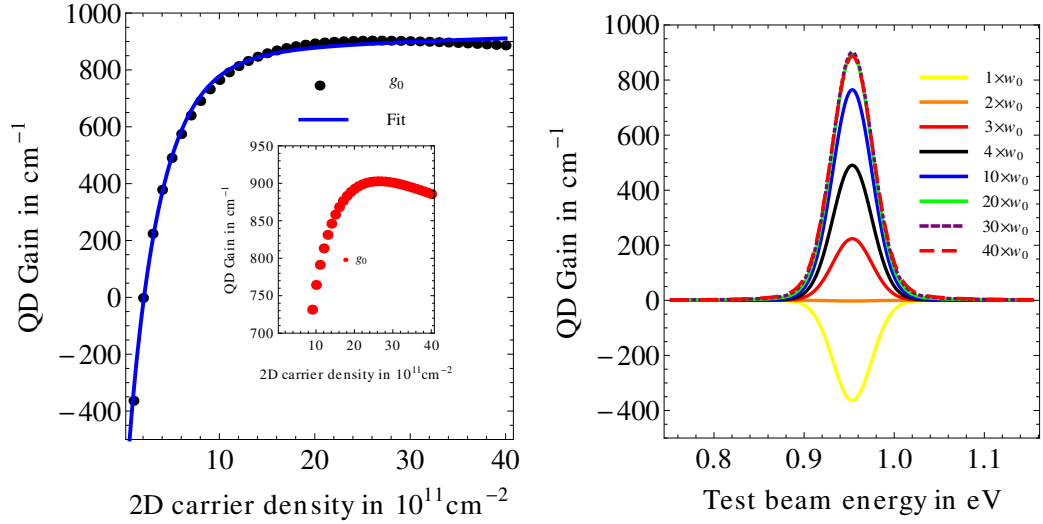


Figure 5.5.: *left*: Maximal value of the gain curves as a function of the reservoir carrier density. The inset depicts a cutout. *right*: QD-gain spectra for reservoir carrier densities $1, 2, 3, 5, 10, 20, 30, 40 \times w_0$, $w_0 = 10^{11} \text{ cm}^{-2}$. A Gaussian shaped inhomogeneous broadening of with $\gamma_{\text{inh}} = 50 \text{ meV}$ FWHM was assumed.

Figure 5.5(*left*) shows the maximal value of the gain curves versus the reservoir carrier density. Similar to the model of M. Lorke et al. [70], one can observe a reduction of the maximal gain for high carrier densities. The inset in Fig. 5.5(*left*) illustrates this behavior. In Fig. 5.5(*left*) a fit function suggested by M. Lorke [69] is shown. It has the form

$$g_0(n) = A \ln[n/n_0] + B \exp[-n/n_1], \quad (5.4)$$

with $A = 42.4731 \text{ cm}^{-1}$, $B = -1471.35 \text{ cm}^{-1}$, $n_0 = 1.93584 \times 10^{-8} \text{ cm}^{-2}$, $n_1 = 3.35303 \text{ cm}^{-2}$.

The gain reduction can be explained by the fact that, for high carrier densities, the carrier inversion is saturated, whereas the homogeneous broadening increases further [70]. In principle, in order to forecast this effect in a laser, a dynamic simulation, including optics, would have been necessary. In the laser regime, the QD inversion, and with it the onset of saturation, is strongly influenced by the optical field. Hypothetically, the saturation of inversion could appear at extremely high carrier densities. However, it is well known that ground state emission, and thus inversion, in QD lasers saturates at moderate carrier densities. Shahid et al. confirmed the effect of gain reduction in measurements [102].

In Fig. 5.6, the maximal QD gain (*left*) and the gain spectra at $n = 20 \times 10^{11} \text{ cm}^{-2}$

(right) are plotted for various homogeneous broadenings. In Fig. 5.6(left), one can see

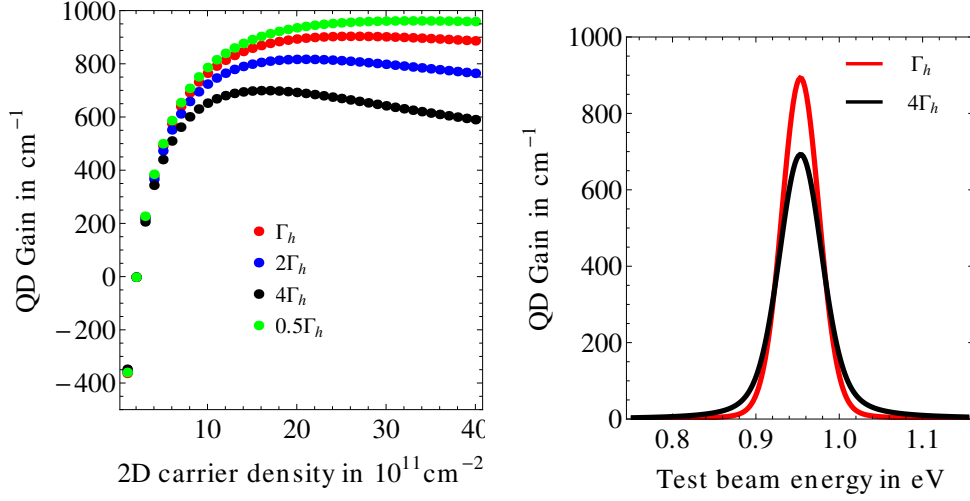


Figure 5.6.: *left*: Maximal QD gain with a homogeneous broadening of Γ_h , $2\Gamma_h$, $4\Gamma_h$ and $0.5\Gamma_h$. *right*: Gain spectra for a 2D carrier density of $20 \times 10^{11} \text{cm}^{-2}$, Gaussian shaped inhomogeneous broadening of $\gamma_{\text{inh}} = 50 \text{meV}$ FWHM and a homogeneous broadening of about $\Gamma_h = 2.6 \text{meV}$ and $\Gamma_h = 10.3 \text{meV}$

that changing Γ_h by a factor of 8 causes a change in the maximal gain of about 40% in the high-density regime. In the regime up to 2D carrier densities of $6 \times 10^{11} \text{cm}^{-2}$, the difference in the maximal gain is almost negligible. The gain spectra in Fig. 5.6(*right*) do not reveal pronounced differences either.

5.4. Discussion

The model for the dephasing time reproduces the basic behavior of the homogeneous broadening. A better agreement with the experiment could be achieved by the incorporation of additional effects. For example, Nilsson et al. found in [21] a better agreement to the experiment of [61] with the use of a quasi-static plasmon pole approximation, instead of the static screening used here. Furthermore, phonon scattering appeared to be significant, both in theory [24] and experiment [61], even in the high-density regime. The use of QD occupation probabilities determined via a rate equation model, or the inclusion of Hartree-Fock energy renormalizations would not cause any fundamental problems. The inclusion of couplings to further polarizations is also possible in a Markovian treatment. This is different for phonon scattering and the extension to multi-level QDs. Lorke et al. emphasize the importance of a self-consistent treatment of Coulomb and phonon scattering. This implies a non-Markovian treatment to account for energy renormalizations beyond the Hartree-Fock limit. On the side of Coulomb scattering this enables the inclusion of intra-dot scattering channels; on the side of the phonon interaction the broadening devolves into effects like the phonon bottleneck. Nevertheless, those two extensions can also be approximated by a description in the limit of the Born-Markov

5. A microscopic gain model

approximation [40, 21].

The moderate qualitative agreement with the benchmark model of Lorke et al., has to be put in relation to the usual variations in the value of d_{vc} , that appear in Eq. (5.1) as input parameter: Eliseev et al. [103] determined the d_{vc} via fits onto experimental data for InAs dots in a well structures. They reported deviations of 7% from an average value $d_{vc} = 0.6 e_0$ nm. This would cause a deviation of nearly 15% in $|d_{vc}|^2$. Values for the dipole–matrix elements of various wafers vary between $0.54 e_0$ nm and $0.66 e_0$ nm. So the difference between the lowest and the highest value is about 20% leading to an uncertainty of about 40% for the maximum value of the gain. Chow et al. used tight binding calculations to determine the dipole matrix elements. For the ground state transition in InAs dots in a well structure, they found a value of $0.24 e_0$ nm. Compared to the value of $0.6 e_0$ nm of Eliseev et al., this causes a difference in the maximum gain by a factor of 6.25.

As a result, the lower accuracy of the gain model presented here, compared to the benchmark model of Lorke et al., might be masked by the uncertainty of the input parameter d_{vc} .

The model presented here offers a good compromise between accuracy and effort. In the end, the desired accuracy, for example in a dynamic simulation, dictates whether the model presented here is appropriate.

A. Details of the orthogonalized plane waves

Because it is necessary for several calculations, the orthogonality of the OPWs will be presented here. Basically the following calculations is taken from Ref. [20]. However, there the orthogonality of the wavefunctions was shown for the in-plane part of the envelope, whereas here, the full 3D envelope is considered. .

A.1. Orthogonalized plane waves for the bulk states standardly used

The starting point are wavefunctions of the form

$$\psi_D(\vec{r}) = \hat{\psi}_D(\vec{r})u_{\Lambda_l}(\vec{r}),$$

for QD states, and

$$\psi_{\mathbf{k}}(\vec{r}) = \hat{\psi}_{\vec{k}}(\vec{r})u_{\Lambda}(\vec{r}).$$

for reservoir states. In one of the following steps it will be used that the QD position is a quantum number, included in D . Therefore it should be reminded that

$$\hat{\psi}_D(\vec{r}) = \hat{\psi}_{(\Lambda_D, \sigma_D, \dots, \vec{R}_D)}(\vec{r}) = \hat{\psi}_{(\Lambda_D, \sigma_D, \dots, 0)}(\vec{\rho}), \text{ with } \vec{\rho} = \vec{r} - \vec{R}_D. \quad (\text{A.1})$$

The following abbreviation will be used, to shorten the notation: $(D, \vec{R}_D) := (\Lambda_D, \sigma_D, \dots, \vec{R}_D)$. By assuming wavefunctions for the same band / carrier type, the discussion can be restricted to the envelope. Nielsen et al. suggested OPWs in the form

$$|\psi_{\mathbf{k}, 3DCR}\rangle = \frac{1}{N_{\mathbf{k}, 3D}} \left(|\psi_{\mathbf{k}, 3D}^0\rangle - \sum_l \langle \psi_l | \psi_{\mathbf{k}, 3D}^0 \rangle |\psi_l\rangle \right) =: |\psi_{\mathbf{k}, 3DCR}\rangle \quad (\text{A.2})$$

with $\langle \vec{r} | \psi_{\mathbf{k}, 3D}^0 \rangle = \frac{1}{\sqrt{AL}} e^{i\vec{k}\cdot\vec{r}}$ and $N_{\mathbf{k}, 3D}$ is a normalization factor which will be derived in below. The first two things to be presented are

1. $\langle \psi_D | \psi_{\mathbf{k}, 3DCR} \rangle = 0,$
2. $\langle \psi_{\mathbf{k}_1, 3DCR} | \psi_{\mathbf{k}', 3DCR} \rangle = 0.$

A. Details of the orthogonalized plane waves

1. $\langle \psi_D | \psi_{\mathbf{k},3DCR} \rangle = 0$

$$\begin{aligned}
\langle \psi_{\text{QD}} | \psi_{\mathbf{k},3DCR} \rangle &= \langle \psi_D | \frac{1}{N_{\mathbf{k},3D}} \left(|\psi_{\mathbf{k},3D}^0\rangle - \sum_{n \in \text{QD}} \langle \psi_n | \psi_{\mathbf{k},3D}^0 \rangle | \psi_n \rangle \right) \\
&= \frac{1}{N_{\mathbf{k},3D}} \left(\langle \psi_D | \psi_{\mathbf{k},3D}^0 \rangle - \sum_{n \in \text{QD}} \langle \psi_n | \psi_{\mathbf{k},3D}^0 \rangle \underbrace{\langle \psi_D | \psi_n \rangle}_{\delta_{n,D}} \right) \\
&= \frac{1}{N_{\mathbf{k},3D}} \left(\langle \psi_D | \psi_{\mathbf{k},3D}^0 \rangle - \langle \psi_D | \psi_{\mathbf{k},3D}^0 \rangle \right) \\
&= 0 \text{ q.e.d. } .
\end{aligned} \tag{A.3}$$

2. $\langle \psi_{\mathbf{k}_1,3DCR} | \psi_{\mathbf{k}_2,3DCR} \rangle = 0$

$$\begin{aligned}
&\langle \psi_{\mathbf{k}_1,3DCR} | \psi_{\mathbf{k}_2,3DCR} \rangle \\
&= \frac{1}{N_{\mathbf{k}_1,3D}} \left(\langle \psi_{\mathbf{k}_1,3D}^0 | - \sum_{n \in \text{QD}} \langle \psi_{\mathbf{k}_1,3D}^0 | \psi_n \rangle \langle \psi_n | \right) \\
&\quad \times \frac{1}{N_{\mathbf{k}_2,3D}} \left(|\psi_{\mathbf{k}_2,3D}^0\rangle - \sum_{m \in \text{QD}} \langle \psi_m | \psi_{\mathbf{k}_2,3D}^0 \rangle | \psi_m \rangle \right) \\
&= \frac{1}{N_{\mathbf{k}_1,3D} N_{\mathbf{k}_2,3D}} \left(\langle \psi_{\mathbf{k}_1,3D}^0 | \psi_{\mathbf{k}_2,3D}^0 \rangle \right. \\
&\quad - \sum_{m \in \text{QD}} \langle \psi_m | \psi_{\mathbf{k}_2,3D}^0 \rangle \langle \psi_{\mathbf{k}_1,3D}^0 | \psi_m \rangle - \sum_{n \in \text{QD}} \langle \psi_{\mathbf{k}_1,3D}^0 | \psi_n \rangle \langle \psi_n | \psi_{\mathbf{k}_2,3D}^0 \rangle \\
&\quad \left. + \sum_{n,m \in \text{QD}} \langle \psi_{\mathbf{k}_1,3D}^0 | \psi_n \rangle \langle \psi_m | \psi_{\mathbf{k}_2,3D}^0 \rangle \langle \psi_n | \psi_m \rangle \right)
\end{aligned} \tag{A.4}$$

Using the orthogonality of the plane waves and

$$\begin{aligned}
\langle \psi_{\text{QD}} | \psi_{\mathbf{k},3D}^0 \rangle &= \int d^3 r \psi_D^*(\vec{r}) \psi_{\mathbf{k},3D}^0(\vec{r}) \\
&= \int d^3 r \psi_{(D,\vec{R}_D=0)}^*(\vec{r} - \vec{R}) \frac{1}{\sqrt{AL}} e^{i\vec{k} \cdot \vec{r}} \\
&\stackrel{\vec{\rho} = \vec{r} - \vec{R}}{=} \int d^3 \rho \psi_{(D,\vec{R}_D=0)}^*(\vec{\rho}) \frac{1}{\sqrt{AL}} e^{i\vec{k} \cdot (\vec{\rho} + \vec{R})} \\
&= e^{i\vec{k} \cdot \vec{R}} \int d^3 \rho \psi_{(D,\vec{R}=0)}^*(\vec{\rho}) \frac{1}{\sqrt{AL}} e^{i\vec{k} \cdot \vec{\rho}},
\end{aligned} \tag{A.5}$$

A.1. Orthogonalized plane waves for the bulk states standardly used

one arrives at

$$\begin{aligned}
\langle \psi_{\mathbf{k}_1,3D} | \psi_{\mathbf{k},3D2} \rangle &= \frac{1}{N_{\mathbf{k}_1,3D} N_{\mathbf{k}_2,3D}} \left(\delta_{\vec{k}_1, \vec{k}_2} \right. \\
&\quad - \sum_{m \in \text{QD}} e^{i(\vec{k}_2 - \vec{k}_1) \cdot \vec{R}_m} \langle \psi_{m, \vec{R}_m=0} | \psi_{\vec{k}_2, 3D}^0 \rangle \langle \psi_{\vec{k}_1}^0 | \psi_{m, \vec{R}_m=0} \rangle \\
&\quad - \sum_{n \in \text{QD}} e^{i(\vec{k}_2 - \vec{k}_1) \cdot \vec{R}_n} \langle \psi_{\vec{k}_1}^0 | \psi_{n, \vec{R}_n=0} \rangle \langle \psi_{n, \vec{R}_n=0} | \psi_{\vec{k}_2}^0 \rangle \\
&\quad + \sum_{n, m \in \text{QD}} e^{-i\vec{k}_1 \cdot \vec{R}_n} e^{i\vec{k}_2 \cdot \vec{R}_m} \langle \psi_{\vec{k}_1, 3D}^0 | \psi_{n, \vec{R}_n=0} \rangle \langle \psi_{m, 0} | \psi_{\vec{k}_2, 3D}^0 \rangle \underbrace{\langle \psi_n | \psi_m \rangle}_{= \delta_{m,n}} \Big) \\
&= \frac{1}{N_{\mathbf{k}_1,3D} N_{\mathbf{k}_2,3D}} \\
&\quad \times \left(\delta_{\vec{k}_1, \vec{k}_2} - \sum_{m \in \text{QD}} e^{i(\vec{k}_2 - \vec{k}_1) \cdot \vec{R}_m} \langle \psi_{m, \vec{R}_m=0} | \psi_{\vec{k}_2, 3D}^0 \rangle \langle \psi_{\vec{k}_1, 3D}^0 | \psi_{m, \vec{R}_m=0} \rangle \right). \tag{A.6}
\end{aligned}$$

Since the QD position does not enter into $\langle \psi_{\mathbf{k}_1,3D}^0 | \psi_{m, \vec{R}_m=0} \rangle$, the sum over all QD positions can be evaluated. Therefore, one assumes randomly distributed QDs. So for a high number N_{QD} of QDs it is appropriate to assume

$$\frac{1}{N_{QD}} \sum_m^{N_{QD}} e^{i(\vec{k}_2 - \vec{k}_1) \cdot \vec{R}_m} = \delta_{\vec{k}_2, \vec{k}_1}. \tag{A.7}$$

The latter “=” fits to a thermodynamic limit, where $N_{QD} \rightarrow \infty$, for $AL \rightarrow \infty$, for $\frac{N_{QD}}{AL} = \text{const.}$. Since Eq. (A.7) holds for any realistic distribution of the QDs, it is not restrictive to assume

$$\frac{1}{N_{QD}} \sum_m^{N_{QD}} e^{i(\vec{k}_2 - \vec{k}_1) \cdot \vec{R}_m} = \frac{1}{N_{QD}/N_{2D}} \sum_m^{N_{QD}/N_{2D}} e^{i(\vec{k}_{||,2} - \vec{k}_{||,1}) \cdot \vec{R}_{||,m}} \frac{1}{N_{2D}} \sum_n^{N_{2D}} e^{i(k_{z,2} - k_{z,1}) R_{z,n}}, \tag{A.8}$$

where N_{2D} denotes the number of QD layers and $x_{||,}$ ($x_{z,}$) denotes the in-plane- / z-component of the respective quantities. In a realistic device, the approximation Eq. (A.7) fits very well for the in-plane direction of a single QD layer. There are about 10000 randomly distributed QDs per layer, and so the phase factors cancel each other out, except for $\vec{k}_{||,2} = \vec{k}_{||,1}$. This differs for the z-direction, where one typically has 5–25 layers with close to equal spacing. As a result, the phase factors would no longer cancel each other out and the Kronecker- δ would not appear for the z-component of the wavevector. However, one could argue that, due to size fluctuations of the QDs, terrace formations, corrugations of the GaAs, and growth stacking failures, the z-coordinates of the QD’s center varies (cf. Refs. [7, 104]). As a consequence, the number of different phase factor increases and the approximation improves. It improves even further by assuming a device with a very large number of QD layers, but equal layer density.

A. Details of the orthogonalized plane waves

This assumption might not fit the situation in a realistic device. Nevertheless it seems appropriate a comparison between the scattering rates of 2D-QD and a 3D-QD sample. In this thesis, it is assumed that Eq. (A.7) also holds for the z-component of the \vec{k} -vector and not only for the in-plane component. This is a common assumption in QW systems [105]. Furthermore, a comparison of different OPW approaches in Sec. 4.3.10 suggests that Eq. (A.7) is also an appropriate assumption for the systems considered here. So assuming Eq. (A.7) holds in 3D, Eq. (A.6) becomes

$$\langle \psi_{\mathbf{k}_1,3D} | \psi_{\mathbf{k}_2,3D} \rangle = \delta_{\vec{k}_1, \vec{k}_2} \frac{1}{N_{\mathbf{k}_1,3D} N_{\mathbf{k}_2,3D}} \left(1 - \sum_{m \in \text{QD}} \langle \psi_{m, \vec{R}_m=0} | \psi_{\vec{k}_2}^0 \rangle \langle \psi_{\mathbf{k}_1,3D}^0 | \psi_{m, \vec{R}_m=0} \rangle \right). \quad (\text{A.9})$$

Defining the normalization factor $N(\vec{k}_1)$ as .

$$N_{\mathbf{k},3D} = \sqrt{1 - \sum_l |\langle \psi_l | \psi_{\mathbf{k},3D}^0 \rangle|^2}, \quad (\text{A.10})$$

one has the desired ortho-normal basis in the reservoir subspace, which is orthogonal to the QD states.

A short overview of the Coulomb-integrals can be found in App. B and more detailed in the Refs. [46] (in-plane part), [51, 52] (z-direction 3D) and [2] (z-direction 2D).

A.2. Additional possible orthogonalized plane waves.

At the end of Sec. 2.4.2 additional possible OPW basis sets were presented. The main idea behind these basis sets is to keep the factorizability of the 3D wavefunction, such as is the case for QD wavefunction:

$$\psi_{\text{QD}_l}(\vec{r}) = \xi_l(z) \varphi_{\text{QD}_l}(\vec{r}_{||}) u_{\Lambda_l, \sigma_l}(\vec{r}), \quad (\text{A.11})$$

$$\psi_{\mathbf{k}_m}^{\text{new}}(\vec{r}) = \phi_{k_z}^{\text{new}}(z) \varphi_{k_{||}}^{\text{new}}(\vec{r}_{||}) u_{\Lambda_m, \sigma_m}(\vec{r}). \quad (\text{A.12})$$

Now it becomes easy to prove that

$$\langle \psi_{\mathbf{k}}^{\text{new}} | \psi_{\text{QD}} \rangle = 0,$$

if

$$\langle \varphi_{k_{||}}^{\text{new}} | \varphi_{\text{QD}} \rangle = 0, \text{ or } \langle \phi_{k_z}^{\text{new}} | \xi \rangle = 0.$$

The “new” states are the in-plane or z-OPWs, which are constructed based on the Nielsen scheme [20]:

$$|\varphi_{k_{||}}^{\text{new}}\rangle := \frac{1}{N_{2D}(k_{||})} \left(|\varphi_{k_{||}}^0\rangle - \sum_{\substack{v \in \text{QD} \\ \Lambda_v = \Lambda_k, \sigma_v = \sigma_k}} \langle \varphi_v | \varphi_{k_{||}}^0 \rangle |\varphi_v\rangle \right), \quad (\text{A.13})$$

A.2. Additional possible orthogonalized plane waves.

and

$$|\phi_{k_z}\rangle := \frac{1}{N_z(k_z)} \left(|\phi_{k_z}^0\rangle - \sum_{\text{QD layer } l}^{N_{2D}} \langle \xi_l | \phi_{k_z}^0 \rangle |\xi_l\rangle \right), \quad (\text{A.14})$$

with $\langle \vec{r}_{||} | \phi_{k_{||}}^0 \rangle = \frac{1}{\sqrt{A}} e^{i\vec{k}_{||} \cdot \vec{r}_{||}}$, $\langle z | \phi_{k_z}^0 \rangle = \frac{1}{\sqrt{L}} e^{ik_z z}$ and normalization factors of the form

$$N_{2D}(\vec{k}_{||}) = \sqrt{1 - \sum_{\substack{v \in \text{QD} \\ \Lambda_v = \Lambda_k, \sigma_v = \sigma_k}} |\langle \varphi_v | \varphi_{k_{||}}^0 \rangle|^2}, \quad (\text{A.15})$$

for the in-plane wavefunctions, respective

$$N_z(k_z) = \sqrt{1 - \sum_{\text{QD layer } l}^{N_{2D}} |\langle \xi_l | \varphi_{k_z}^0 \rangle|^2}, \quad (\text{A.16})$$

for growth direction. Note that the band- and spin-indices are fixed in the sum over all QD states v in the 2D reservoir. The orthogonality of these OPWs with respect to other reservoir states can be shown in the same way as in the previous section for the 3D-OPW. For the in-plane OPW, this can be found in Ref. [20]. However, the difficulties arising from the small number of layers are the same as they were in the 3D case, leading an assumption of a high number of QD layers.

Further possible eigenbases for the reservoir subspace are:

1. the QD in-plane wavefunctions,

$$|\psi_{\mathbf{k},2\text{DOPW}}\rangle = \frac{1}{N_{2D}(\vec{k}_{||})} \left(|\varphi_{k_{||}}^0\rangle - \sum_{\substack{v \in \text{QD} \\ \Lambda_v = \Lambda_k, \sigma_v = \sigma_k}} \langle \varphi_v | \varphi_{k_{||}}^0 \rangle |\varphi_v\rangle \right) |\phi_{k_z}^0\rangle |u_{(\Lambda_k, \sigma_k)}\rangle, \quad (\text{A.17})$$

2. the z-direction,

$$|\psi_{\mathbf{k},z\text{OPW}}\rangle = \frac{1}{N_z(k_z)} |\varphi_{k_{||}}^0\rangle \left(|\phi_{k_z}^0\rangle - \sum_{\text{QD layer } l}^{N_{2D}} \langle \xi_l | \phi_{k_z}^0 \rangle |\xi_l\rangle \right) |u_{(\Lambda_k, \sigma_k)}\rangle, \quad (\text{A.18})$$

3. the in plane and z-direction separately¹:

$$\begin{aligned} |\psi_{\mathbf{k},2\text{D} \times z\text{OPW}}\rangle &= \frac{1}{N_{2D}(\vec{k}_{||})N_z(k_z)} \left(|\varphi_{k_{||}}^0\rangle - \sum_{\substack{v \in \text{QD} \\ \Lambda_v = \Lambda_k, \sigma_v = \sigma_k}} \langle \varphi_v | \varphi_{k_{||}}^0 \rangle |\varphi_v\rangle \right) \\ &\quad \times \left(|\phi_{k_z}^0\rangle - \sum_{\text{QD layer } l}^{N_{2D}} \langle \xi_l | \phi_{k_z}^0 \rangle |\xi_l\rangle \right) |u_{(\Lambda_k, \sigma_k)}\rangle. \end{aligned} \quad (\text{A.19})$$

¹This basis has been chosen in Ref. [49]

A. Details of the orthogonalized plane waves

Due to the relations

$$\langle \psi_{2\text{DOPW}} | \psi_{\text{QD}} \rangle = \langle \phi_{k_z}^0 | \chi \rangle \underbrace{\langle \phi_{k_{\parallel}}^{\vec{r}} | \varphi_{\text{QD}} \rangle}_{=0} = 0, \quad (\text{A.20})$$

$$\langle \psi_{2\text{DOPW-zOPW}} | \psi_{\text{QD}} \rangle = \underbrace{\langle \phi_{k_z} | \chi \rangle}_{=0} \underbrace{\langle \varphi_{k_{\parallel}}^{\vec{r}} | \varphi_{\text{QD}} \rangle}_{=0} = 0, \quad (\text{A.21})$$

$$\langle \psi_{\text{zDOPW}} | \psi_{\text{QD}} \rangle = \underbrace{\langle \phi_{k_z} | \chi \rangle}_{=0} \langle \phi_{k_{\parallel}}^0 | \varphi_{\text{QD}} \rangle = 0, \quad (\text{A.22})$$

all basis vectors are orthogonal to the QD states. due to the relations $\langle \phi_{\vec{k}_{\parallel}}^{\vec{r}} | \phi_{\vec{k}'_{\parallel}}^{\vec{r}} \rangle = \langle \phi_{\vec{k}_{\parallel}}^0 | \phi_{\vec{k}'_{\parallel}}^0 \rangle = \delta_{\vec{k}_{\parallel}, \vec{k}'_{\parallel}}$ and $\langle \phi_{k_z} | \phi_{k'_z} \rangle = \langle \phi_{k_z}^0 | \phi_{k'_z}^0 \rangle = \delta_{k_z, k'_z}$ the vectors also form an ortho-normal basis in the reservoir subspace.

B. Coulomb integrals

In-plane-overlap integrals

In this chapter, an overview of the Coulomb-overlap integrals will be given. These integrals are the ingredients of the matrix elements.

A detailed catalog of all possible in-plane overlap integrals and their calculation can be found in Ref. [46].

As in Refs. [20, 46], the overlap of different QDs is neglected. Therefore, it is assumed that the QD states entering the matrix elements belong to the same QD at the position $\vec{R} = (\vec{R}_{||}, R_z)$.

The basic in-plane integrals are:

$$\langle \varphi_{\text{GS}}^\Lambda | e^{i\vec{q}_{||} \cdot \vec{r}_{||}} | \varphi_{\vec{k}_{||}}^0 \rangle = \frac{1}{\sqrt{A}} 2\sqrt{\pi} \sqrt{\frac{\hbar}{2m_\Lambda \omega_{\text{QD}}^\Lambda}} e^{-\frac{\hbar}{2m_\Lambda \omega_{\text{QD}}^\Lambda} (\vec{k}_{||} + \vec{q}_{||})_{||}^2} e^{i(\vec{k}_{||} + \vec{q}_{||}) \cdot \vec{R}_{||}}, \quad (\text{B.1})$$

$$\langle \varphi_{\text{ES},\pm}^\Lambda | e^{i\vec{q}_{||} \cdot \vec{r}_{||}} | \varphi_{\vec{k}_{||}}^0 \rangle = i \frac{1}{\sqrt{A}} 2\sqrt{\pi} e^{-\frac{\hbar}{2m_\Lambda \omega_{\text{QD}}^\Lambda} (\vec{k}_{||} + \vec{q}_{||})_{||}^2} e^{\pm i\alpha_{\vec{k}_{||} + \vec{q}_{||}}} e^{i(\vec{k}_{||} + \vec{q}_{||}) \cdot \vec{R}_{||}}, \quad (\text{B.2})$$

$$\langle \varphi_{\text{GS}}^\Lambda | e^{i\vec{q}_{||} \cdot \vec{r}_{||}} | \varphi_{\text{GS}}^\Lambda \rangle = e^{-\frac{\hbar}{4m_\Lambda \omega_{\text{QD}}^\Lambda} q_{||}^2} e^{i\vec{q}_{||} \cdot \vec{R}_{||}}, \quad (\text{B.3})$$

$$\langle \varphi_{\text{GS}}^\Lambda | e^{i\vec{q}_{||} \cdot \vec{r}_{||}} | \varphi_{\text{ES},\pm}^\Lambda \rangle = \frac{1}{2} i \sqrt{\frac{\hbar}{m_\Lambda \omega_{\text{QD}}^\Lambda}} e^{-\frac{\hbar}{4m_\Lambda \omega_{\text{QD}}^\Lambda} q_{||}^2} q_{||} e^{\pm i\alpha_{\vec{q}_{||}}} e^{i(\vec{q}_{||}) \cdot \vec{R}_{||}}, \quad (\text{B.4})$$

$$\langle \varphi_{\text{ES},\pm}^\Lambda | e^{i\vec{q}_{||} \cdot \vec{r}_{||}} | \varphi_{\text{ES},\pm}^\Lambda \rangle = \frac{1}{4} \frac{\hbar}{m_\Lambda \omega_{\text{QD}}^\Lambda} e^{-\frac{\hbar}{4m_\Lambda \omega_{\text{QD}}^\Lambda} q_{||}^2} \left(4 \frac{m_\Lambda \omega_{\text{QD}}^\Lambda}{\hbar} - q_{||}^2 \right) e^{i\vec{q}_{||} \cdot \vec{R}_{||}}, \quad (\text{B.5})$$

$$\langle \varphi_{\text{ES},\pm}^\Lambda | e^{i\vec{q}_{||} \cdot \vec{r}_{||}} | \varphi_{\text{ES},\mp}^\Lambda \rangle = -\frac{1}{4} \frac{\hbar}{m_\Lambda \omega_{\text{QD}}^\Lambda} e^{-\frac{\hbar}{4m_\Lambda \omega_{\text{QD}}^\Lambda} q_{||}^2} q_{||}^2 e^{-i2\alpha_{\vec{q}_{||}}} e^{i\vec{q}_{||} \cdot \vec{R}_{||}}. \quad (\text{B.6})$$

$\alpha_{\vec{x}_{||}}$ denotes the angle between an in-plane wavevector $\vec{x}_{||}$ and the QD axis. The additional terms that appear can be constructed by complex conjugation and / or vector substitutions, for example, $\vec{q}_{||} \rightarrow -\vec{q}_{||}$. Note that $\alpha_{-\vec{q}_{||}} = \alpha_{\vec{q}_{||}} + \pi$ and therefore $e^{i\alpha_{-\vec{q}_{||}}} = -e^{i\alpha_{\vec{q}_{||}}}$. Details of calculations for the GS reservoir overlap integral can be found in Ref. [2]. Calculations for the other integrals is similar.

All overlap integrals contain a factor of the form $e^{-x K_{||}^2}$. This factor strongly reduces the scattering efficiency for increasing momentum (transfer) $K_{||}$.

B. Coulomb integrals

z-overlap integrals

The z-overlap integrals for the 2D reservoir are

$$\langle \xi_a | \langle \xi_b | e^{-q_{||}|z-z'|} | \xi_c \rangle | \xi_d \rangle = \int_{-L/2}^{L/2} dz \int_{-L/2}^{L/2} dz' \xi_a^*(z) \xi_b^*(z') e^{-q_{||}|z-z'|} \xi_c(z') \xi_d(z) \quad (\text{B.7})$$

$$= \frac{2}{Lq} + \frac{1}{Lq + \frac{4\pi^2}{Lq}} - \frac{2}{L^6} (1 - e^{-Lq}) \left(\frac{4\pi^2}{q(q^2 + \frac{4\pi^2}{L^2})} \right)^2. \quad (\text{B.8})$$

Details of the calculation of the overlap integral can be found in Ref. [2].

In the 3D Coulomb matrix, elements enter z-overlap integrals of the form

$$\langle \xi | e^{\pm i q_z z} | \xi \rangle = \frac{8\pi^2 \sin\left(\frac{Lq_z}{2}\right)}{Lq_z (4\pi^2 - L^2q_z^2)} e^{i\pm q_z R_z}, \quad (\text{B.9})$$

and

$$\langle \xi_a | e^{\pm i q_z z} | \phi_{k_z}^0 \rangle = \frac{1}{\sqrt{L_z}} \frac{2\sqrt{2L} \pi \cos\left(\frac{L(k_z \pm q_z)}{2}\right)}{\pi^2 - L^2(k_z \pm q_z)^2} e^{i(k_z \pm q_z) R_z}. \quad (\text{B.10})$$

Details of the calculation of the overlap integral can be found in Refs. [51, 52].

Phase-factors $e^{i\vec{q}\cdot\vec{R}}$ reflect the QD position, cf. Appx. (A.5). For further evaluation, these phase factors are important to assuring the orthogonality of the QD wavefunctions, or to incorporating spatial inhomogeneities, cf. App. A.1 and Sec. 3.3.2. However in some matrix elements the phase factors just cancel each other out, since the Coulomb matrix elements enter the scattering rates in second order. Hence, in the case of a spatially homogeneous system under consideration, the scattering rates are not dependent on QD position.

As the QD wavefunctions and so the Coulomb integrals are given in cylindrical coordinates, the sum over all reservoir states becomes

$$\sum_{\vec{k}} \rightarrow \frac{AL}{(2\pi)^3} \int_{\text{BZ}} d^3k = \frac{AL}{(2\pi)^3} \int_0^{2\pi} d\alpha_k \int_{-k_z}^{k_z} dk_z \int_0^{k_{||}} dk_{||} k_{||}. \quad (\text{B.11})$$

Here BZ denotes the volume of the Brillouin-zone and k_z and $k_{||}$ are the maximal absolute values of the wavevector in z- and in-plane direction within the Brillouin-zone. In practice the integration boardsers can be restricted via the fast decay of the Fermi-distributions and as a result of that, the maximal significant energy and momentum transfer. The angle α_k is the angle of the in-plane wavevector to the QD in-plane axis. For the QD-GS this axis can be chosen arbitrary, whereas for the QD-ES it is defined via the wavefunction, cf. Eqs. (2.14) and (2.15).

C. Derivation Screening

If a test charge is surrounded by other carriers, it does not “see” the full Coulomb potential of all carriers, but rather a reduced one. The Coulomb potential of carriers further away from the test charge is screened by the carriers that are between them.

An established method to describe screening in semiconductor materials is the so called Lindhard formula ([39, 106]). A detailed discussion of screening and the Lindhard formula can be found in chapter 8 of Ref. [39], which is the basis for the following sketch of the derivation.

For the devices considered here, the problem arises of considering subsystems of different dimensionality. For this reason, the derivation of the Lindhard formula, as shown in Refs. [39, 68, 2, 51], will be sketched to find a way to describe screening in structures of different dimensionality. To keep the notation as general as possible compound indices will be defined as $\mathbf{k} = (\vec{k}, \sigma_k, \Lambda_k)$ and the notation $\mathbf{k} = (\vec{k}, \sigma_k, \lambda_k)$. Furthermore the notation $\mathbf{k} \pm \mathbf{x} = (\vec{k} \pm \vec{x}, \sigma_k = \sigma_x, \Lambda_k = \Lambda_x)$ will be used. The starting point is the dynamics of the operator

$$\langle a_{\mathbf{k}-\mathbf{q}}^\dagger a_{\mathbf{k}} \rangle, \quad (\text{C.1})$$

which is connected to the charge density operator

$$\langle \rho_{\vec{q}}^{\Lambda_q} \rangle = -\frac{|e_0|}{AL} \sum_{\vec{k}, \sigma_k} \langle a_{\mathbf{k}-\mathbf{q}}^\dagger a_{\mathbf{k}} \rangle. \quad (\text{C.2})$$

The operator of the total charge is then given by

$$\langle \rho_{\vec{q}} \rangle = -\frac{|e_0|}{AL} \sum_{\vec{k}, \sigma_k} \langle a_{(\vec{k}-\vec{q}, \sigma_k, c)}^\dagger a_{(\vec{k}, \sigma_k, c)} \rangle + \frac{|e_0|}{AL} \sum_{\vec{k}, \sigma_k} \langle d_{(\vec{k}+\vec{q}, \sigma_k, h)}^\dagger d_{(\vec{k}, \sigma_k, h)} \rangle, \quad (\text{C.3})$$

where $d_{(\vec{k}+\vec{q}, \sigma_k, h)}^\dagger / d_{(\vec{k}, \sigma_k, h)}$ denote the hole creation / annihilation operators, which can be defined as [39] $a_{(\vec{k}, \sigma_k, v)} = d_{(-\vec{k}, -\sigma_k, h)}^\dagger$ and $a_{(\vec{k}, \sigma_k, v)}^\dagger = d_{(-\vec{k}, -\sigma_k, h)}$. Here, a fluctuation in spatially homogeneous charge density will be considered, leading to inhomogeneity, so that

$$\langle \rho_{\vec{q}} \rangle \neq 0, \text{ for } \vec{q} \neq 0. \quad (\text{C.4})$$

C. Derivation Screening

To simplify the notation, Eq. (C.3) can be rewritten as

$$\begin{aligned}
\langle \rho_{\vec{q}} \rangle &= -\frac{|e_0|}{AL} \sum_{\vec{k}, \sigma_k} \langle a_{(\vec{k}-\vec{q}, \sigma_k, c)}^\dagger a_{(\vec{k}, \sigma_k, c)} \rangle + \frac{|e_0|}{AL} \sum_{\vec{k}, \sigma_k} \langle d_{(\vec{k}+\vec{q}, \sigma_k, h)}^\dagger d_{(\vec{k}, \sigma_k, h)} \rangle \\
&= -\frac{|e_0|}{AL} \sum_{\vec{k}, \sigma_k} \langle a_{(\vec{k}-\vec{q}, \sigma_k, c)}^\dagger a_{(\vec{k}, \sigma_k, c)} \rangle + \frac{|e_0|}{AL} \sum_{\vec{k}, \sigma_k} \langle a_{(-(\vec{k}+\vec{q}), \sigma_k, v)}^\dagger a_{(-\vec{k}, \sigma_k, v)} \rangle \\
&\stackrel{\vec{K} = -(\vec{k}+\vec{q})}{=} -\frac{|e_0|}{AL} \sum_{\vec{k}, \sigma_k} \langle a_{(\vec{k}-\vec{q}, \sigma_k, c)}^\dagger a_{(\vec{k}, \sigma_k, c)} \rangle - \frac{|e_0|}{AL} \sum_{\vec{k}, \sigma_k} \langle a_{(\vec{K}-\vec{q}, \sigma_k, v)}^\dagger a_{(\vec{K}, \sigma_k, v)} \rangle \\
&= -\frac{|e_0|}{AL} \sum_{\vec{k}, \sigma_k, \Lambda_k} \langle a_{(\vec{k}-\vec{q}, \sigma_k, \Lambda_k)}^\dagger a_{(\vec{k}, \sigma_k, \Lambda_k)} \rangle. \tag{C.5}
\end{aligned}$$

The fluctuation causes an induced field, so that a test charge sees the potential

$$V_{\text{eff}} = V(\vec{r}) + V_{\text{induced}}(\vec{r}) \tag{C.6}$$

The dynamics of the fluctuation can be determined via the Heisenberg EOM of the operator $\langle a_{\vec{k}-\vec{q}}^\dagger a_{\vec{k}} \rangle$. Assuming a Hamiltonian in the form of

$$H = H_{0,\text{el}} + H_{V_{\text{eff}}} \tag{C.7}$$

$$= \sum_{\mathbf{k}} \epsilon_{\mathbf{k}} a_{\mathbf{k}}^\dagger a_{\mathbf{k}} + \sum_{\mathbf{p}} V_{\text{eff}}(p) \sum_{\mathbf{k}} a_{\mathbf{k}+\mathbf{p}}^\dagger a_{\mathbf{k}}, \tag{C.8}$$

with the abbreviations $f_{\mathbf{x}} = \langle a_{\mathbf{x}}^\dagger a_{\mathbf{x}} \rangle$ and a random phase approximation [39], the EOM has the form

$$\frac{d}{dt} \langle a_{\mathbf{k}-\mathbf{q}}^\dagger a_{\mathbf{k}} \rangle = \frac{i}{\hbar} (\epsilon_{\mathbf{k}-\mathbf{q}} - \epsilon_{\mathbf{k}}) \langle a_{\mathbf{k}-\mathbf{q}}^\dagger a_{\mathbf{k}} \rangle - \frac{i}{\hbar} V_{\text{eff}}(q) (f_{\mathbf{k}-\mathbf{q}} - f_{\mathbf{k}}) \tag{C.9}$$

Solving the EOM via Fourier transformation, and introducing the damping $e^{-\gamma t}$ leads to

$$\langle a_{\vec{k}-\vec{q}}^\dagger a_{\vec{k}} \rangle = V_{\text{eff}}(q) \frac{f_{\mathbf{k}-\mathbf{q}} - f_{\mathbf{k}}}{\epsilon_{\mathbf{k}-\mathbf{q}} - \epsilon_{\mathbf{k}} + \omega + i\gamma} \tag{C.10}$$

and the charge density operator

$$\langle \rho_{\vec{q}} \rangle = -\frac{|e_0|}{AL} V_{\text{eff}}(q) \sum_{\mathbf{k}} \frac{f_{\mathbf{k}-\mathbf{q}} - f_{\mathbf{k}}}{\epsilon_{\mathbf{k}-\mathbf{q}} - \epsilon_{\mathbf{k}} + \omega + i\gamma}. \tag{C.11}$$

Now, one uses that the induced potential has to fulfill Poisson's equation, which can be

solved via Fourier transformation, yielding

$$V_{\text{induced}}(\vec{q}) = -\frac{|e_0|}{4\pi\epsilon q^2} \langle \rho_q \rangle \quad (\text{C.12})$$

$$= \frac{|e_0|}{4\pi\epsilon q^2} \frac{|e_0|}{AL} V_{\text{eff}}(q) \sum_{\mathbf{k}} \frac{f_{\mathbf{k}-\mathbf{q}} - f_{\mathbf{k}}}{\epsilon_{\vec{k}-\vec{q}} - \epsilon_{\vec{k}} + \omega + i\gamma} \quad (\text{C.13})$$

$$= V(q) V_{\text{eff}}(q) \sum_{\mathbf{k}} \frac{f_{\mathbf{k}-\mathbf{q}} - f_{\mathbf{k}}}{\epsilon_{\mathbf{k}-\mathbf{q}} - \epsilon_{\mathbf{k}} + \omega + i\gamma}. \quad (\text{C.14})$$

Finally one arrives at the Lindhard formula [68]

$$V_{\text{eff}}(q) = \frac{V(q)}{1 - V(q) \sum_{\mathbf{k}} \frac{f_{\mathbf{k}-\mathbf{q}} - f_{\mathbf{k}}}{\epsilon_{\mathbf{k}-\mathbf{q}} - \epsilon_{\mathbf{k}} + \omega + i\gamma}} \quad (\text{C.15})$$

$$= \frac{V_q}{\epsilon(q, \omega)} \quad (\text{C.16})$$

The static limit of the Lindhard is reached for $\omega + i\gamma \rightarrow 0$. For small vectors \vec{q} , one can use the approximations

$$\epsilon_{\vec{k}-\vec{q}} - \epsilon_{\vec{k}} = \frac{\hbar^2}{2m_{\Lambda}} [(k^2 + q^2 - 2\vec{k} \cdot \vec{q}) - k^2] \approx -\frac{\hbar^2}{2m_{\Lambda}} 2\vec{k} \cdot \vec{q} \quad (\text{C.17})$$

and

$$f_{\mathbf{k}-\mathbf{q}} - f_{\mathbf{k}} \approx (f_{\mathbf{k}} - \vec{q} \cdot \nabla_{\vec{k}} f_{\mathbf{k}}) - f_{\mathbf{k}} = -\sum_i q_i \frac{\partial f_{\mathbf{k}}}{\partial k_i} \quad (\text{C.18})$$

$$= -\sum_i q_i \frac{\partial f_{\mathbf{k}}}{\partial \epsilon(k)} \frac{\epsilon(k)}{\partial k_i} \quad (\text{C.19})$$

$$= \sum_i q_i \frac{\partial f_{\mathbf{k}}}{\partial \mu} \frac{\epsilon(k)}{\partial k_i} \quad (\text{C.20})$$

With the parabolic dispersion relation, assumed here, one arrives at

$$V_{\text{eff}}(q) = \frac{V(q)}{1 - V(q) \sum_{\mathbf{k}} \frac{\partial f_{\mathbf{k}}}{\partial \mu}} \quad (\text{C.21})$$

In the last step the relation $\frac{\partial f_{\vec{k}}^v}{\partial \mu_v} = \frac{\partial f_{\vec{k}}^h}{\partial \mu_h}$ was used, which can be easily proved by showing $\frac{\partial \mu_h}{\partial \mu_v} = -1 \Leftrightarrow \mu_v = -\mu_h$.

C.1. Screening in 3D

Inserting the Coulomb potential for $V_{3D}(\vec{q}) = \frac{e_0^2}{\varepsilon AL(q_{\parallel}^2 + q_z^2)}$ into Eq. (C.21) yields [51, 50]

$$\epsilon(q, 0) = 1 + \frac{\kappa_{3D}^2}{q_{\parallel}^2 + q_z^2}. \quad (\text{C.22})$$

The 3D screening wavenumber has the form

$$\kappa_{3D} = \sqrt{\frac{e_0^2}{\varepsilon AL} \sum_{\mathbf{k}} \frac{\partial f_{\mathbf{k}}}{\partial \mu}}. \quad (\text{C.23})$$

For \vec{q} vectors within the $(x, y, 0)$ -plane ($\vec{q} = (q_x, q_y, 0)$) the sum also includes WL states, so the latter equation can be written as

$$\kappa_{3D} = \sqrt{\frac{e_0^2}{\varepsilon AL} \left(\sum_{\mathbf{k} \in \text{Bulk}} \frac{\partial f_{\mathbf{k}}^{3D}}{\partial \mu_{3D}} + \sum_{\mathbf{k} \in \text{2DCR}} \frac{\partial f_{\mathbf{k}}^{2D}}{\partial \mu_{2D}} \right)} \quad (\text{C.24})$$

$$= \sqrt{\frac{e_0^2}{\varepsilon} \left(\sum_{\lambda} \frac{\partial n_{3D}^{\lambda}}{\partial \mu_{3D}^{\lambda}} + \sum_{\lambda=e,h} \frac{1}{L} \frac{\partial n_{2D}^{\lambda}}{\partial \mu_{2D}^{\lambda}} \right)}. \quad (\text{C.25})$$

In the last step the relation $\frac{\partial f_{\vec{k}}^v}{\partial \mu_v} = \frac{\partial f_{\vec{k}}^h}{\partial \mu_h}$ was used, which can be easily proved by showing $\frac{\partial \mu_h}{\partial \mu_v} = -1 \Leftrightarrow \mu_v = -\mu_h$.

In eq. (C.20), one can see that the derivative of the Fermi distribution is with respect to the 2D respective 3D chemical potential. The 3D-QD samples considered in this thesis do not contain a 2D carrier reservoir. Therefore Eq. (C.25) becomes [39]

$$\kappa_{3D} = \sqrt{\frac{e_0^2}{\varepsilon} \sum_{\lambda=e,h} \frac{\partial n_{3D}^{\lambda}}{\partial \mu_{3D}^{\lambda}}}. \quad (\text{C.26})$$

It is not possible to achieve an exact analytic expression of the 3D carrier density $n_{3D} = \sum_{\vec{k} \in \text{Bulk}} f_{\vec{k}}^{3D}$ in terms of the chemical potential. Instead of using approximations like the Debye-Hückel screening wavenumber [39], here the analytic approximation

$$\beta \mu_{3D}^{\lambda}(n_{3D}^{\lambda}) \approx \ln \left[\frac{n_{3D}^{\lambda}}{n_0^{\lambda}} \right] + 4.897 \ln \left[0.045 \frac{n_{3D}^{\lambda}}{n_0^{\lambda}} + 1 \right] + 0.133 \frac{n_{3D}^{\lambda}}{n_0^{\lambda}}, \quad (\text{C.27})$$

$$\text{with } n_0^{\lambda} = \frac{1}{4} \left(\frac{2m_{\lambda} k_B T}{\hbar^2 \pi} \right)^{3/2},$$

by [39, 54, 53] is used to calculate the inverse derivative:

$$\frac{\partial n_{3D}}{\partial \mu_{3D}}(n_{3D}) = \left(\frac{\partial \mu_{3D}}{\partial n_{3D}} \right)^{-1} (n_{3D}) \quad (\text{C.28})$$

$$\approx 0.133 + \frac{0.220365}{1 + 0.045 \frac{n_{3D}}{n_0}} + \frac{n_0}{n_{3D}}. \quad (\text{C.29})$$

Eq. (2.38) will also be used to calculate of Fermi distributions in 3D.

C.2. Screening in 2D

The static dielectric function of a **2D-system** has the form [63]

$$\epsilon(q, 0) = 1 + \frac{\kappa_{2D}^2}{q_{||}}, \quad (\text{C.30})$$

which can be achieved by inserting the 2D Coulomb potential $V_{2D}(\vec{q}_{||}) = \frac{e_0^2}{2\epsilon A q_{||}}$ into eq. (C.21). The 2D screening wavenumber then becomes [39, 2]

$$\kappa_{2D} = \frac{e_0^2}{2\epsilon A} \left(\sum_{\mathbf{k} \in 2\text{DCR}} \frac{\partial f_{\mathbf{k}}^{2D}}{\partial \mu_{2D}} \right) \quad (\text{C.31})$$

$$= \frac{e_0^2}{2\epsilon} \sum_{\lambda=e,h} \left(\frac{\partial n_{2D}^{\lambda}}{\partial \mu_{2D}^{\lambda}} \right). \quad (\text{C.32})$$

In the last step the relation $\frac{\partial f_{\vec{k}}^v}{\partial \mu_v} = \frac{\partial f_{\vec{k}}^h}{\partial \mu_h}$ was used again. Here the influence of the 3D reservoir is not taken into account.

D. Derivation of the T_2 time

Derivation of the dephasing time is based on a Hamiltonian with the form

$$H = H_{0,el} + H_{c-c} \text{ with} \quad (\text{D.1})$$

$$H_{0,el} = \sum_m \varepsilon_m a_m^\dagger a_m, \quad (\text{D.2})$$

$$H_{c-c} = \frac{1}{2} \sum_{a,b,c,d} V_{abcd} a_a^\dagger a_b^\dagger a_c a_d. \quad (\text{D.3})$$

The discussion is focuses on effects caused by Coulomb scattering. One can find a detailed derivation of the scattering rates in Refs. [2, 65, 66]. The derivation of the dephasing time is, to a large extent, the same. Especially since E. Malic used a general notation that is largely not restricted to the treatment of occupation probabilities: The equations of motion (EOM) were set up for the quantity $\langle a_1^\dagger a_2 \rangle$. Only in the final steps the discussion was restricted to diagonal elements of the density matrix (“1 = 2”). That notation will be also used here for derivation of the dephasing time, since (i) results of Malic et al. can easily be used here and (ii) the numbers “1” and “2”, which will be used for fixed QD states, are more clearly distinguishable than the a, b, c, A, B, C, \dots denoting sum indices. Furthermore, the following abbreviations will be used:

$$\begin{aligned} \sigma_{xy} &:= \langle a_x^\dagger a_y \rangle = \rho_{xy}, \\ \sigma_{xy}^\dagger &:= \langle a_y a_x^\dagger \rangle = \delta_{xy} - \rho_{xy}, \\ \sigma_{\alpha\beta\gamma\delta}^{(c)} &:= \langle a_\alpha^\dagger a_\beta^\dagger a_\gamma a_\delta \rangle^{(c)}, \\ \tilde{V}_{ABCD} &:= V_{ABCD} - V_{BACD}, \\ \hbar\omega_{xy} &:= \varepsilon_x - \varepsilon_y, \end{aligned} \quad (\text{D.4})$$

and the Hartree-Fock energy

$$\varepsilon_{1a}^{HF} = \varepsilon_1 \delta_{1a} + \tilde{V}^{ab1c} \langle a_b^\dagger a_c \rangle. \quad (\text{D.5})$$

According to Refs. [2, 65, 66] the EOM for the polarization $\langle a_1^\dagger a_2 \rangle$ takes the form

$$\begin{aligned} i\hbar \frac{d}{dt} \langle a_1^\dagger a_2 \rangle &= \sum_a \left[\varepsilon_{a2}^{HF} \langle a_1^\dagger a_a \rangle - \varepsilon_{1a}^{HF} \langle a_a^\dagger a_2 \rangle \right] \\ &\quad - \frac{1}{2} \sum_{a,b,c} \left[\tilde{V}_{ab1c} \langle a_a^\dagger a_b^\dagger a_c a_2 \rangle^c - \tilde{V}_{2abc} \langle a_1^\dagger a_a^\dagger a_c a_b \rangle^c \right]. \end{aligned} \quad (\text{D.6})$$

As described in Sec. 3.2.1, the next step is to set up and solve the EOM for the quantities $\langle a_a^\dagger a_b^\dagger a_c a_2 \rangle^c$ and $\langle a_1^\dagger a_a^\dagger a_c a_b \rangle^c$. For details, cf. Refs. [2, 65, 66]. Within the limits of the

D. Derivation of the T_2 time

Born approximation, one finally arrives at an inhomogeneous differential equation with the form

$$i\hbar \frac{d}{dt} \sigma_{\alpha\beta\gamma\delta}^c = - \underbrace{(\varepsilon_\alpha + \varepsilon_\beta - \varepsilon_\gamma - \varepsilon_\delta)}_{=: \Delta} \sigma_{\alpha\beta\gamma\delta}^c - \sum_{A,B,C,D} Q_{ABCD}(t), \quad (\text{D.7})$$

with

$$Q_{ABCD} = (t) = \tilde{V}_{ABDC} \left[\sigma_{A\delta} \sigma_{B\gamma} \sigma_{\beta C}^\dagger \sigma_{\alpha D}^\dagger - \sigma_{A\delta}^\dagger \sigma_{B\gamma}^\dagger \sigma_{\beta C} \sigma_{\alpha D} \right]. \quad (\text{D.8})$$

For $t = t_0$ an uncorrelated system is assumed and so $\sigma_{\alpha\beta\gamma\delta}^c(t_0) = 0$. Using the variation of parameters method [107], one arrives at the special solution

$$\sigma_{\alpha\beta\gamma\delta}^c = \frac{i}{\hbar} \sum_{A,B,C,D} \int_{t_0}^t e^{\frac{i}{\hbar} \Delta (t-t')} Q_{ABCD}(t') dt'. \quad (\text{D.9})$$

It is assumed that the inhomogeneity Q_{ABCD} can be decomposed into fast oscillating and a slowly varying part: $Q_{ABCD}(t) = \tilde{Q}_{ABCD}(t) e^{i(\omega_{A\delta} + \omega_{B\gamma} + \omega_{\beta C} + \omega_{\alpha D})t}$ cf. [51]. By applying a Markov approximation one achieves

$$\begin{aligned} \sigma_{\alpha\beta\gamma\delta}^c &= \frac{i}{\hbar} 2 \sum_{A,B,C,D} \int_0^{t-t_0} e^{\frac{i}{\hbar} \Delta s} Q_{ABCD}(t-s) ds \\ &= \frac{i}{\hbar} \sum_{A,B,C,D} \int_0^{t-t_0} e^{\frac{i}{\hbar} \Delta s} \tilde{Q}_{ABCD}(t-s) e^{i(\omega_{A\delta} + \omega_{B\gamma} + \omega_{\beta C} + \omega_{\alpha D})(t-s)} ds \\ &= \frac{i}{\hbar} \sum_{A,B,C,D} \int_0^{t-t_0} e^{\frac{i}{\hbar} (\Delta - \hbar(\omega_{A\delta} + \omega_{B\gamma} + \omega_{\beta C} + \omega_{\alpha D})) s} \tilde{Q}_{ABCD}(t-s) e^{i(\omega_{A\delta} + \omega_{B\gamma} + \omega_{\beta C} + \omega_{\alpha D}) t} ds \\ &\stackrel{\text{Markov}}{\approx} \frac{i}{\hbar} \sum_{A,B,C,D} \tilde{Q}_{ABCD}(t) e^{i(\omega_{A\delta} + \omega_{B\gamma} + \omega_{\beta C} + \omega_{\alpha D}) t} \\ &\quad \times \int_0^{t-t_0} e^{\frac{i}{\hbar} (\Delta - \hbar(\omega_{A\delta} + \omega_{B\gamma} + \omega_{\beta C} + \omega_{\alpha D})) s} ds \\ &= i \sum_{A,B,C,D} Q_{ABCD}(t) \pi g(\Delta - \hbar(\omega_{A\delta} + \omega_{B\gamma} + \omega_{\beta C} + \omega_{\alpha D})) \\ &= i \sum_{A,B,C,D} Q_{ABCD}(t) \pi g(\varepsilon_\alpha + \varepsilon_\beta - \varepsilon_\gamma - \varepsilon_\delta - \hbar(\omega_{A\delta} + \omega_{B\gamma} + \omega_{\beta C} + \omega_{\alpha D})) \\ &= i \sum_{A,B,C,D} Q_{ABCD}(t) \pi g(\varepsilon_D + \varepsilon_C - \varepsilon_A - \varepsilon_B). \end{aligned} \quad (\text{D.10})$$

Here $g(x) := \delta(x) + iP(\frac{1}{x})$, where δ denotes the δ -Distribution and P denotes the principal value [68]. In this thesis, the principal value is always disregarded. The reason for that becomes clear in Eqs. (3.12) and (3.15), where all quantities are real¹

¹Note that (i) similar to Eqs. (D.13) and (D.14), the Boltzmann equation could be expressed in terms of $|\tilde{V}\dots|^2$, instead of direct and exchange interaction. Therefore, the exchange term is also a real quantity. (ii) For the Gain model, the QDs do not have excited states. Hence, the overlap integrals are real quantities, cf. Eqs. (B.1) and (B.3).

As a result of that the factor $\text{i}P(\frac{1}{x})$ would cause imaginary quantities. However, the Boltzmann equation (3.12) contains only real quantities. In the EOM of the microscopic polarization Eq. (3.14), the principal value could lead to corrections to eigenenergy, which are not considered here.

Equation (D.10) can be inserted into Eq. (D.6):

$$\sum_{a,b,c} \tilde{V}_{ab1c} \langle a_a^\dagger a_b^\dagger a_c a_2 \rangle^c = \text{i}\pi \sum_{a,b,c} \sum_{A,B,C,D} \tilde{V}_{ab1c} \tilde{V}_{ABDC} \left[\sigma_{A2} \sigma_{Bc} \sigma_{bC}^\dagger \sigma_{aD}^\dagger - \sigma_{A2}^\dagger \sigma_{Bc}^\dagger \sigma_{bC} \sigma_{aD} \right] \times \delta(\varepsilon_D + \varepsilon_C - \varepsilon_B - \varepsilon_A), \quad (\text{D.11})$$

and

$$\sum_{a,b,c} \tilde{V}_{2abc} \langle a_1^\dagger a_a^\dagger a_c a_b \rangle^c = \text{i}\pi \sum_{a,b,c} \sum_{A,B,C,D} \tilde{V}_{2abc} \tilde{V}_{ABDC} \left[\sigma_{Ab} \sigma_{Bc} \sigma_{aC}^\dagger \sigma_{1D}^\dagger - \sigma_{Ab}^\dagger \sigma_{Bc}^\dagger \sigma_{aC} \sigma_{1D} \right] \times \delta(\varepsilon_D + \varepsilon_C - \varepsilon_A - \varepsilon_B). \quad (\text{D.12})$$

Equations (D.11) and (D.12) contain sums over all system states. The scope of this thesis is restricted to contributions that are linear in the QD polarization p_{12} , and where other single particle states are diagonal elements of the density matrix $\rho_x = \langle a_x^\dagger a_x \rangle$. For derivation of scattering rates, the terms σ_{A2} and σ_{1D} in Eq. (D.11) and (D.12) reflect the term derived from the left-hand side of the differential equation. So assuming $A = 1$ in Eq. (D.11) and $D = 2$ in (D.12), and limiting ourselves to diagonal elements for the other density matrix elements, one arrives at

$$\sum_{a,b,c} \tilde{V}_{ab1c} \langle a_a^\dagger a_b^\dagger a_c a_2 \rangle^c = \text{i}\pi \sum_{a,b,c} \tilde{V}_{ab1c} \tilde{V}_{1cab} \left[p_{12} \rho_c (1 - \rho_b) (1 - \rho_a) + p_{12} (1 - \rho_c) \rho_b \rho_a \right] \times \delta(\varepsilon_a + \varepsilon_b - \varepsilon_c - \varepsilon_1) \quad (\text{D.13})$$

and

$$\sum_{a,b,c} \tilde{V}_{2abc} \langle a_1^\dagger a_a^\dagger a_c a_b \rangle^c = -\text{i}\pi \sum_{a,b,c} \tilde{V}_{2abc} \tilde{V}_{bc2a} \left[\rho_b \rho_c (1 - \rho_a) p_{12} + (1 - \rho_b) (1 - \rho_c) \rho_a p_{12} \right] \times \delta(\varepsilon_2 + \varepsilon_a - \varepsilon_b - \varepsilon_c). \quad (\text{D.14})$$

These terms thus correspond to terms that are known from the scattering rates. However, in Eqs. (D.11) and (D.12), other matrix elements could also form the polarization p_{12} . The matrix elements σ_{A2} and σ_{1D} then become diagonal elements. In the following discussion of these contributions Eqs. (D.11) and (D.12) will be discussed separately.

D. Derivation of the T_2 time

Contributions to Eq. (D.11)

Under the condition $\sigma_{A2} = \rho_2$ one arrives at

$$\begin{aligned}
& \sum_{a,b,c} \tilde{V}_{ab1c} \langle a_a^\dagger a_b^\dagger a_c a_2 \rangle^c \\
&= \text{i}\pi \sum_{a,b,c} \sum_{B,D,C} \tilde{V}_{ab1c} \tilde{V}_{2BDC} \left[\sigma_{22} \sigma_{Bc} \sigma_{bC}^\dagger \sigma_{aD}^\dagger - \sigma_{22}^\dagger \sigma_{Bc}^\dagger \sigma_{bC} \sigma_{aD} \right] \delta(\varepsilon_a + \varepsilon_b - \varepsilon_c - \varepsilon_1) \\
&= \text{i}\pi \sum_{a,b,c} \sum_{B,D,C} \left((V_{ab1c} - V_{ba1c})(V_{2BDC} - V_{2BCD}) \right) \left[\sigma_{22} \sigma_{Bc} \sigma_{bC}^\dagger \sigma_{aD}^\dagger - \sigma_{22}^\dagger \sigma_{Bc}^\dagger \sigma_{bC} \sigma_{aD} \right] \\
&\quad \times \delta(\varepsilon_a + \varepsilon_b - \varepsilon_c - \varepsilon_1) \\
&= \text{i}\pi \sum_{a,b,c} \sum_{B,D,C} \left(V_{ab1c} V_{2BDC} - V_{ab1c} V_{2BCD} - V_{ba1c} V_{2BDC} + V_{ba1c} V_{2BCD} \right) \\
&\quad \times \left[\sigma_{22} \sigma_{Bc} \sigma_{bC}^\dagger \sigma_{aD}^\dagger - \sigma_{22}^\dagger \sigma_{Bc}^\dagger \sigma_{bC} \sigma_{aD} \right] \delta(\varepsilon_a + \varepsilon_b - \varepsilon_c - \varepsilon_1) \tag{D.15}
\end{aligned}$$

One of the σ_{xy} has to be equal to the interband-QD-polarization p_{12} . This gives rise to the contributions²:

- $\sigma_{Bc} = p_{12}$:

$$\begin{aligned}
& \text{i}\pi \sum_{a,b} \sum_{C,D} \left(V_{ab12} V_{21DC} - V_{ab12} V_{21CD} - V_{ba12} V_{21DC} + V_{ba12} V_{21CD} \right) \\
&\quad \times \left[\sigma_{22} \sigma_{12} \sigma_{bC}^\dagger \sigma_{aD}^\dagger - \sigma_{22}^\dagger \sigma_{12}^\dagger \sigma_{bC} \sigma_{aD} \right] \delta(\varepsilon_a + \varepsilon_b - \varepsilon_2 - \varepsilon_1) \\
&= \text{i}\pi \sum_{a,b} \sum_{D,C} \left(-V_{ab12} V_{21CD} - V_{ba12} V_{21DC} \right) \\
&\quad \times \left[\sigma_{22} p_{12} \sigma_{bC}^\dagger \sigma_{aD}^\dagger - \sigma_{22}^\dagger (-p_{12}) \sigma_{bC} \sigma_{aD} \right] \delta(\varepsilon_a + \varepsilon_b - \varepsilon_2 - \varepsilon_1) \tag{D.16}
\end{aligned}$$

- $\sigma_{bC} = p_{12}$:

$$\begin{aligned}
& \text{i}\pi \sum_{a,c} \sum_{B,D} \left(V_{a11c} V_{2BD2} - V_{a11c} V_{2B2D} - V_{1a1c} V_{2BD2} + V_{1a1c} V_{2B2D} \right) \\
&\quad \times \left[\sigma_{22} \sigma_{Bc} \sigma_{12}^\dagger \sigma_{aD}^\dagger - \sigma_{22}^\dagger \sigma_{Bc}^\dagger \sigma_{12} \sigma_{aD} \right] \delta(\varepsilon_a + \varepsilon_1 - \varepsilon_c - \varepsilon_2 + \hbar\omega_{21}) \\
&= \text{i}\pi \sum_{a,c} \sum_{B,D} \left(V_{a11c} V_{2BD2} - V_{a11c} V_{2B2D} - V_{1a1c} V_{2BD2} \right) \\
&\quad \times \left[\sigma_{22} \sigma_{Bc} (-p_{12}) \sigma_{aD}^\dagger - \sigma_{22}^\dagger \sigma_{Bc}^\dagger p_{12} \sigma_{aD} \right] \delta(\varepsilon_a - \varepsilon_c) \tag{D.17}
\end{aligned}$$

²In the following, the relation $\sigma_{12}^\dagger = \langle a_2 a_1^\dagger \rangle = \delta_{12} - \rho_{12} = -p_{12}$ will be used several times.

- $\sigma_{aD} = p_{12}$:

$$\begin{aligned}
& \text{i}\pi \sum_{b,c} \sum_{B,C} \left(V_{1b1c} V_{2B2C} - V_{1b1c} V_{2BC2} - V_{b11c} V_{2B2C} + V_{b11c} V_{2BC2} \right) \\
& \quad \times \left[\sigma_{22} \sigma_{Bc} \sigma_{bC}^\dagger \sigma_{12}^\dagger - \sigma_{22}^\dagger \sigma_{Bc}^\dagger \sigma_{bC} \sigma_{12} \right] \delta(\varepsilon_1 + \varepsilon_b - \varepsilon_c - \varepsilon_2 + \hbar\omega_{21}) \\
& = \text{i}\pi \left(-V_{1b1c} V_{2BC2} - V_{b11c} V_{2B2C} + V_{b11c} V_{2BC2} \right) \\
& \quad \times \left[\sigma_{22} \sigma_{Bc} \sigma_{bC}^\dagger (-p_{12}) - \sigma_{22}^\dagger \sigma_{Bc}^\dagger \sigma_{bC} p_{12} \right] \delta(\varepsilon_b - \varepsilon_c) \tag{D.18}
\end{aligned}$$

The terms marked in red vanish because of the assumption that only one interband polarization is considered, and the condition that the two inner respective the two outer indices have to be of the same carrier type/ band Λ , $V_{ABCD} \sim \delta_{\Lambda_A, \Lambda_D} \delta_{\Lambda_B, \Lambda_C}$. As the terms that cause polarization p_{12} are fixed now, the other matrix elements can be limited

D. Derivation of the T_2 time

to diagonal elements, so a *random phase approximation* is made [39]:

$$\begin{aligned}
& \sum_{a,b,x} \tilde{V}_{ab1c} \langle a_a^\dagger a_b^\dagger a_c a_2 \rangle^c \\
= & \text{i}\pi 2 \sum_{a,b,c} V_{ab1c} (V_{1cab} - V_{1cba}) [p_{12}\rho_c(1-\rho_b)(1-\rho_a) + p_{12}(1-\rho_c)\rho_b\rho_a] \\
& \times \delta(\varepsilon_a + \varepsilon_b - \varepsilon_c - \varepsilon_2 + \hbar\omega_{21}) \\
& + \text{i}\pi \sum_{a,b} \left(-V_{ab12}V_{21ba} - V_{ba12}V_{21ab} \right) [\rho_2 p_{12}(1-\rho_b)(1-\rho_a) - (1-\rho_2)(-p_{12})\rho_b\rho_a] \\
& \times \delta(\varepsilon_a + \varepsilon_b - \varepsilon_2 - \varepsilon_1) \\
& + \text{i}\pi \sum_{a,c} \left(V_{a11c}V_{2ca2} - V_{a11c}V_{2c2a} - V_{1a1c}V_{2ca2} \right) \\
& \times [\rho_2\rho_c(-p_{12})(1-\rho_a) - (1-\rho_2)(1-\rho_c)p_{12}\rho_a] \delta(\varepsilon_a - \varepsilon_c) \\
& + \text{i}\pi \sum_{b,c} \left(-V_{1b1c}V_{2cb2} - V_{b11c}V_{2c2b} + V_{b11c}V_{2cb2} \right) \\
& \times [\rho_2\rho_c(1-\rho_b)(-p_{12}) - (1-\rho_2)(1-\rho_c)\rho_b p_{12}] \delta(\varepsilon_b - \varepsilon_c) \\
= & \text{i}\pi 2 \sum_{a,b,c} V_{ab1c} (V_{1cab} - V_{1cba}) [p_{12}\rho_c(1-\rho_b)(1-\rho_a) + p_{12}(1-\rho_c)\rho_b\rho_a] \\
& \times \delta(\varepsilon_a + \varepsilon_b - \varepsilon_c - \varepsilon_2 + \hbar\omega_{21}) \\
& + \text{i}\pi \sum_{a,b} \left(-V_{ab12}V_{21ba} - V_{ba12}V_{21ab} \right) \\
& \times [\rho_2 p_{12}(1-\rho_b)(1-\rho_a) - (1-\rho_2)(-p_{12})\rho_b\rho_a] \delta(\varepsilon_a + \varepsilon_b - \varepsilon_2 - \varepsilon_1) \\
& - \text{i}\pi \sum_{a,c} \left(V_{a11c}V_{2ca2} - V_{a11c}V_{2c2a} - V_{1a1c}V_{2ca2} \right) [p_{12}(1-\rho_c)\rho_a] \delta(\varepsilon_a - \varepsilon_c) \\
& - \text{i}\pi \sum_{b,c} \left(-V_{1b1c}V_{2cb2} - V_{b11c}V_{2c2b} + V_{b11c}V_{2cb2} \right) [p_{12}(1-\rho_c)\rho_b] \delta(\varepsilon_b - \varepsilon_c) \\
= & \text{i}\pi 2 \sum_{a,b,c} V_{ab1c} (V_{1cab} - V_{1cba}) [p_{12}\rho_c(1-\rho_b)(1-\rho_a) + p_{12}(1-\rho_c)\rho_b\rho_a] \\
& \times \delta(\varepsilon_a + \varepsilon_b - \varepsilon_c - \varepsilon_2 + \hbar\omega_{21}) \\
& + \text{i}\pi 2 \sum_{a,b} \left(-V_{ab12}V_{21ba} \right) [\rho_2 p_{12}(1-\rho_b)(1-\rho_a) - (1-\rho_2)(-p_{12})\rho_b\rho_a] \\
& \times \delta(\varepsilon_a + \varepsilon_b - \varepsilon_2 - \varepsilon_1) \\
& - 2\text{i}\pi \sum_{a,c} \left(V_{a11c}V_{2ca2} - V_{a11c}V_{2c2a} - V_{1a1c}V_{2ca2} \right) [p_{12}(1-\rho_c)\rho_a] \delta(\varepsilon_a - \varepsilon_c) \quad (\text{D.19})
\end{aligned}$$

The last step was based on the Fermi distributions being dependent only on the energy of the state, which has to be the same for the two states over which we sum up, due to the δ -distribution.

Contributions to Eq. (D.12)

Of course, the same steps must also be performed with second-term (D.12). So under the condition $\sigma_{1D} = \rho_1$ one arrives at

$$\begin{aligned}
& \text{i}\pi \sum_{a,b,c} \sum_{A,B,C} \tilde{V}_{2abc} \tilde{V}_{AB1C} \left[\sigma_{Ab} \sigma_{Bc} \sigma_{aC}^\dagger \sigma_{11}^\dagger - \sigma_{Ab}^\dagger \sigma_{Bc}^\dagger \sigma_{aC} \sigma_{11} \right] \delta(\varepsilon_2 + \varepsilon_a - \varepsilon_b - \varepsilon_c) \\
&= \text{i}\pi \sum_{a,b,c} \sum_{A,B,C} \left((V_{2abc} - V_{2acb})(V_{AB1C} - V_{BA1C}) \right) \\
&\quad \times \left[\sigma_{Ab} \sigma_{Bc} \sigma_{aC}^\dagger \sigma_{11}^\dagger - \sigma_{Ab}^\dagger \sigma_{Bc}^\dagger \sigma_{aC} \sigma_{11} \right] \delta(\varepsilon_2 + \varepsilon_a - \varepsilon_b - \varepsilon_c) \\
&= \text{i}\pi \sum_{a,b,c} \sum_{A,B,C} \left(V_{2abc} V_{AB1C} - V_{2abc} V_{BA1C} - V_{2acb} V_{AB1C} + V_{2acb} V_{BA1C} \right) \\
&\quad \times \left[\sigma_{Ab} \sigma_{Bc} \sigma_{aC}^\dagger \sigma_{11}^\dagger - \sigma_{Ab}^\dagger \sigma_{Bc}^\dagger \sigma_{aC} \sigma_{11} \right] \delta(\varepsilon_2 + \varepsilon_a - \varepsilon_b - \varepsilon_c) \tag{D.20}
\end{aligned}$$

Again, one of the σ_{xy} should give rise to the polarization p_{12} , leading to ³:

- $\sigma_{aC} = p_{12}$:

$$\begin{aligned}
& \text{i}\pi \sum_{b,c} \sum_{A,B} \left(V_{21bc} V_{AB12} - V_{21bc} V_{BA12} - V_{21cb} V_{AB12} + V_{21cb} V_{BA12} \right) \\
&\quad \times \left[\sigma_{Ab} \sigma_{Bc} \sigma_{12}^\dagger \sigma_{11}^\dagger - \sigma_{Ab}^\dagger \sigma_{Bc}^\dagger \sigma_{12} \sigma_{11} \right] \delta(\varepsilon_1 + \varepsilon_1 - \varepsilon_b - \varepsilon_c + \hbar\omega_{21}) \\
&= \text{i}\pi \sum_{b,c} \sum_{A,B} \left(-V_{21bc} V_{BA12} - V_{21cb} V_{AB12} \right) \\
&\quad \times \left[\sigma_{Ab} \sigma_{Bc} (-p_{12}) \sigma_{11}^\dagger - \sigma_{Ab}^\dagger \sigma_{Bc}^\dagger p_{12} \sigma_{11} \right] \delta(\varepsilon_2 + \varepsilon_1 - \varepsilon_b - \varepsilon_c) \tag{D.21}
\end{aligned}$$

- $\sigma_{Bc} = p_{12}$:

$$\begin{aligned}
& \text{i}\pi \sum_{a,b} \sum_{A,C} \left(V_{2ab2} V_{A11C} - V_{2ab2} V_{1A1C} - V_{2a2b} V_{A11C} + V^{2a2b} V^{1A1C} \right) \\
&\quad \times \left[\sigma_{Ab} \sigma_{12} \sigma_{aC}^\dagger \sigma_{11}^\dagger - \sigma_{Ab}^\dagger \sigma_{12}^\dagger \sigma_{aC} \sigma_{11} \right] \delta(\varepsilon_2 + \varepsilon_a - \varepsilon_b - \varepsilon_2) \\
&= \text{i}\pi \sum_{a,b} \sum_{A,C} \left(V_{2ab2} V_{A11C} - V_{2ab2} V_{1A1C} - V_{2a2b} V_{A11C} \right) \\
&\quad \times \left[\sigma_{Ab} p_{12} \sigma_{aC}^\dagger \sigma_{11}^\dagger - \sigma_{Ab}^\dagger (-p_{12}) \sigma_{aC} \sigma_{11} \right] \delta(\varepsilon_a - \varepsilon_b) \tag{D.22}
\end{aligned}$$

³In the following, the relation $\sigma_{12}^\dagger = \langle a_2 a_1^\dagger \rangle = \delta_{12} - \rho_{12} = -p_{12}$ will be used several times.

D. Derivation of the T_2 time

- $\sigma_{Ab} = p_{12}$:

$$\begin{aligned}
& i\pi \sum_{a,c} \sum_{B,C} \left(V_{2a2c} V_{1B1C} - V_{2a2c} V_{B11C} - V_{2ac2} V_{1B1C} + V_{2ac2} V_{B11C} \right) \\
& \times \left[\sigma_{12} \sigma_{Bc} \sigma_{aC}^\dagger \sigma_{11}^\dagger - \sigma_{12}^\dagger \sigma_{Bc}^\dagger \sigma_{aC} \sigma_{11} \right] \delta(\varepsilon_2 + \varepsilon_a - \varepsilon_2 - \varepsilon_c) \\
= & i\pi \sum_{a,c} \sum_{B,C} \left(-V_{2a2c} V_{B11C} - V_{2ac2} V_{1B1C} + V_{2ac2} V_{B11C} \right) \\
& \times \left[p_{12} \sigma_{Bc} \sigma_{aC}^\dagger \sigma_{11}^\dagger - (-p_{12}) \sigma_{Bc}^\dagger \sigma_{aC} \sigma_{11} \right] \delta(\varepsilon_a - \varepsilon_c) \tag{D.23}
\end{aligned}$$

Terms marked **red** once again vanish. One finally arrives at

$$\begin{aligned}
& \sum_{a,b,c} \tilde{V}_{2abc} \langle a_1^\dagger a_a^\dagger a_c a_b \rangle^c \\
= & -i\pi \sum_{a,b,c} \tilde{V}_{2abc} \tilde{V}_{bc2a} [\rho_b \rho_c (1 - \rho_a) p_{12} + (1 - \rho_b)(1 - \rho_c) \rho_a p_{12}] \delta(\varepsilon_2 + \varepsilon_a - \varepsilon_b - \varepsilon_c) \\
& + i\pi \sum_{b,c} \left(-V_{21bc} V_{cb12} - V_{21cb} V_{bc12} \right) \\
& \quad \times [\rho_b \rho_c (-p_{12})(1 - \rho_1) - (1 - \rho_b)(1 - \rho_c) p_{12} \rho_1] \delta(\varepsilon_2 + \varepsilon_1 - \varepsilon_b - \varepsilon_c) \\
& + i\pi \sum_{a,b} \left(V_{2ab2} V^{b11a} - V_{2ab2} V_{1b1a} - V_{2a2b} V_{b11a} \right) \\
& \quad \times [\rho_b p_{12} (1 - \rho_a)(1 - \rho_1) + (1 - \rho_b) p_{12} \rho_a \rho_1] \delta(\varepsilon_a - \varepsilon_b) \\
& + i\pi \sum_{a,c} \left(-V_{2a2c} V_{c11a} - V_{2ac2} V_{1c1a} + V_{2ac2} V_{c11a} \right) \\
& \quad \times [p_{12} \rho_c (1 - \rho_a)(1 - \rho_1) + p_{12} (1 - \rho_c) \rho_a \rho_1] \delta(\varepsilon_a - \varepsilon_c) \\
= & -i\pi 2 \sum_{a,b,c} V_{2abc} (V_{bc2a} - V_{cb2a}) \\
& \quad \times [\rho_b \rho_c (1 - \rho_a) p_{12} + (1 - \rho_b)(1 - \rho_c) \rho_a p_{12}] \delta(\varepsilon_2 + \varepsilon_a - \varepsilon_b - \varepsilon_c) \\
& + i\pi \sum_{b,c} \left(-V_{21bc} V_{cb12} - V_{21cb} V_{bc12} \right) \\
& \quad \times [\rho_b \rho_c (-p_{12})(1 - \rho_1) - (1 - \rho_b)(1 - \rho_c) p_{12} \rho_1] \delta(\varepsilon_2 + \varepsilon_1 - \varepsilon_b - \varepsilon_c) \\
& + i\pi \sum_{a,b} \left(V_{2ab2} V_{b11a} - V_{2ab2} V_{1b1a} - V_{2a2b} V_{b11a} \right) [p_{12} \rho_b (1 - \rho_a)] \delta(\varepsilon_a - \varepsilon_b) \\
& + i\pi \sum_{a,c} \left(-V_{2a2c} V_{c11a} - V_{2ac2} V_{1c1a} + V_{2ac2} V_{c11a} \right) [p_{12} \rho_c (1 - \rho_a)] \delta(\varepsilon_a - \varepsilon_c) \\
= & -i\pi 2 \sum_{a,b,c} V_{2abc} (V_{bc2a} - V_{cb2a}) \\
& \quad \times [\rho_b \rho_c (1 - \rho_a) p_{12} + (1 - \rho_b)(1 - \rho_c) \rho_a p_{12}] \delta(\varepsilon_2 + \varepsilon_a - \varepsilon_b - \varepsilon_c) \\
& + i\pi 2 \sum_{b,c} \left(-V_{21bc} V_{cb12} \right) \\
& \quad \times [\rho_b \rho_c (-p_{12})(1 - \rho_1) - (1 - \rho_b)(1 - \rho_c) p_{12} \rho_1] \delta(\varepsilon_2 + \varepsilon_1 - \varepsilon_b - \varepsilon_c) \\
& + 2i\pi \sum_{a,b} \left(V_{2ab2} V_{b11a} - V_{2ab2} V_{1b1a} - V_{2a2b} V_{b11a} \right) [p_{12} \rho_b (1 - \rho_a)] \delta(\varepsilon_a - \varepsilon_b)
\end{aligned} \tag{D.24}$$

Previously, we used Fermi distributions being dependent only on the energy of the state, which has to be the same for the two states over which we sum up, due to the δ -distribution.

Combination of the two contributions

Inserting Eq. (D.19) and (D.24) into (D.6) leads to

$$\begin{aligned}
& i\hbar \frac{d}{dt} \langle a_1^\dagger a_2 \rangle \\
&= \sum_a \left[\varepsilon_{a2}^{HF} \langle a_1^\dagger a_a \rangle - \varepsilon_{1a}^{HF} \langle a_a^\dagger a_2 \rangle \right] - \frac{1}{2} \sum_{a,b,c} \left[\tilde{V}_{ab1c} \langle a_a^\dagger a_b^\dagger a_c a_2 \rangle^c - \tilde{V}_{2abc} \langle a_1^\dagger a_a^\dagger a_c a_b \rangle^c \right] \\
&= \sum_a \left[\varepsilon_{a2}^{HF} \langle a_1^\dagger a_a \rangle - \varepsilon_{1a}^{HF} \langle a_a^\dagger a_2 \rangle \right] \\
&\quad - \frac{i\pi 2}{2} \left\{ \sum_{a,b,c} V_{ab1c} (V_{1cab} - V_{1cba}) [p_{12} \rho_c (1 - \rho_b)(1 - \rho_a) + p_{12} (1 - \rho_c) \rho_b \rho_a] \right. \\
&\quad \quad \times \delta(\varepsilon_a + \varepsilon_b - \varepsilon_c - \varepsilon_1) \\
&\quad \quad + \sum_{a,b} \left(-V_{ab12} V_{21ba} \right) [\rho_2 p_{12} (1 - \rho_b)(1 - \rho_a) - (1 - \rho_2)(-p_{12}) \rho_b \rho_a] \\
&\quad \quad \times \delta(\varepsilon_a + \varepsilon_b - \varepsilon_2 - \varepsilon_1) \\
&\quad \quad - \sum_{a,c} \left(V_{a11c} V_{2ca2} - V_{a11c} V_{2c2a} - V_{1a1c} V_{2ca2} \right) [p_{12} (1 - \rho_c) \rho_a] \delta(\varepsilon_a - \varepsilon_c) \\
&\quad \quad - \left[- \sum_{a,b,c} V_{2abc} (V_{bc2a} - V_{cb2a}) [\rho_b \rho_c (1 - \rho_a) p_{12} + (1 - \rho_b)(1 - \rho_c) \rho_a p_{12}] \right. \\
&\quad \quad \quad \times \delta(\varepsilon_2 + \varepsilon_a - \varepsilon_b - \varepsilon_c) \\
&\quad \quad \quad + \sum_{b,c} \left(-V_{21bc} V_{cb12} \right) [\rho_b \rho_c (-p_{12})(1 - \rho_1) - (1 - \rho_b)(1 - \rho_c) p_{12} \rho_1] \\
&\quad \quad \quad \times \delta(\varepsilon_2 + \varepsilon_1 - \varepsilon_b - \varepsilon_c) \\
&\quad \quad \quad \left. + \sum_{a,b} \left(V_{2ab2} V_{b11a} - V_{2ab2} V_{1b1a} - V_{2a2b} V_{b11a} \right) [p_{12} \rho_b (1 - \rho_a)] \delta(\varepsilon_a - \varepsilon_b) \right\} \\
&= \sum_a \left[\varepsilon_{a2}^{HF} \langle a_1^\dagger a_a \rangle - \varepsilon_{1a}^{HF} \langle a_a^\dagger a_2 \rangle \right] \\
&\quad - i\pi \left\{ \sum_{a,b,c} V_{ab1c} (V_{1cab} - V_{1cba}) [\rho_c (1 - \rho_b)(1 - \rho_a) + (1 - \rho_c) \rho_b \rho_a] \delta(\varepsilon_a + \varepsilon_b - \varepsilon_c - \varepsilon_1) \right. \\
&\quad \quad + \sum_{a,b,c} V_{2abc} (V_{bc2a} - V_{cb2a}) [\rho_b \rho_c (1 - \rho_a) + (1 - \rho_b)(1 - \rho_c) \rho_a] \delta(\varepsilon_2 + \varepsilon_a - \varepsilon_b - \varepsilon_c) \\
&\quad \quad - 2 \sum_{a,c} \left(V_{a11c} V_{2ca2} - V_{a11c} V_{2c2a} - V_{1a1c} V_{2ca2} \right) [(1 - \rho_c) \rho_a] \delta(\varepsilon_a - \varepsilon_c) \tag{D.25} \\
&\quad \quad - \sum_{a,b} \left(V_{ab12} V_{21ba} \right) [\rho_2 (1 - \rho_b)(1 - \rho_a) + (1 - \rho_2) \rho_b \rho_a] \delta(\varepsilon_a + \varepsilon_b - \varepsilon_2 - \varepsilon_1) \\
&\quad \quad \left. - \sum_{b,c} \left(V_{21bc} V_{cb12} \right) [\rho_b \rho_c (1 - \rho_1) + (1 - \rho_b)(1 - \rho_c) \rho_1] \delta(\varepsilon_2 + \varepsilon_1 - \varepsilon_b - \varepsilon_c) \right\} p_{12}
\end{aligned}$$

Finally, the Coulomb-matrix V_{abcd} elements of the second-order contribution are re-

placed by related screened ones:

$$V_{abdc} \longrightarrow \frac{V_{abdc}}{\epsilon} \approx \frac{V_{abdc}}{1 + \frac{\kappa}{q}} =: W_{abdc}. \quad (\text{D.26})$$

A comparison with

$$\dot{p}_{12} = \frac{i}{\hbar}(\varepsilon_1 - \varepsilon_1)p_{12} - \frac{1}{T_2}p_{12}. \quad (\text{D.27})$$

leads to the dephasing time [99]

$$\begin{aligned} T_2^{-1} = & \frac{\pi}{\hbar} \left\{ \right. \\ & \sum_{a,b,c} \left[W_{abD_1c} (W_{1cab} - W_{1cba}) [\rho_c(1 - \rho_b)(1 - \rho_a) + (1 - \rho_c)\rho_b\rho_a] \right. \\ & \quad \times \delta(\varepsilon_a + \varepsilon_b - \varepsilon_c - \varepsilon_1) \\ & \quad + W_{2abc} (W_{bc2a} - W_{cb2a}) [\rho_b\rho_c(1 - \rho_a) + (1 - \rho_b)(1 - \rho_c)\rho_a] \\ & \quad \left. \times \delta(\varepsilon_2 + \varepsilon_a - \varepsilon_b - \varepsilon_c) \right] \\ & - 2 \sum_{a,c} \left(W_{a1D_1c} W_{2caD_2} - W_{a11c} W_{2c2a} - W_{1a1c} W_{2ca2} \right) [(1 - \rho_c)\rho_a] \\ & \quad \times \delta(\varepsilon_a - \varepsilon_c) \\ & - \sum_{a,b} \left(W_{ab12} W_{21ba} \right) [\rho_2(1 - \rho_b)(1 - \rho_a) + (1 - \rho_2)\rho_b\rho_a] \\ & \quad \times \delta(\varepsilon_a + \varepsilon_b - \varepsilon_2 - \varepsilon_1) \\ & - \sum_{b,c} \left(W_{21bc} W_{cb12} \right) [\rho_b\rho_c(1 - \rho_1) + (1 - \rho_b)(1 - \rho_c)\rho_1] \\ & \quad \left. \times \delta(\varepsilon_2 + \varepsilon_1 - \varepsilon_b - \varepsilon_c) \right\}. \quad (\text{D.28}) \end{aligned}$$

E. Light matter interaction

In this chapter, the connection between the microscopic material response to the macroscopic \vec{E} -field will be motivated. A detailed discussion of optical modes in semiconductor lasers can be found in Refs. [87, 108], from which several fundamental relations in the following discussion are taken. For this purpose, an edge-emitting laser with a quasi-planar waveguide is assumed. According to Ref. [87], for stable transverse (TE) waveguiding the main component of the \vec{E} -field can be written as

$$\vec{E}(z, \vec{r}_{\parallel}, \omega) = e^{i\omega t} \left[\Psi^+(z, t) e^{-i\beta z} + \Psi^-(z, t) e^{i\beta z} \right] \Xi_0(\vec{r}_{\parallel}). \quad (\text{E.1})$$

In frequency space, the transverse main modes $\Xi_0(\vec{r}_{\parallel})$ have to fulfill the wave-guide equation [47]

$$\left[\Delta_{r_{\parallel}} + \frac{\omega^2}{c^2} \varepsilon_r(\omega) - \beta^2 \right] \Xi_0(\vec{r}_{\parallel}) = 0, \quad (\text{E.2})$$

where β^2 denotes the (complex) eigenvalues. Here, permittivity ε_r can be expressed as a function of the refractive index n_r , the background losses α_{bg} , and the material gain g [87]

$$\varepsilon_r(\omega) = \left[n(\omega) - i \frac{c}{2\omega} (g(\omega) - \alpha_{bg}) \right]^2. \quad (\text{E.3})$$

Furthermore, it has to fulfill the material equations

$$\begin{aligned} \vec{D}(\omega) &= \varepsilon_0 \vec{E}(\omega) + \vec{P}(\omega) \\ &= \varepsilon_0 \vec{E}(\omega) + \varepsilon_0 \chi(\omega) \vec{E}(\omega) \\ &= \varepsilon_0 (1 + \chi(\omega)) \vec{E}(\omega) \\ &=: \varepsilon_0 \varepsilon_r \vec{E}(\omega). \end{aligned} \quad (\text{E.4})$$

$$\vec{P}(\omega) = \vec{P}_{QD}(\omega) + \vec{P}_{bg}(\omega) \quad (\text{E.5})$$

$$= \varepsilon_0 (\chi_{QD}(\omega) + \chi_{bg}(\omega)) \vec{E}(\omega) \quad (\text{E.6})$$

$$=: \varepsilon_0 \chi(\omega) \vec{E}(\omega). \quad (\text{E.7})$$

Here, \vec{P} denotes macroscopic polarization and χ denotes susceptibility. Those quantities can be split into a QD contribution (\vec{P}_{QD}/χ_{QD}) and a contribution of the surrounding / background material (\vec{P}_{bg}/χ_{bg}). c denotes the speed of light. With the Eqs. (E.4) and

E. Light matter interaction

(E.7), the quantities n_r and g can be expressed as [39]

$$\text{Im}(\varepsilon_r) = -\frac{c}{\omega}n(g(\omega) - \alpha_{bg}) \quad (\text{E.8})$$

$$\Leftrightarrow (g(\omega) - \alpha_{bg}) = -\frac{\omega}{c}\text{Im}(\varepsilon_r) \quad (\text{E.9})$$

$$\text{Eqs. (E.4), (E.7) and (E.6)} \quad -\frac{\omega}{c}\text{Im}\left(\frac{(\vec{P}_{QD} + \vec{P}_{bg}) \cdot \vec{e}_E}{\vec{E} \cdot \vec{e}_E}\right) \quad (\text{E.10})$$

and

$$\text{Re}(\varepsilon_r) = n^2 - \left(\frac{c}{2\omega}\right)^2 \quad (\text{E.11})$$

$$\Rightarrow n_r = \sqrt{\frac{1}{2}\left[\text{Re}(\varepsilon(\omega)) + \sqrt{\text{Re}(\varepsilon^2(\omega)) + \text{Im}(\varepsilon^2(\omega))}\right]} \quad (\text{E.12})$$

$$\approx \sqrt{\text{Re}(\varepsilon(\omega))}. \quad (\text{E.13})$$

Equation (E.12) can be proven by inserting into Eq. (E.11).

Macroscopic polarization is the sum of microscopic polarizations

$$\vec{P}(\omega) = \sum_{i,j} \frac{\vec{d}_{ij}^*}{AL} \hat{p}_{ij}(\omega) + \frac{\vec{d}_{ij}}{AL} \hat{p}_{ij}^*(\omega). \quad (\text{E.14})$$

Therefore Eqs. (E.10), (E.12) and (E.14) constitutes bridge between the macroscopic scale, important for a description of optics in a device, and the microscopic scale, necessary for a detailed description of material response.

E.1. Calculation of macroscopic polarization

Microscopic polarization $\hat{p}_{ij}(\omega)$ in the frequency domain will be determined via a Fourier transformation of the equation of motion (EOM) for $p_{ij}(t)$. To determine the EOM, the following Hamiltonian is assumed:

$$H = H_{0,el} + H_{int}, \quad (\text{E.15})$$

$$H_{0,el} = \sum_m \varepsilon_m a_m^\dagger a_m, \quad (\text{E.16})$$

$$\begin{aligned} H_{int} &= -\int d\vec{r} \vec{E}(\vec{r}, t) \hat{\psi}^\dagger(\vec{r}, t) \vec{r} \hat{\psi}(\vec{r}, t), \\ &= -\sum_{m,n} \vec{E}(t) \cdot \vec{d}_{mn} a_m^\dagger a_n, \end{aligned} \quad (\text{E.17})$$

$$H_{c-c} = \frac{1}{2} \sum_{abcd} V_{abcd} a_a^\dagger a_b^\dagger a_c a_d, \quad (\text{E.18})$$

It is assumed that the classical light field $\vec{E}(t)$ is low-intensity. This is done in the spirit of a test beam that probes material gain without causing a significant change to carrier occupation in the system. Furthermore, Coulomb interaction and light-matter

interaction are treated separately.

In the following the contribution of the QDs to the macroscopic polarization will be discussed. It has the form

$$\vec{P}_{QD}(\omega) = \sum_{i,\sigma} \sum_{\sigma} \frac{\vec{d}_i^*}{AL} \hat{p}_{i,\sigma}(\omega) + \frac{\vec{d}_i}{AL} \hat{p}_{i,\sigma}^*(\omega). \quad (\text{E.19})$$

σ accounts for spin and i denotes the i^{th} QD in the ensemble, c.f. Ref. [20]. As in the gain model, QD without excited states are assumed; only QD polarization $p_{vc} = \langle a^\dagger v a_c \rangle$ and its adjoint need to be considered. As a result, only the dipole matrix elements $d_{vc}^i = d_i$ and $d_{cv}^i = d_i^*$ need to be considered. The indices v and c denote the valence and conduction band state of the QD.

The EOM for the microscopic polarization of the i^{th} QD reads

$$-i\hbar \frac{d}{dt} \langle a_v^\dagger a_c \rangle_i = \overbrace{(\varepsilon_{v_i} - \varepsilon_{c_i})}^{-\epsilon_i} \langle a_v^\dagger a_c \rangle_i - \vec{E}(t) \cdot \vec{d}_i \left[\langle a_c^\dagger a_c \rangle_i - \langle a_v^\dagger a_v \rangle_i \right] - \frac{1}{iT_2^i} \langle a_v^\dagger a_c \rangle_i, \quad (\text{E.20})$$

The test beam is intended to be low-intensity. Hence it is appropriate to assume the QD inversion $\langle a_v^\dagger a_v \rangle_i - \langle a_c^\dagger a_c \rangle_i = 1 - \rho_h^i - \rho_e^i$ in the light matter interaction term to be constant. This is often denoted as regime of *linear optics*. Introducing the polarization of the i^{th} QD as $\langle a_v^\dagger a_c \rangle_i = p_i$ Eq. (E.20) reads

$$-i\hbar \dot{p}_i(t) = -\epsilon_i p_i(t) + \vec{E}(t) \cdot \vec{d}_i (1 - \rho_h^i - \rho_e^i) - \frac{\hbar}{iT_2^i} p_i(t) \quad (\text{E.21})$$

This differential equation can be solved via Fourier transformation on both sides, and a partial integration on the left-hand side, resulting in

$$-i\hbar(-i\omega) \hat{p}_i(\omega) = -\epsilon_i \hat{p}_i(\omega) + \vec{E}(\omega) \cdot \vec{d}_i (1 - \rho_h^i - \rho_e^i) - \frac{\hbar}{iT_2^i} \hat{p}_i(\omega), \quad (\text{E.22})$$

$$\Leftrightarrow \hat{p}_i(\omega) = \frac{\vec{E}(\omega) \cdot \vec{d}_i (1 - \rho_h^i - \rho_e^i)}{\epsilon_i - \hbar\omega + \frac{\hbar}{iT_2^i}} \quad (\text{E.23})$$

The results for a single QD are close to Ref. [109]. The Fourier-transformed adjoint polarization $\hat{p}_{i,\sigma}^*(\omega)$ has the form

$$\hat{p}_{i,\sigma}^*(\omega) = \frac{\vec{E}(\omega) \cdot \vec{d}_i^* (1 - \rho_h^i - \rho_e^i)}{\epsilon_i + \hbar\omega - \frac{\hbar}{iT_2^i}}. \quad (\text{E.24})$$

Similar as in the appendix of [109] one can write the macroscopic polarization in the

E. Light matter interaction

form

$$\vec{P}_{QD}(\omega) = \sum_i \sum_{\sigma} \frac{\vec{d}_i^*}{AL} \hat{p}_{i,\sigma}(\omega) + \frac{\vec{d}_i}{AL} \hat{p}_{i,\sigma}^*(\omega) \quad (\text{E.25})$$

$$= \frac{2}{AL} \frac{\hat{E}(\omega) |d_i|^2 \vec{e}_{d_i} (\vec{e}_E \cdot \vec{e}_{d_i}) (1 - \rho_h^i - \rho_e^i)}{\epsilon_i - \hbar\omega + \frac{\hbar}{iT_2^i}} + \frac{2}{AL} \frac{\hat{E}(\omega) |d_i|^2 \vec{e}_{d_i} (\vec{e}_E \cdot \vec{e}_{d_i}) (1 - \rho_h^i - \rho_e^i)}{\epsilon_i + \hbar\omega - \frac{\hbar}{iT_2^i}} \quad (\text{E.26})$$

$$= \frac{2}{AL} \sum_i \left(\frac{\hat{E}(\omega) |d_i|^2 \vec{e}_{d_i} (\vec{e}_E \cdot \vec{e}_{d_i}) (1 - \rho_h^i - \rho_e^i) (\epsilon_i - \hbar\omega - \frac{\hbar}{iT_2^i})}{(\epsilon_i - \hbar\omega)^2 + (\frac{\hbar}{T_2^i})^2} + \frac{\hat{E}(\omega) |d_i|^2 \vec{e}_{d_i} (\vec{e}_E \cdot \vec{e}_{d_i}) (1 - \rho_h^i - \rho_e^i) (\epsilon_i + \hbar\omega + \frac{\hbar}{iT_2^i})}{(\epsilon_i + \hbar\omega)^2 + (\frac{\hbar}{T_2^i})^2} \right). \quad (\text{E.27})$$

Factor 2 originates from the spin sum.

E.2. Material gain

The QD contribution to material gain has the form

$$g(\omega) = -\frac{\omega}{n(\omega)c} \text{Im} \left(\frac{\vec{P}_{QD}(\omega) \cdot \vec{e}_E}{\epsilon_0 \vec{E}(\omega) \cdot \vec{e}_E} \right). \quad (\text{E.28})$$

The distinction between the QD and the background contribution is appropriate for the material gain in the model under consideration, because (i) the signatures of the subsystem in the gain spectra are clearly distinct in frequency domain and (ii) couplings between differing polarizations have not been considered. According to Eq. (E.27), the imaginary part of the polarization reads

$$\text{Im} \left(\vec{P}_{QD}(\omega) \right) = \frac{2}{AL} \sum_i \left(\frac{\hat{E}(\omega) |d_i|^2 \vec{e}_{d_i} (\vec{e}_E \cdot \vec{e}_{d_i}) (1 - \rho_h^i - \rho_e^i) (\frac{\hbar}{T_2^i})}{(\epsilon_i - \hbar\omega)^2 + (\frac{\hbar}{T_2^i})^2} + \frac{\hat{E}(\omega) |d_i|^2 \vec{e}_{d_i} (\vec{e}_E \cdot \vec{e}_{d_i}) (1 - \rho_h^i - \rho_e^i) (-\frac{\hbar}{T_2^i})}{(\epsilon_i + \hbar\omega)^2 + (\frac{\hbar}{T_2^i})^2} \right). \quad (\text{E.29})$$

The second term can be disregarded, since it is far away from resonance. Equation (E.29) is a sum of Lorentzian-shaped curves. The sum over all QDs can be transformed into an integral over all QD-resonance energies

$$\sum_i \rightarrow \int d\epsilon G(\epsilon),$$

where

$$G(\epsilon) = \frac{1}{\sqrt{2\pi}\sigma} e^{-\frac{1}{2}\left(\frac{\epsilon - \hbar\omega}{\sigma}\right)^2}, \quad (\text{E.30})$$

is a kind of density of states of the inhomogeneous broadened QD ensemble. The Gaussian shape reflects the statistical character of the resonance energy distribution, caused by QD size and composition fluctuations. A few additional approximations will be done for the evaluation: (i) Equal dipole matrix elements $d_i = d_{cv}$ occupation probabilities $\rho_\lambda^i = \rho_\lambda$ and dephasing times $T_2(\epsilon) = T_2$ are assumed for all QDs, (ii) the electric field of the test-beam is assumed to be parallel to the dipole-moment $\vec{e}_E = \vec{e}_{d_i}$. (iii) the occupation probabilities of the QD states are approximated by Fermi-distributions with the 2D chemical potential $\rho_\lambda = f_\lambda$ Under these assumptions, Eq. (E.29) becomes

$$\text{Im}(\vec{P}_{QD}(\omega)) \approx \vec{e}_d \int d\epsilon \frac{|d_{cv}|^2 2N_{QD}}{AL} \frac{\hat{E}(\omega) |d_{cv}|^2 (1 - f_h - f_e) \left(\frac{\hbar}{T_2}\right)}{(\epsilon - \hbar\omega)^2 + \left(\frac{\hbar}{T_2}\right)^2} G(\epsilon). \quad (\text{E.31})$$

N_{QD} denotes the number of QDs.

One achieves the gain formula by inserting the latter equation into Eq. (E.28):

$$g(\omega) = -\frac{\omega}{n_r c} \int d\epsilon \frac{|d_{cv}|^2 2N_{QD}}{AL} \frac{\hat{E}(\omega) |d_{cv}|^2 (1 - f_h - f_e) \left(\frac{\hbar}{T_2}\right)}{(\epsilon - \hbar\omega)^2 + \left(\frac{\hbar}{T_2}\right)^2} G(\epsilon). \quad (\text{E.32})$$

In principle, the refractive index n_r is a combination of the background refractive index and a carrier density and frequency-dependent contribution from the QDs. The latter can be determined from (E.27). However, $n_r = \sqrt{\epsilon_{\text{bg}}}$ will be used for the gain calculations, due to a minor correction to the QD contribution to the background reflective index, for the gain calculations will be used.

E.3. Refractive index

Via the Eqs. (E.4), (E.7) and (E.12), the refractive index n_r can be expressed as

$$n_r(\omega) = \sqrt{\frac{1}{2} \left[\epsilon(\omega) + \sqrt{\text{Re}(\epsilon^2(\omega)) + \text{Im}(\epsilon^2(\omega))} \right]}, \quad (\text{E.33})$$

$$= \sqrt{\frac{1}{2} \left[\text{Re}(\epsilon(\omega)) + |\epsilon(\omega)| \right]}, \quad (\text{E.34})$$

$$= \sqrt{\frac{1}{2} \left[(1 + \text{Re}(\chi(\omega))) + |(1 + \chi(\omega))| \right]}, \quad (\text{E.35})$$

In contrast to material gain, background polarization cannot be split off, since it is assumed to be constant in the considered domain under consideration. Actually, it is the main contributor to the refractive index.

The refractive index can be expressed via the macroscopic polarization as

E. Light matter interaction

$$n_r(\omega) = \sqrt{\frac{1}{2} \left[\left(1 + \operatorname{Re} \left[\frac{P_{QD}(\omega) + P_{bg}}{\varepsilon_0 E(\omega)} \right] \right) + \left| 1 + \frac{P_{QD}(\omega) + P_{bg}}{\varepsilon_0 E(\omega)} \right| \right]} \quad (\text{E.36})$$

with

$$\operatorname{Re} \left(\vec{P}_{QD}(\omega) \right) \approx \vec{e}_d \int d\epsilon \frac{|d_{cv}|^2 2N_{QD}}{AL} \frac{\hat{E}(\omega) |d_{cv}|^2 (1 - f_h - f_e) (\epsilon - \hbar\omega)}{(\epsilon - \hbar\omega)^2 + (\frac{\hbar}{T_2})^2} G(\epsilon). \quad (\text{E.37})$$

F. List of parameters

Table F.1.: Table of fundamental constants constants used in numerics.

Symbol	Value	Description
\hbar	0.658212 eV fs	\hbar , Planck-constant/ 2π
e_0	1	Elementary charge
k_B	8.617386×10^{-5} eV/K	Boltzmann constant
m_0	$5.685631 \text{ fs}^2 \text{ eV/nm}^2$	Electron mass
c	299.79 nm/fs	Speed of light
ϵ_0	$0.05526347 e_0/(\text{eV nm})$	Electric permittivity

Table F.2.: Standartly used material parameters for the calculations in Chap. 4.

Symbol	Value	Description
T	300 K	Temperature
ϵ_{bg}	12.5	Background permittivity index
m_e	$0.038 m_0$	Effective mass for electrons in the QD and the 2DCR
m_h	$0.492 m_0$	Effective mass for heavy holes in the QD and the 2DCR
m_{eB}	$0.067 m_0$	Effective mass for electrons in the 3DCR
m_{hB}	$0.5 m_0$	Effective mass for heavy holes in the 3DCR
ϵ_{GS}^e	0.13 eV	Energy distance GS - reservoir in the QD for electrons
ϵ_{ES}^e	0.065 eV	Energy distance GS - ES in the QD for electrons
ω_{QD}^e	$0.065 \text{ eV}/\hbar$	QD oscillator strength for conduction band states
ϵ_{GS}^h	0.035 eV	Energy distance GS - reservoir in the QD for holes
ϵ_{ES}^h	0.03 eV	Energy distance GS - ES in the QD for holes
ω_{QD}^h	$0.005 \text{ eV}/\hbar$	QD oscillator strength for valence band states
L	10 nm	Effective height of QDs and 2DCR
L_z	300 nm	Height of the 3DCR quantization volume
N_{2D}	6	Number of QD layers
N_{QD}/A	$1 \times 10^{10} \text{ cm}^{-2}$	QD area density (per layer)

F. List of parameters

Table F.3.: Parameters changed for calculations in Sec. 4.3.8.

Symbol	Value	Description
m_e	$0.038 m_0$	Effective mass for electrons in the QD and the 2DCR
m_h	$0.492 m_0$	Effective mass for heavy holes in the QD and the 2DCR
m_{eB}	m_e	Effective mass for electrons in the 3DCR
m_{hB}	m_h	Effective mass for heavy holes in the 3DCR
ε_{GS}^e	0.08 eV	Energy distance GS - reservoir in the QD for electrons
ε_{ES}^e	0.04 eV	Energy distance GS - ES in the QD for electrons
ω_{QD}^e	$0.04 \text{ eV}/\hbar$	QD oscillator strength for conduction band states
ε_{GS}^h	0.03 eV	Energy distance GS - reservoir in the QD for holes
ε_{ES}^h	0.015 eV	Energy distance GS - ES in the QD for holes
ω_{QD}^h	$0.015 \text{ eV}/\hbar$	QD oscillator strength for valence band states
L_z	500 nm	Height of the 3DCR quantization volume
N_{2D}	5	Number of QD layers

Table F.4.: Parameters for the numerics of the gain model in Chap. 5.

Symbol	Value	Description
T	300 K	Temperature
ϵ_{bg}	12.5	Background permittivity index
m_e	$0.061 m_0$	Effective mass for electrons in the QD and the 2DCR
m_h	$0.101 m_0$	Effective mass for heavy holes in the QD and the 2DCR
d	$0.6 e_0 \text{ nm}$	Dipole moment
ε_{GS}^e	0.037 eV	Energy distance GS - reservoir in the QD for electrons
ω_{QD}^e	$0.037 \text{ eV}/\hbar$	QD oscillator strength for conduction band states
ε_{ES}^h	0.031 eV	Energy distance GS - ES in the QD for holes
ω_{QD}^h	$0.031 \text{ eV}/\hbar$	QD oscillator strength for valence band states
L	5 nm	Effective height of QDs and 2DCR
N_{QD}/A	$5 \times 10^{10} \text{ cm}^{-2}$	QD area density
N_{2D}	1	Number of QD layers
σ_{FWHM}	50 meV	FWHM of the Gaussian-shaped inhom. broadening

Danksagung

Mein besonderer Dank geht an Priv.-Doz. Dr. Uwe Bandelow und Prof. Andreas Knorr für die Betreuung der Arbeit.

Ich danke Frau Prof. Woggon für die Übernahme des Prüfungsvorsitzes.

Mein Dank geht auch an Michael Lorke, Kolja Schuh, Matthias Florian, Prof. Hans Christian Schneider und Prof. Frank Jahnke für hilfreiche Gespräche über Coulomb-Streuung.

Thomas Koprucki, Jeong Eun Kim, Niels Majer, Kathy Lüdge und Ermin Malic sei für die Zusammenarbeit im Rahmen des Sfb 787 gedankt.

Ich bedanke mich vielfach und noch öfter bei Peter Mathé für die Zusammenarbeit und Anleitung im Bereich Quasi-Monte Carlo Integration und bei Andrei Schliwa und Deniz Breddermann für die Zusammenarbeit zur Untersuchung der Reservoirdimensionalität.

Ein herzliches Dankeschön an Franz Schulze, Carsten Brée, Sandra Kuhn, Frank Milde und Shalva Amiranashvili für das Korrekturlesen des Manuskripts.

Frau Rebecca M. Stuart sei für die sprachliche Überarbeitung des Manuskripts vielfach gedankt.

Ein besonderer Dank geht auch an Ihar Babushkin, Thomas Koprucki, Rico Buchholz und Shalva "Lord of Mathematica" Amiranashvili für viele Tipps und Hilfen beim Programmieren.

Paul Racec und Hans-Jürgen Wünsche sei für die interessanten und lehrreichen Diskussionen über Wellenfunktionen und Halbleiterlaser herzlich gedankt.

Den Mitgliedern der School of Nanophotonics sei für viele lehrreiche Diskussionen über Quantenpunkte gedankt.

Ich möchte auch der gesamten AG Knorr (TU) und FG2 (WIAS) für die nette Atmosphäre und viele anregende Unterhaltungen über Physik und vieles mehr meinen Dank aussprechen. In diesem Sinne bedanke ich mich auch besonders bei meinen Büronachbarn Carsten Brée, Sven-Joachim Kimmerle, Antonio Perez-Serrano und Taras Girnyk (WIAS), Rico Buchholz, Alexander Kothe und Fabian Paul (TU), sowie Shalva Amiranashvili.

Insbesondere möchte ich bei meiner Familie für die immerwährende Unterstützung bedanken.

Die Sobol-Punkte zur numerischen Integration wurden mit einem Programm von F. Kuo und S. Joe erstellt.

Diese Arbeit wurde durch den Sonderforschungsbereich 787 gefördert.

G. Bibliography

- [1] J. M. M. Bertoni. *Struktur von GaAs-Oberflächen und ihre Bedeutung für InAs-Quantenpunkte*. Ph.D. thesis, Technische Universität Berlin (2000).
- [2] E. Malic. *Many-particle theory of optical properties in low-dimensional nanostructures*. Ph.D. thesis, TU Berlin, Berlin (2008).
- [3] J. Siegert, S. Marcinkevicius, and Q. X. Zhao. *Carrier dynamics in modulation-doped InAs/GaAs quantum dots*. *Phys. Rev. B*, **72** (2005).
- [4] S. Sanguinetti, M. Gurioli, K. Watanabe, T. Tateno, and N. Koguchi. *Dependence of quantum dot Auger carrier relaxation on barrier dimensionality: an experimental study*. *Semicond. Sci. Technol.*, **19**, 293 (2004). doi:10.1088/0268-1242/19/4/098.
- [5] From: <http://www.internetworldstats.com/stats.htm>; visited on 21.2.2012.
- [6] *Cisco Visual Networking Index: Forecast and Methodology, 2009 - 2014* (2010).
- [7] D. Bimberg, M. Grundmann, and N. N. Ledentsov. *Quantum Dot Heterostructures*. Wiley, New York (1998).
- [8] P. Borri, W. Schneider, S. anf Langbein, and D. Bimberg. *Ultrafast carrier dynamics in InGaAs quantum dot materials and devices*. *Journal of Optics A: Pure and Applied Optics*, **8**, 33 (2006).
- [9] H. Haug and H. Haken. *Theory of Noise in Semiconductor Laser Emission*. *Zeitschrift für Physik*, **204**, 262 (1967).
- [10] H. Haug and S. Schmitt-Rink. *Electron theory of the optical properties of laser-excited semiconductors*. *Progress in Quantum Electronics*, **9**, 3 (1984). ISSN 0079-6727. doi:10.1016/0079-6727(84)90026-0.
- [11] G. Bastard. *Superlattice band structure in the envelope-function approximation*. *Phys. Rev. B*, **24**, 5693 (1981). doi:10.1103/PhysRevB.24.5693.
- [12] S. Schmitt-Rink, C. Ell, and H. Haug. *Many-body effects in the absorption, gain, and luminescence spectra of semiconductor quantum-well structures*. *Phys. Rev. B*, **33**, 1183 (1986). doi:10.1103/PhysRevB.33.1183.
- [13] M. Lindberg and S. W. Koch. *Effective Bloch equations for semiconductors*. *Phys. Rev. B*, **38**, 3342 (1988). doi:10.1103/PhysRevB.38.3342.
- [14] H. Haug and S. W. Koch. *Semiconductor laser theory with many-body effects*. *Phys. Rev. A*, **39**, 1887 (1989). doi:10.1103/PhysRevA.39.1887.

G. Bibliography

- [15] R. Binder, D. Scott, A. E. Paul, M. Lindberg, K. Henneberger, and S. W. Koch. *Carrier-carrier scattering and optical dephasing in highly excited semiconductors*. Phys. Rev. B, **45**, 1107 (1992). doi:10.1103/PhysRevB.45.1107.
- [16] J. Hader, J. Moloney, S. Koch, and W. W. Chow. *Microscopic Modeling of Gain and Luminescence in Semiconductors*. IEEE Journal of Selected Topics in Quantum Electronics, **9**, 688 (2003).
- [17] U. Bockelmann and T. Egeler. *Electron relaxation in quantum dots by means of Auger processes*. Phys Rev B, **46** (1992).
- [18] A. V. Uskov, F. Adler, H. Schweizer, and M. H. Pilkuhn. *Auger carrier relaxation in self-assembled quantum dots by collisions with two-dimensional carriers*. J.Appl. Phys., **12**, 7895 (1997).
- [19] H. C. Schneider, W. W. Chow, and S. W. Koch. *Many-body effects in the gain spectra of highly excited quantum-dot lasers*. Phys. Rev. B, **64**, 115315 (2001). doi:10.1103/PhysRevB.64.115315.
- [20] T. Nielsen, P. Gartner, and F. Jahnke. *Many-body theory of carrier capture and relaxation in semiconductor quantum-dot lasers*. Phys Rev B, **69**, 1 (2004).
- [21] H. H. Nilsson, J.-Z. Zhang, and I. Galbraith. *Homogeneous broadening in quantum dots due to Auger scattering with wetting layer carriers*. Phys Rev B, **72**, 205331 (2005).
- [22] R. Ferreira and G. Bastard. *Unbound states in quantum heterostructures*. Nanscale Research Letters, **1**, 120 (2006).
- [23] D. Bimberg, private communication.
- [24] M. Lorke, T. Nielsen, J. Seebeck, P. Gartner, and F. Jahnke. *Influence of carrier-carrier and carrier-phonon correlations on optical absorption and gain in quantum-dot systems*. Phys Rev B, **73**, 1 (2006).
- [25] H. C. Schneider, W. W. Chow, and S. W. Koch. *Excitation-induced dephasing in semiconductor quantum dots*. Phys. Rev. B, **70**, 235308 (2004). doi:10.1103/PhysRevB.70.235308.
- [26] J. L. Pan. *Ionization balance in semiconductor quantum-dot lasers*. Phys. Rev. B, **49**, 2536 (1994). doi:10.1103/PhysRevB.49.2536.
- [27] J. L. Pan and P. L. Hagelstein. *Collisional processes involved in the population kinetics of semiconductor quantum-dot lasers*. Phys. Rev. B, **49**, 2554 (1994). doi:10.1103/PhysRevB.49.2554.
- [28] R. Wetzler, A. Wacker, and E. Schöll. *Coulomb scattering with remote continuum states in quantum dot devices*. Journal of Applied Physics, **95**, 7966 (2004). doi:10.1063/1.1739284.

- [29] A. L. Vartanian. *Electron capture and intra-band relaxation by means of Auger processes in colloidal semiconductor nanocrystals*. Physica B, **406**, 331 (2011).
- [30] S. Sanguinetti, K. Watanabe, T. Tantenno, M. Wakaki, and N. Koguchi. *Role of the wetting layer in the carrier relaxation in quantum dots*. Applied Physics Letters, **81**, 613 (2002).
- [31] H. Niederreiter. *Random Number Generation and Quasi-Monte Carlo Methods*. SIAM, Philadelphia (1992).
- [32] S. Joe and F. Kuo. *Remark on Algorithm 659: Implementing Sobol's quasirandom sequence generator*. ACM Trans. Math. Softw., **29**, 49 (2003).
- [33] M. Grundmann. *Nano-Optoelectronics Concepts, Physics and Devices*. Springer, Berlin (2002).
- [34] E. Malic, K. J. Ahn, M. J. P. Bormann, P. Hovel, E. Scholl, A. Knorr, M. Kuntz, and D. Bimberg. *Theory of relaxation oscillations in semiconductor quantum dot lasers*. Appl. Phys. Lett., **89**, 101107 (2006).
- [35] T. Koprucki, private communication.
- [36] G. Blatter. *Quantenmechanik I* (2005). Lecture notes from the ETH Zürich; http://www.itp.phys.ethz.ch/education/prev_lectures/ss06/qm2/QM.pdf.
- [37] W. Nolting. *Grundkurs Theoretische Physik 5/2 Quantenmechanik und Anwendungen*. Springer, Berlin (2006).
- [38] H. Haken. *Quantenfeldtheorie des Festkörpers*. Teubner Verlag, Stuttgart (1993).
- [39] H. Haug and S. W. Koch. *Quantum Theory of the Optical and Electronic Properties of Semiconductors*. World Scientific, Singapore (2009).
- [40] I. A. Ostapenko, G. Hönig, S. Rodt, A. Schliwa, A. Hoffmann, D. Bimberg, M.-R. Dachner, M. Richter, A. Knorr, S. Kako, and Y. Arakawa. *Exciton acoustic-phonon coupling in single GaN/AlN quantum dots*. Phys. Rev. B, **85**, 081303 (2012). doi:10.1103/PhysRevB.85.081303.
- [41] M.-R. Dachner, E. Malic, M. Richter, A. Carmele, J. Kabuss, A. Wilms, J.-E. Kim, G. Hartmann, J. Wolters, U. Bandelow, and A. Knorr. *Theory of carrier and photon dynamics in quantum dot light emitters*. Phys. Status Solidi B, **247**, 809 (2010).
- [42] W. W. Chow, L. M., and J. F. *Will Quantum Dots Replace Quantum Wells As the Active Medium of Choice in Future Semiconductor Lasers?* IEEE Journal of Selected Topics in Quantum Electronics, **17**, 1349 (2011).
- [43] K. Schuh, private communication.
- [44] F. Rossi and T. Kuhn. *Theory of ultrafast phenomena in photoexcited semiconductors*. Reviews of modern physics, **74**, 895 (2002).

G. Bibliography

- [45] G. Park, O. B. Shchekin, D. L. Huffaker, and D. G. Deppe. *Lasing from In-GaAs/GaAs quantum dots with extended wavelength and well-defined harmonic-oscillator energy levels*. Applied Physics Letters, **73**, 3351 (1998). doi:10.1063/1.122766.
- [46] T. R. Nielsen. *Carrier-Carrier and Carrier-Phonon Scattering in Self-Assembled Quantum Dots*. Ph.D. thesis, University of Bremen (2005).
- [47] S. L. Chuang. *Physics of Optoelectronic Devices*. Wiley & Sons, New York (1995).
- [48] R. Wüst. *Mathematik für Physiker und Mathematiker Band 1: Reelle Analysis und Lineare Algebra*. Wiley-VCH, Weinheim (2002).
- [49] A. Wilms, D. Breddermann, and P. Mathé. *Theory of direct capture from two- and three-dimensional reservoirs to quantum dot states*. Phys. Status Solidi C, **9**, 1278 (2012).
- [50] A. Knorr. *Spatial Effects in the Ultrafast Optics and Kinetics of Semiconductors* (1997). Habilitationsschrift. Philipps-Universität Marburg.
- [51] D. Breddermann. *Theorie der Ladungsträgerstreuung in einer Halbleiter-Laserstruktur*. Master's thesis, TU Berlin, Berlin (2009).
- [52] J. Wolters. *On the Self Consistent Theory of Nonequilibrium Phonos in Semiconductor Devices*. Master's thesis, TU Berlin, Berlin (2009).
- [53] J. Joyce and R. Dixon. Appl. Phys. Lett., **31**, 354 (1977).
- [54] V. Aguilera-Navaro, G. Esterez, and A. Kosteki. J. Appl. Phys., **63**, 2848 (1988).
- [55] F. Schulze, M. Schoth, U. Woggon, A. Knorr, and C. Weber. *Ultrafast dynamics of carrier multiplication in quantum dots*. Phys. Rev. B, **84**, 125318 (2011). doi: 10.1103/PhysRevB.84.125318.
- [56] H.-P. Breuer and P. F. *The theory of open quantum systems*. Oxford University Press, Oxford (2002).
- [57] S. Mukamel. *Principle of Nonlinear Optical Spectroscopy*. Oxford University Press, Oxford (1995).
- [58] J. Fricke. *Transport Equations Including Many-Particle Correlations for an Arbitrary Quantum System: A General Formalism*. ANNALS OF PHYSICS, **252**, 479 (1996).
- [59] J. Fricke, V. Meden, C. Wöhler, and K. Schönhammer. *Improved Transport Equations Including Correlations for Electron-Phonon Systems: Comparison with Exact Solutions in One Dimension*. ANNALS OF PHYSICS, **253**, 177 (1997).
- [60] E. Fick and G. Sauermaun. *Quantenstatistik Dynamischer Prozesse, Band I. Generelle Aspekte*. Verlag Harri Deutsch, Thun (1983).

- [61] P. Borri, S. Schneider, U. Woggon, R. L. Sellin, D. Ouyang, and D. Bimberg. *Exciton Relaxation and Dephasing in Quantum-Dot Amplifiers From Room to Cryogenic Temperature*. IEEE Journal of Selected Topics in Quantum Electronics, **8**, 984 (2002).
- [62] N. Majer, K. Lüdge, and E. Schöll. *Cascading enables ultrafast gain recovery dynamics of quantum dot semiconductor optical amplifiers*. Phys. Rev. B, **82** (2010).
- [63] E. Malic, M. J. Bormann, P. Hövel, M. Kuntz, D. Bimberg, A. Knorr, and E. Schöll. *Coulomb Damped Relaxation Oscillations in Semiconductor Quantum Dot Lasers*. IEEE, J. Sel. Topics Quantum Electron., **13**, 1242 (2007).
- [64] K. Lüdge and E. Schöll. *Quantum-Dot Lasers - Desynchronized Nonlinear Dynamics of Electrons and Holes*. IEEE Journal of Quantum Electronics, **45**, 1396 (2009).
- [65] J. E. Kim. *Microscopic Description of Quantum-Dot Vertical-Cavity Surface-Emitting Structures Using Maxwell-Bloch Equations*. Ph.D. thesis, TU Berlin, Berlin (2011).
- [66] E. Malic. *Dynamic Theory of Semiconductor Quantum Dot Lasers*. Master's thesis, TU Berlin, Berlin (2005).
- [67] F. Jahnke, M. Kira, and S. Koch. *Linear and nonlinear optical properties of excitons in semiconductor quantum wells and microcavities*. Zeitschrift für Physik B Condensed Matter, **104**, 559 (1997). ISSN 0722-3277. 10.1007/s002570050490.
- [68] W. W. Chow, S. W. Koch, and M. Sargent III. *Semiconductor Laser Physics*. Springer, Berlin (1999).
- [69] M. Lorke. *Optical gain and laser properties of semiconductor quantum-dot systems*. Ph.D. thesis, University of Bremen (2008).
- [70] M. Lorke, W. W. Chow, T. R. Nielsen, J. Seebeck, P. Gartner, and F. Jahnke. *Anomaly in the excitation dependence of the optical gain of semiconductor quantum dots*. Phys. Rev. B, **74** (2006).
- [71] E. Gehrig and O. Hess. *Spatio-Temporal Dynamics and Quantum Fluctuations in Semiconductor lasers*. Springer, Berlin (2003).
- [72] T. Kuhn. *Ladungsträgerdynamik in Halbleitersystemen fern vom Gleichgewicht: Elektronisches Rauschen und kohärente Prozesse* (1994). Habilitationsschrift. Universität Stuttgart.
- [73] O. Hess and T. Kuhn. *Maxwell-Bloch equation for spatially inhomogeneous semiconductor lasers. I. Theoretical formulation*. Phys Rev A, **54**, 3347 (1996).
- [74] F. Steininger, A. Knorr, T. Stroucken, P. Thomas, and S. W. Koch. *Dynamic Evolution of Spatiotemporally Localized Electronic Wave Packets in Semiconductor*

G. Bibliography

- Quantum Wells*. Phys. Rev. Lett., **77**, 550 (1996). doi:10.1103/PhysRevLett.77.550.
- [75] E. Gehrig and O. Hess. *Mesoscopic spatiotemporal theory for quantum-dot lasers*. Phys Rev A, **65**, 1 (2002).
- [76] D. Reschner, E. Gehrig, and O. Hess. *Mesoscopic spatiotemporal theory for quantum-dot lasers*. IEEE, Journal of quantum electronics, **45**, 21 (2009).
- [77] F. Steininger, A. Knorr, P. Thomas, and S. W. Koch. *The influence of electron-phonon scattering on the spatio-temporal dynamics of electron wavepackets in semiconductor quantum wells*. Zeitschrift für Physik B, **103**, 45 (1997).
- [78] I. Büll. *Physik mit dem PC*. Teubner (1998).
- [79] H. Schaback and H. Wendland. *Numerische Mathematik*. Springer, Berlin (2005).
- [80] P. Mathé, private communication.
- [81] M. Matsumoto and T. Nishimura. A C-program for MT19937, with initialization improved 2002/1/26.
- [82] S. Joe and F. Kuo. *Constructing Sobol Sequences with Better Two-Dimensional Projections*. SIAM Journal on Scientific Computing, **30**, 2635 (2008). doi:10.1137/070709359.
- [83] Weisstein, Eric W. "Lambert W-Function." From MathWorld—A Wolfram Web Resource. <http://mathworld.wolfram.com/LambertW-Function.html> . Visited 29.08.2012.
- [84] W. W. Chow and S. W. Koch. IEEE, Journal of selected topics in quantum electronics, **41**, 495 (2005).
- [85] K. Lüdge and E. Schöll. *Nonlinear dynamics of doped semiconductor quantum dot lasers*. The European Physical Journal D, **58**, 167 (2010).
- [86] J. Kim, M.-R. Dachner, A. Wilms, and E. Malic. *Microscopic study of relaxation oscillations in quantum-dot VCSELs*. Photonics and Nanostructures—Fundamentals and Applications, **9**, 337 (2011).
- [87] U. Bandelow, R. Hünlich, and T. Koprucki. *Simulation of Static and Dynamic Properties of Edge-Emitting Multi Quantum Well Lasers*. IEEE J. Select. Topics Quantum Electron., **9**, 798 (2003).
- [88] W. A. Hügel, M. F. Heinrich, and M. Wegener. *Dephasing Due to Carrier-Carrier Scattering in 2D*. phys. stat. sol. (b), **221**, 473 (200).
- [89] G. E. Cragg and A. L. Efros. *Suppression of Auger Processes in Confined Structures*. Nano Letters, **10**, 313 (2010).

- [90] V. B. Verma, M. J. Stevens, K. L. S. nad N. L. Dias, A. Garg, J. J. Coleman, and W. P. Mirin. *Time-resolved photoluminescence of lithographically defined quantum dots fabricated by electron beam lithography and wet chemical etching*. Journal of Applied Physics, **109** (2011).
- [91] F. Adler, M. Geiger, A. Bauknecht, F. Scholz, H. Schweizer, B. Ohnesorg, A. Forchel, and M. H. Pilkuhn. *Optical transitions and carrier relaxation in self assembled InAs/GaAs quantum dots*. Journal of Applied Physics, **80**, 4019 (1996).
- [92] D. Morris, N. Perret, and S. Fafard. *Carrier energy relaxation by means of Auger processes in InAs/GaAs self-assembled quantum dots*. Applied Physics Letters, **75**, 3593 (1999). doi:10.1063/1.125398.
- [93] J. E. Kim, E. Malić, M. Richter, A. Wilms, and A. Knorr. *Maxwell-Bloch Equation Approach for Describing the Microscopic Dynamics of Quantum-Dot VCSELs*. IEEE Journal of Quantum Electronics, **46**, 1115 (2010).
- [94] H.-Y. Liu, Z.-M. Meng, Q.-F. Dai, L.-J. Wu, Q. Guo, W. Hu, S.-H. Liu, S. Lan, and T. Yang. *Ultrafast carrier dynamics in undoped and p-doped InAs/GaAs quantum dots characterized by pump-probe reflection measurements*. Journal of Applied Physics, **103**, 083121 (2008). doi:10.1063/1.2913316.
- [95] K. W. Sun, J. W. Chen, B. C. Lee, C. P. Lee, and A. M. Kechiantz. *Carrier capture and relaxation in InAs quantum dots*. Nanotechnology, **16**, 1530 (2005).
- [96] E. R. Racec, P. Racec, and U. Wulf. *Resonant transport through semiconductor nanostructures*. Recent Research Developments in Physics, **4**, 387 (2003).
- [97] M. Baro, H.-C. Kaiser, H. Neidhardt, and R. J. *A quantum transmitting Schrödinger-Poisson system*. Reviews in Mathematical Physics, **16**, 281 (2004).
- [98] K. Lüdge, M. J. P. Bormann, E. Malić, P. Hövel, M. Kuntz, D. Bimberg, A. Knorr, and E. Schöll. *Turn-on dynamics and modulation response in semiconductor quantum dot lasers*. Phys. Rev. B, **78**, 035316 (2008). doi:10.1103/PhysRevB.78.035316.
- [99] T. Koprucki, A. Wilms, A. Knorr, and U. Bandelow. *Modeling of quantum dot lasers with microscopic treatment of Coulomb effects* (2011).
- [100] Y. P. Varshni. *Temperature dependence of the energy gap in semiconductors*. Physica, **34**, 149 (1967).
- [101] W. Demtröder. *Atoms, Molecules and Photons*. Springer, Berlin (2010).
- [102] H. Shahid, D. T. D. Childs, B. J. Stevens, and R. A. Hogg. *Negative differential gain due to many body effects in self-assembled quantum dot lasers*. Applied Physics Letters, **99**, 061104 (2011). doi:10.1063/1.3624708.
- [103] P. G. Eliseev, H. Li, A. Stintz, G. T. Liu, T. C. Newell, K. J. Malloy, and L. F. Lester. *Transition dipole moment of InAs/InGaAs quantum dots from experiments*

G. Bibliography

- on ultralow-threshold laser diodes*. Applied Physics Letters, **77**, 262 (2000). doi: 10.1063/1.126944.
- [104] R. Sellin, C. Heinrichsdorff, C. Ribbat, M. Grundmann, U. W. Pohl, and D. Bimberg. *Surface flattening during MOVCD of thin GaAs layers covering InGaAs quantum dots*. Journal of Crystal Growth, **221**, 581 (2000).
- [105] J. Wolters, M.-R. Dachner, E. Malic, M. Richter, U. Woggon, and A. Knorr. *Carrier heating in light-emitting quantum-dot heterostructures at low injection currents*. Phys Rev B, **80** (2009).
- [106] G. D. Mahan. *Many-Particle Physics*. Plenum Press, New York (1990).
- [107] R. Wüst. *Mathematik für Physiker und Mathematiker Band 2: Reelle Analysis und Lineare Algebra*. Wiley-VCH, Weinheim (2002).
- [108] H. Wenzel and H.-J. Wünsche. *An Equation for the Amplitudes of the Modes in Semiconductor Lasers*. IEEE Journal of Quantum Electronics, **30**, 2073 (1994).
- [109] S. Ritter. *Mikroskopische Theorie der Dynamik zweier gekoppelter Halbleiter-Quantenpunkte*. Master's thesis, TU Berlin, Berlin (2006).